University of South Carolina
Scholar Commons

Theses and Dissertations

2018

Multifunction Radio Frequency Composite Structures

David L. Zeppettella
University of South Carolina

Follow this and additional works at: https://scholarcommons.sc.edu/etd

 Part of the Electrical and Computer Engineering Commons

Recommended Citation
Zeppettella, D. L.(2018). *Multifunction Radio Frequency Composite Structures.* (Doctoral dissertation). Retrieved from https://scholarcommons.sc.edu/etd/4603

This Open Access Dissertation is brought to you by Scholar Commons. It has been accepted for inclusion in Theses and Dissertations by an authorized administrator of Scholar Commons. For more information, please contact dillarda@mailbox.sc.edu.

Multifunction Radio Frequency Composite Structures

by

David L. Zeppettella

Bachelor of Engineering
Youngstown State University 1995

Master of Science
University of Dayton 2011

Submitted in Partial Fulfillment of the Requirements

for the Degree of Doctor of Philosophy in

Electrical Engineering

College of Engineering and Computing

University of South Carolina

2018

Accepted by:

Mohammod Ali, Major Professor

Grigory Simin, Committee Member

Guoan Wang, Committee Member

Juan Caicedo, Committee Member

Cheryl L. Addy, Vice Provost and Dean of the Graduate School

Dedication

To my wife and daughter,

and in loving memory of my parents, Carmen and Marilyn.

Acknowledgments

The work presented here is the result of not just my own efforts, but also those who supported me in this endeavor. First I wish to express my appreciation to my advisor, Dr. Mohammod Ali, for all of his guidance, expertise, and patience during this research. I would also like to thank the members of my committee, Dr. Grigory Simin, Dr. Guoan Wang, and Dr. Juan Caicedo for reviewing the work and contributing suggestions for improvement. Additionally, the assistance of Todd Bussey, Philip Knoth, Russ Topp, Jason Jewel, and Jason Miller in the fabrication of prototype antennas and composite structures was critical in completing this work, and their efforts are much appreciated.

Thanks to my wife and daughter for their understanding as I worked toward this goal. Hopefully the trips to Columbia partially compensated for the family outings and activities that I missed because of the demands of academia.

I would be remiss if I failed to recognize all of the teachers, professors, and mentors who contributed to my development over the years. The list of those who encouraged and inspired me is long indeed. Hi, Mr. Clark.

All contents cleared for public release: Case Number 88ABW-2018-0542

Abstract

There has been recent interest in the development of multifunction structures for weight-critical applications. A multifunction structure is a load-bearing structure that also allows one or more additional functions such as RF communication, energy storage, sensing etc. The focus of this dissertation is to analyze, design, develop, and test new high performance (broadband, high gain, circularly polarized) internal antennas that are structural and integral to the aircraft. It is demonstrated that antennas with more bandwidth and higher efficiency could be developed if the space and materials available in an aircraft structure could be judiciously exploited for multifunctional usage. This is improbable with bolt-on approaches, such blade antennas or antennas housed within a wing pod.

Firstly, a method called Characteristic Mode Analysis (CMA) is studied and used both for a dipole antenna and a VHF airfoil integrated antenna. Although computationally intensive, it provides fundamental insights on the significance of each mode, modal interactions, and overall achievable bandwidth. The CMA of a dipole antenna loaded with a thin coating of DNG material is undertaken. The presented analysis considers the MoM Galerkin formulation. The analyses presented demonstrate that when the relative permittivity and permeability are greater than -1 but less than 0, the configuration shows potential for antenna size reduction. For example, a 25% size reduction is achieved when the relative permittivity and permeability are equal to -0.3.

Secondly, the study, design, and development of a broadband (2:1 frequency ratio), positive gain ($>$ 0 dBi), VHF antenna integrated within a composite airfoil structure

are undertaken to overcome the limitations of very low gain (-20 dBi typical at low VHF frequencies) associated with resistively matched, electrically small, broadband airborne blade antennas. It is demonstrated that a broadband antenna operating from 89-220 MHz can be incorporated into composite structures. Simulation and experimental results clearly show that such antennas can be built using structural composite materials, such as fiberglass or cyanate-ester/quartz, Rohacell foam and conductive mesh with appropriate thicknesses commensurate with the frequency band of operation. Additionally, the antenna is studied with CMA to understand the contributions of various modes to antenna performance and to asses the performance impact of composite materials as a result of structural integration. The proposed sandwich structure antenna was also studied for possible MIMO application in an inverted V-tail UAV configuration. The two antennas in that configuration clearly show excellent performance based on their ECC and simulated radiation patterns.

Finally, fundamental studies and innovations are made in the topic area of structurally integrated, broadband, circularly polarized spiral antennas on EBG structures. To allow directional radiation, spirals require a quarter of a wavelength separation when placed on a reflecting surface (e.g. the aircraft's ground). This thickness (as much as 6 inches or more at 450 MHz) is a significant challenge from a structural integration perspective and is unacceptable at UHF frequencies. While RF absorbing materials have been proposed, they significantly reduce antenna efficiency. To our knowledge, no work on spirals on EBGs has been reported that addresses either the broadband EBG design challenges in the UHF frequency band or the integration of such structures with composite aircraft platforms. Therefore, the investigation, design, and development of an equiangular spiral antenna on an EBG are conducted for 425-800 MHz satellite communication applications. Starting from a mushroom EBG structure, analysis and simulations are undertaken to determine the dependency of antenna gain bandwidth, impedance bandwidth, pattern bandwidth, and axial ratio

on the EBG geometry, materials, and height. A structural integration scheme is proposed, and a corresponding antenna plus EBG with nearly an octave bandwidth is designed, built, and tested that demonstrate good circularly polarized performance (gain greater than 4 dBi RHCP and axial ratio less than 3 dB). While further optimization of gain versus axial ratio versus EBG geometry and height is quite possible, the findings demonstrate the clear feasibility of a RHCP spiral antenna on a planar, tapered EBG with half the thickness of a traditional spiral on a reflector for composite structural integration.

Table of Contents

List of Tables

List of Figures

Chapter 1

Introduction

1.1 Background

Although the use of remotely piloted aircraft and auto piloted vehicles, so called unmanned aerial vehicles (UAV) or drones, started out primarily in military applications, the growth of the commercial drone industry is expected to out pace the military by 14% between 2015 and 2020 [1]. For example, Google and Facebook have purchased aerospace companies with the goal of providing internet access to remote areas via high altitude, long endurance aircraft. Amazon is developing technology to deliver packages to customers using drones, and drone manufacturers are now specifically marketing vehicles for commercial operations[2, 3, 4]. Wireless communications is at the core of all of these applications. The work described in this dissertation deals with enabling not only more efficient antennas for UAVs such as those shown in Figure 1.1, but also more weight efficient ways of incorporating antennas onto the aircraft.

Figure 1.1: a) The Solara 50 solar powered drone from Google / Titan Aerospace [5]. b) Insitu Integrator [6].

Conventionally, the design of aircraft structures and functional subsystems are considered to be separate areas of endeavor, with the primary aim of this philosophy being to reduce complexity in the design process [7]. In the case of aircraft antennas, the standard manufacturing techniques used for attaching antennas to the vehicle can introduce additional weight, aerodynamic drag, or both. While these issues are detrimental to performance in any air vehicle, weight and drag are critical considerations in high-altitude, long endurance (HALE) vehicles such as the Solara 50 and weight is an important factor for small drones.

One approach that has been suggested to overcome the problems associated with traditional antenna integration methods is to develop multifunctional air vehicle structures that are capable of performing an antenna function in addition to their conventional role of carrying flight loads [8, 9]. Known in the literature as Conformal Load-bearing Antennas Structures (CLAS), this concept is an unconventional approach to aircraft design in which the vehicle's structure is designed and fabricated with conductive geometry as an inherent part of the structure to enable a desired antenna function. The ultimate goal of this approach is to enable enhanced RF performance while having minimal weight and drag impact on the flight vehicle.

The conventional approach for antenna integration with an air vehicle is to design the antenna as a stand-alone device, and subsequently package the antenna in a protective housing that is then attached to the vehicle. Although simulations can be used to investigate and compensate for some of the effects of the vehicle on antenna performance, the antenna often requires tuning after mounting. Figure 1.2 shows a UHF aircraft antenna packaged in an aerodynamic housing for attachment to the exterior of the vehicle. Antennas with this form factor are referred to as blade antennas and are commonly used on commercial aircraft.

One problem with blade antennas is that they are electrically small in the VHF and lower UHF bands, and it is well known that an electrically small antenna is inefficient

(a) (b)

Figure 1.2: (a) UHF Blade antenna for aircraft applications [10]. (b) Direct Write VHF antenna on aircraft fairing [11].

[12, 13]. An alternative approach is to leverage the physical space available on an aircraft's structure to enable a larger antenna. Figure 1.2b illustrates an example of this concept in which a VHF antenna was fabricated on a Boeing 737 fairing using Direct Write technology [11]. This offers the advantage of large antenna with an insignificant weight increase and no drag penalty for the aircraft.

1.2 Objectives

The ultimate goal of this work is to study and design multifunction structures that can be functional blocks of an aircraft such as a vertical stabilizer or fuselage as well as support RF antenna functions for communications and radar. As mentioned, the general topic area falls within the CLAS concept. Chapter 2 provides a more in-depth review of previous work within the CLAS topic area. A brief literature review of CLAS reveals the following notable areas of contributions:

1. Slotted waveguide arrays made within composite structures operating at X-band [14, 15]

2. 200 MHz to 2 GHz Spiral antenna within a deep cavity within an aircraft [9].

3. Structurally Integrated X-band Array [16].

4. Ku-band Microstrip patch antennas and their general adaptation within a composite sandwich panel [17].

5. UHF Log Periodic Dipole Array (LPDA) within fiberglass composite [18].

6. Pixelated reconfigurable L-band patch antennas using MEMS [19, 20].

As can be seen in the works outlined above, there is a significant gap in terms of CLAS antenna research in the VHF and UHF frequency ranges. To our knowledge, no work in the VHF frequency range has been reported for composite aircrafts. To note that Characteristic Mode Analyses (CMA) can be a valuable tool for the study of efficient VHF antennas and structures because it can analyze and predict the radiating modes of a structure without any attribution or knowledge to the excitation. This may allow the design of more efficient antennas that can allow broad bandwidths with the help of modal interactions. However, except for the CMA of a bolt-on antenna on a UAV [21] there has been no study reported on a truly structural VHF antenna. Secondly, when it comes to UHF antennas the published work on UHF LPDA within a composite structure focuses on an endfire array only [18]. There is a tremendous need to design and develop structurally integrated antennas that can offer circular polarization with very small cavity depth to ensure low profile and lightweight aircraft. While the VHF concept to be investigated is relevant to VHF communications, SIGINT, and radar, the UHF concept to be studied is relevant to satellite systems such as UHF SATCOM and MUOS.

Therefore, the specific focus of this dissertation are on: (1) Characteristic Mode Analyses (CMA) of both stand alone and structural antennas, (2) CLAS broadband VHF antenna design to overcome the limitation of poor efficiency with external protruding blade antennas, and (3) CLAS circularly polarized broadband spiral antenna design using Electromagnetic bandgap (EBG) materials that can reduce the depth

of the antenna cavity by at least 50%. The primary focus will be on antennas that can be functional and integral to a composite structural panel constrained by the geometrical shapes and materials that are being used in composite aircraft.

1.3 Outline

This dissertation is organized into six chapters. In chapter two, a brief outline on the theory of characteristic modes is presented and terminology relevant to the research presented here is discussed. Chapter two also contains a literature review that covers previous CMA and CLAS research. Chapter three reviews work on the application of CMA to a dipole coated with a sleeve of DNG material. In this work, a MATLAB script was developed to conduct modal analysis first on a dipole of 0.75 mm radius, and then on the same dipole coated with a 0.5 mm thick layer of DNG material. The commercial software FEKO was used to provide corroborating data. Chapter four covers the development of a novel broadband VHF antenna for airfoil integration. The parametric study used to develop and optimize the antenna geometry is discussed, and a method of integrating the antenna with a composite structure is presented. The chapter concludes with a feasibility assessment of a MIMO application based on two such multi-function airfoils. Chapter five reviews the development of a structural EBG to enable a directional, circularly polarized antenna to be integrated with a composite structure. The development of the EBG is discussed followed by the fabrication details for a prototype structure that contains the EBG and a spiral antenna. Results of S_{11} and anechoic chamber tests are then compared to simulated values. Finally, a FEKO model of the EBG assembly installed on a UAV fuselage is used to assess the impact of conductive structural components on radiation patterns. Chapter six contains the conclusion and suggestions for future work.

Chapter 2

Background

Garbacz first proposed the theory of characteristic modes in 1968 [22]. Shortly thereafter, Garbacz and Turpin published a paper that discussed a technique for finding characteristic mode currents on wires of small diameter having a general shape [23]. The approach described in that work involved an analysis of the scattering matrix of a conducting body, specifically the diagonalizing of the matrix. Harrington and Mautz subsequently offered an alternative approach by proposing that characteristic modes could also be determined from the generalized impedance matrix of the conducting body [24, 25]. This approach has garnered much attention because Method of Moments codes provide access to the impedance matrix. While a thorough description of characteristic mode theory can be found in the aforementioned works, a summary of the theoretical work of Harrington and Mautz is provided here.

2.1 Theory of Characteristic Modes

Figure 2.1 depicts a physical scenario that assists in understanding the computation of characteristic modes. An electric field, $\vec{\boldsymbol{E}}_{\boldsymbol{a}}$, is applied to a conductive surface, S. An equation that relates the surface current, $\vec{\boldsymbol{J}}$, on S to the tangential electric field can be defined through the use of a linear operator as in Equation 2.1, where the subscript refers to the tangential components on the surface. The operator L is defined as shown in Equations 2.2 - 2.5, where r indicates a field point, r' denotes a point on the source, and ε, μ, and k, represent the permittivity, permeability, and wave number of free space, respectively [24].

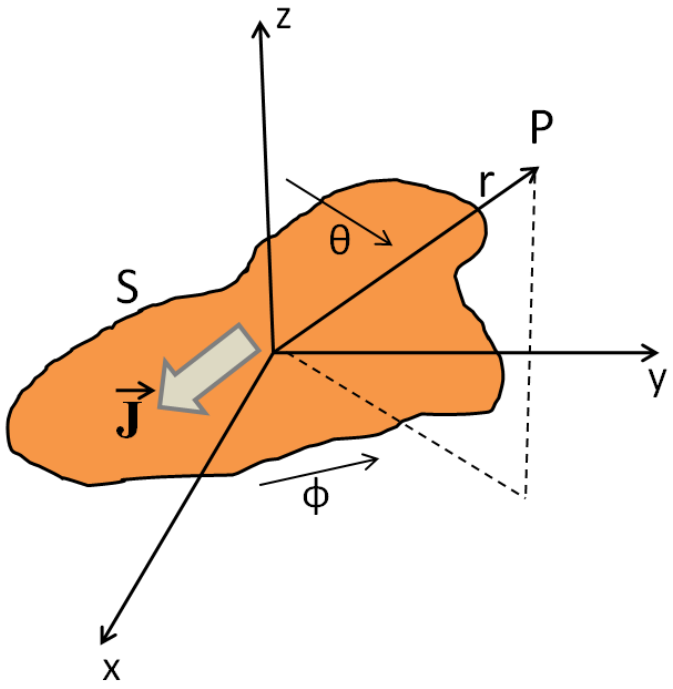

Figure 2.1: Conductive surface and coordinate system for calculation of characteristic modes.

$$|\boldsymbol{L}(\vec{\boldsymbol{J}}) - \vec{\boldsymbol{E}}_a|_{tan} = \boldsymbol{0} \tag{2.1}$$

$$\boldsymbol{L}(\vec{\boldsymbol{J}}) = j\omega \boldsymbol{A}(\vec{\boldsymbol{J}}) + \boldsymbol{\nabla}\boldsymbol{\Phi}(\vec{\boldsymbol{J}}) \tag{2.2}$$

$$\boldsymbol{A}(\vec{\boldsymbol{J}}) = \mu \oiint_S \vec{\boldsymbol{J}}(\boldsymbol{r}')\, \psi(\boldsymbol{r}, \boldsymbol{r}')\, \mathrm{d}\boldsymbol{s}' \tag{2.3}$$

$$\boldsymbol{\Phi}(\vec{\boldsymbol{J}}) = -\frac{\boldsymbol{1}}{j\omega\epsilon} \oiint_S \boldsymbol{\nabla}' \cdot \vec{\boldsymbol{J}}(\boldsymbol{r}')\, \psi(\boldsymbol{r}, \boldsymbol{r}')\, \mathrm{d}\boldsymbol{s}' \tag{2.4}$$

$$\psi(\boldsymbol{r}, \boldsymbol{r}') = \frac{\boldsymbol{e}^{-jk|\boldsymbol{r}-\boldsymbol{r}'|}}{\boldsymbol{4\pi}|\boldsymbol{r}-\boldsymbol{r}'|} \tag{2.5}$$

From a physical perspective, the electric field intensity, $\vec{\boldsymbol{E}}$, at any point in space (e.g. point P in Figure 2.1) due to the surface current on S is given by -L(J). Fur-

thermore, the linear operator, L, in Equation 2.2 has the units of impedance and can thus be expressed as shown in Equation 2.6.

$$\boldsymbol{Z(J)} = [\boldsymbol{L(j)}]_{tan} \tag{2.6}$$

Harrington and Mautz point out that the impedance operator is complex and can thus be expressed as in Equation 2.7 [24].

$$\boldsymbol{Z}(\vec{\boldsymbol{J}}) = \boldsymbol{R}(\vec{\boldsymbol{J}}) + \boldsymbol{j}\boldsymbol{X}(\vec{\boldsymbol{J}}) \tag{2.7}$$

Harrington and Mautz further state that the characteristic current modes can be determined as the eigenfunctions of a particular weighted eigenvalue equation of the form shown in Equation 2.8 and showed through additional work that such an equation can be solved by reducing it to matrix form using Galerkin formulation, as shown in Equation 2.9 [25].

$$\boldsymbol{X}(\vec{\boldsymbol{J}}_n) = \boldsymbol{\lambda}_n \boldsymbol{R}(\vec{\boldsymbol{J}}_n) \tag{2.8}$$

$$[\boldsymbol{X}]\vec{\boldsymbol{J}}_n = \boldsymbol{\lambda}_n [\boldsymbol{R}]\vec{\boldsymbol{J}}_n \tag{2.9}$$

In matrix form, R and X represent the real and imaginary part of the impedance matrix of the conducting body, λ_n are the eigenvalues, and $\vec{\boldsymbol{J}}_n$ are the eigencurrents. This is significant because calculation of the impedance matrix is an essential process in commercially available method of moments (MoM) codes. As a consequence, computation of eigencurrents and eigenvalues can be included as a feature in commercial codes, as has been done with FEKO, or the impedance matrix can be exported and custom code can be developed to calculate λ_n and $\vec{\boldsymbol{J}}_n$. For example, the MATLAB function *eig()* can be used to directly return the eigenvalues and eigenfunctions of a matrix.

Characteristic modes are real surface currents on a conducting body that can produce a radiated field. These currents are entirely dependent on the shape and make-up of the body and are independent of excitation. The remainder of this chapter deals with salient terminology related to characteristic modes.

2.2 Eigenvalues

For each characteristic mode, there is an associated eigenvalue, sometimes referred to as a characteristic number, which conveys important information about the mode itself. To illustrate this, the first three eigenvalues for a 750 MHz, thin wire, half-wave dipole antenna are calculated and plotted versus frequency in Figure 2.2. In general, the magnitude of the eigenvalue, $|\lambda_n|$, is a figure of merit that indicates how well a given mode radiates. Modes for which $|\lambda_n|$ is small are the most effective radiators, while large values of $|\lambda_n|$ indicate that a mode is a poor radiator [26]. Resonance is indicated when the value of λ_n is zero. The sign of λ_n also conveys information about how a particular mode tends to store energy. Magnetic energy storage is indicated by positive eigenvalues, while electric energy storage is indicated by negative eigenvalues [27]. Thus, as seen in Figure 2.2, the first eigenvalue is zero at 750 MHz, indicating resonance, and the two higher order modes have large negative values. The latter condition indicates that the modes in question contribute little to the radiated power and act in a capacitive manner (i.e. storing electric energy). Furthermore, all of the modes take on positive values after the zero crossing, indicating inductive behavior.

2.3 Modal Significance

Eigenvalue data can be used to define another concept known as modal significance. Mathematically, as described by Murray et al. [28], modal significance can be defined as shown by Equation 2.10.

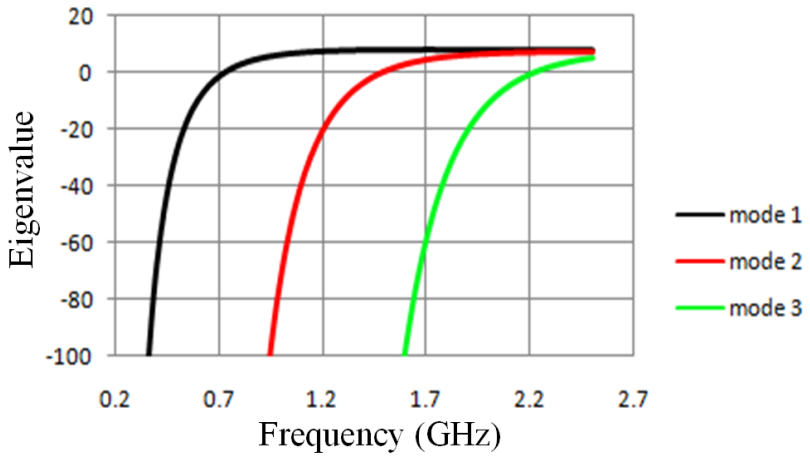

Figure 2.2: First three eigenvalues for a 20 cm, 750MHz half-wave dipole antenna with 1 mm diameter.

$$\boldsymbol{MS} = \left| \frac{\mathbf{1}}{\mathbf{1} + \boldsymbol{j\lambda_n}} \right| \tag{2.10}$$

Modal significance is an inherent property of a mode that indicates the degree to which the mode can couple with an external source. Figure 2.3 shows a modal significance plot that was created using Equation 2.10 and calculated eigenvalue data for a 33.3 cm, 450 MHz half-wave dipole antenna having a radius of 1 mm. For the resonant condition $\lambda_n = 0$, the modal significance achieves its maximum value of one, making the resonant frequencies easy to locate on the plot. The concept of modal half-power bandwidth is also indicated in Figure 2.3. By considering the frequencies at which the modal significance reaches the half power point, defined as in Equation 2.11, the modal half-power bandwidth is defined as shown in Equation 2.12, where f_u and f_l are the upper and lower frequencies at which the modal significance is 0.7, f_r is the resonant frequency (where MS = 1), and the subscript n denotes the n^{th} mode.

$$\boldsymbol{MS} = \left| \frac{\mathbf{1}}{\mathbf{1} + \boldsymbol{j\lambda_n}} \right| = \frac{\mathbf{1}}{\sqrt{\mathbf{2}}} \approx \mathbf{0.707} \tag{2.11}$$

$$\boldsymbol{BW_n} = \frac{\boldsymbol{f_u} - \boldsymbol{f_l}}{\boldsymbol{f_r}} \tag{2.12}$$

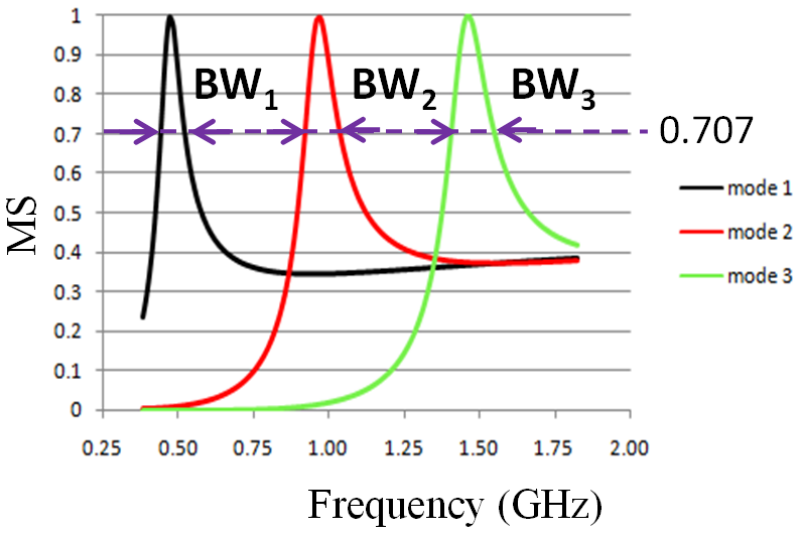

Figure 2.3: Modal Significance for a 450 MHz Dipole Antenna.

A useful application of modal significance is to determine which characteristic modes are significant in terms of contributing to radiated power. A mode is considered significant when $\boldsymbol{MS \geq 1/\sqrt{2}}$ while the case of $\boldsymbol{MS < 1/\sqrt{2}}$ indicates a non-significant mode [29].

2.4 Characteristic Angle

The theory of characteristic modes states that a conducting body can support a set of real characteristic currents that each give rise to a radiated characteristic field $\vec{\boldsymbol{E}}_{\boldsymbol{n}}$. The tangential component of the characteristic field is equiphase at all points on the conductive body and there is consequently a phase lag between the surface currents and the tangential field component. This phase lag can be calculated using the eigenvalues and Equation 2.13 where α_n denotes the phase angle, which is referred to as the characteristic angle. Figure 2.4 shows an example of a characteristic angle plot that was created using the calculated eigenvalue data from Figure 2.2. The characteristic angle can be used to determine a resonant state, which occurs when $\alpha_n = 180°$. This condition is known as external resonance resulting from the case of

$\lambda_n = 0$, and it indicates that the characteristic surface current is 180° out of phase with the tangential component of the radiated field. For the case of the tangential field component and modal surface current being 90° or 270° ($\alpha_n = 90°$ and $\alpha_n = 270°$), the mode is in a condition known as internal resonance and this results in minimal radiated power. The characteristic angle can also indicate the nature of energy storage; with inductive energy storage indicated by α_n having a value between 90° and 180°, and a capacitive mode being indicated when the value of α_n is in the range of 180° and 270° [29].

$$\boldsymbol{\alpha_n = 180° - \tan^{-1} \lambda_n} \tag{2.13}$$

2.5 CMA Literature

One innovation being proposed in this research is the application of CMA in the study and development of CLAS concepts. Because this represents an intersection of two previously unrelated concepts, CMA and CLAS literature will be reviewed in the following two sections. The two topics are then brought together in Chapter 4 where

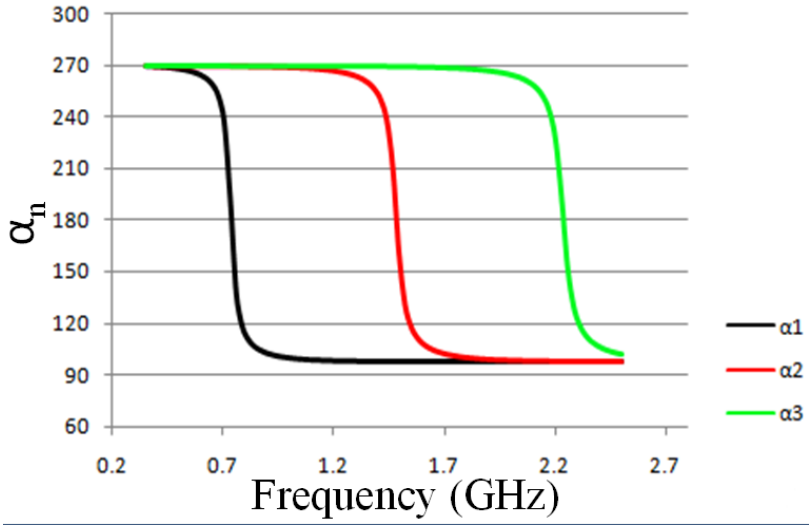

Figure 2.4: Characteristic angle for a 750 MHz diople.

CMA is applied in the development of an airfoil-integrated VHF antenna.

Adams and Bernard investigated the use of CMA to analyze an electrically small antenna with emphasis on antenna tuning and bandwidth enhancement through modal techniques [30]. Figure 2.5 shows the antenna geometry, which is a four-arm TM_{10} monopole. The antenna consists of four dielectric arms of constant radius that are oriented in the $\varphi = 0°$ and $\varphi = 90°$ planes to support helical wires coiled along their length. This structure is bisected in the $\vartheta = 90°$ by a substrate containing a ground plane on the bottom and traces connected to the base of each wire coil on the top. The antenna is fed from the bottom and connects to the intersection of the two traces.

CMA was conducted on the geometry, and the first and second modal currents and their associated characteristic angles are shown in Figure 2.6a and b, respectively. As can be seen on the left of the figure, there is more current in the spherical arms than in the traces for mode 1, but this condition is essentially reversed for mode 2 which has significantly more current in the traces. The characteristic angle plots show that both modes are initially capacitive and mode 1 goes through resonance at 850 MHz and becomes inductive. Mode 2 remains capacitive and ultimately resonates at 1.57 GHz before going inductive. As indicated by the slope of its characteristic angle plot, mode 1 has the lower eigenvalue magnitude over the band of operation and thus provides most of the antenna's radiation. Mode 2 provides capacitive admittance in the antenna's operating band.

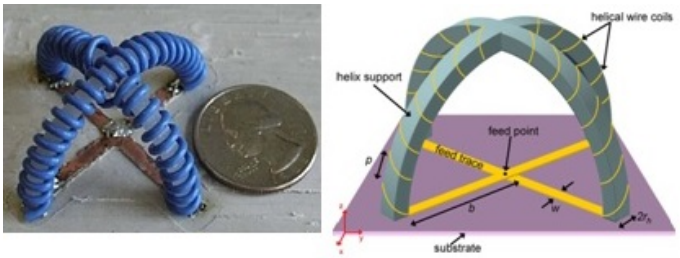

Figure 2.5: Electrically small antenna [30].

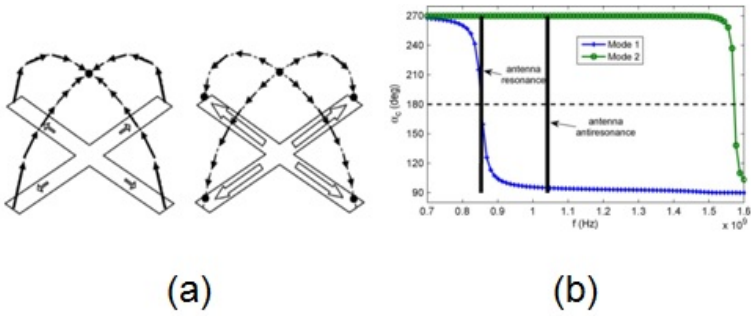

Figure 2.6: (a) Characteristic currents for modes 1 and 2 (b) Characteristic angle plots for modes 1 and 2 [30].

One important concept brought out by this research is the idea that the input admittance of an antenna can be expressed as a sum of the admittances of each of its characteristic modes as in Equation 2.14. A series RLC circuit can be used to model individual characteristic modes because the modes display a decreasing capacitive susceptance before resonance and increasing inductive susceptance after resonance (although it should be noted that some modes never resonate and are purely inductive). Therefore, in the case when a conductive body supports multiple modes, it is analogous to connecting RLC resonators in parallel since the admittances add as indicated by Equation 2.14. Figure 2.7 thus represents a circuit model for the input impedance of an antenna from a characteristic mode perspective with the dots on the right indicating that higher order modes are considered to be open circuits. This circuit model implies that antenna resonances and anti-resonances occur for different reasons. A resonant condition arises from a single dominant mode, while anti-resonance comes about due to the interaction of multiple characteristic modes, some being capacitive in nature and some being inductive modes that could be either a non-resonant type or a mode that is above resonance. This idea of interaction between modes implies that even non-radiating modes could contribute to antenna performance by essentially acting as additional matching circuits.

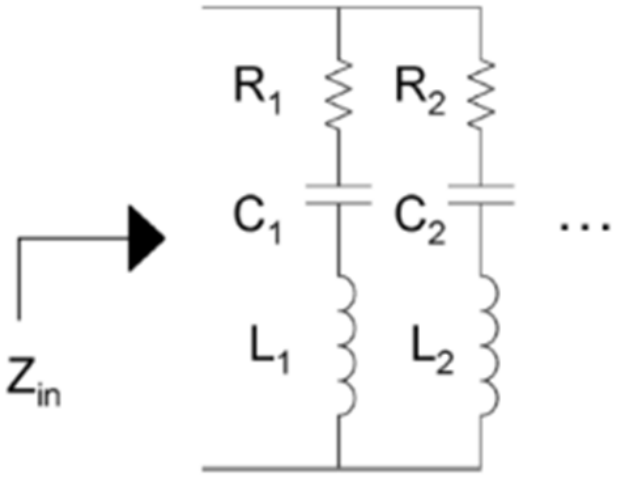

Figure 2.7: Circuit model for antenna input impedance from a CMA perspective [30].

$$\boldsymbol{Y_i n} = \sum_n \frac{\boldsymbol{J_n^2}}{\boldsymbol{1 + \lambda_n^2}} (\boldsymbol{1 - \lambda_n}) \tag{2.14}$$

The use of CMA to study the optimum location to place an antenna on an air vehicle was studied by Chalas [31]. The antenna in this case is considered more of a probe to excite currents on the surface of the aircraft which give rise to radiated fields. This is a concept that was first proposed by Newman [26].

The operation of a general coupled antenna-platform system can be expressed using the Method of Moments (MoM) as in Equation 2.15. In this expression, $[\mathrm{Z_{AA}}]$ and $[\mathrm{Z_{PP}}]$ represent the impedance matrices of the antenna and vehicle, and $[\mathrm{Z_{AP}}]$ and $[\mathrm{Z_{PA}}]$ are the antenna-vehicle mutual coupling matrices. Also $\mathrm{I_A}$ and $\mathrm{I_P}$ are the currents on the antenna and vehicle, and $\mathrm{V_A}$ and $\mathrm{V_P}$ are the antenna and vehicle voltages.

$$[\boldsymbol{Z}]\{\boldsymbol{I}\} = \begin{bmatrix} [\boldsymbol{Z_{AA}}] & [\boldsymbol{Z_{AP}}] \\ [\boldsymbol{Z_{PA}}] & [\boldsymbol{Z_{PP}}] \end{bmatrix} \begin{bmatrix} \{\boldsymbol{I}\}_A \\ \{\boldsymbol{I}\}_P \end{bmatrix} = \begin{bmatrix} \{\boldsymbol{V}\}_A \\ \{\boldsymbol{V}\}_P \end{bmatrix} \tag{2.15}$$

The first step in the process was to analyze the geometry of the aircraft to determine the first four characteristic modes, which can be obtained by performing

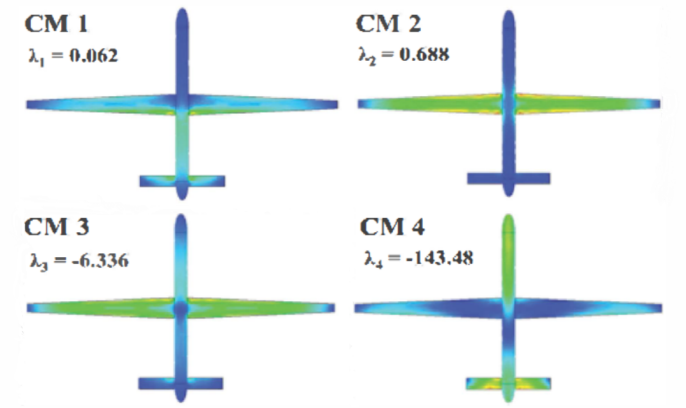

Figure 2.8: First four eigenvalues and characteristic currents for UAV model [31].

modal decomposition on the impedance matrix of the vehicle, $[Z_{PP}]$. The frequency of interest for the study was 11.5 MHz, and Figure 2.8 shows the modal currents and associated eigenvalues for the first four modes supported by the vehicle. The eigenvalues indicate that modes one and two, being close to zero, can radiate efficiently, while the larger eigenvalues for modes three and four indicate these modes more reactive in nature - especially in the case of mode four.

The coupling between the antenna and vehicle was then investigated by assuming that an electrically small, inverted L antenna (ILA) was to be placed somewhere along the top of the fuselage and the location was varied while observing the effects on the 3 dB bandwidth of the ILA. Figure 2.9 shows the results of the analysis, with the x-axis denoting the ILA location expressed as a ratio of position to overall fuselage length, x/L. As indicated by the plot, the bandwidth is larger when the antenna is located near the tail and reaches a minimum value when the antenna is positioned at the midpoint of the fuselage. Thus a strategic choice of antenna location results in increased bandwidth.

To highlight the effect of antenna location on bandwidth enhancement, the power excited by each characteristic mode as a function of location was computed. Figure 2.10 shows a plot of normalized power for each characteristic mode on the vehicle

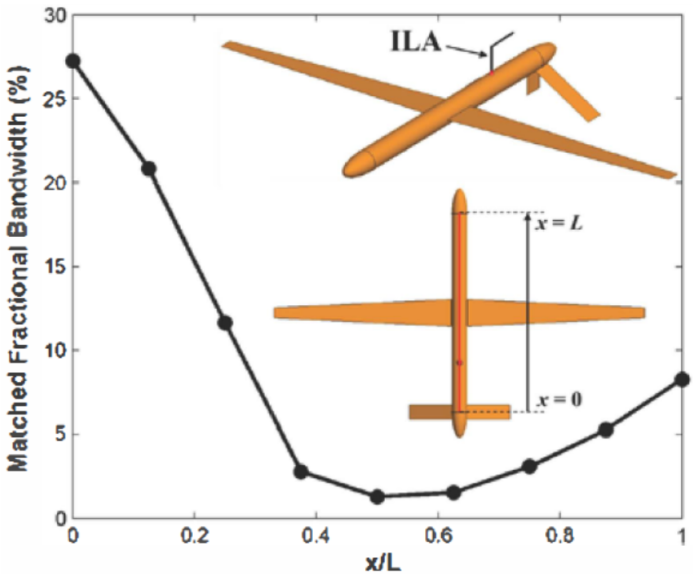

Figure 2.9: Matched 3 dB fractional bandwidth seen at the antenna input when mounted on UAV[31].

versus antenna location, which is once again expressed as the ratio of x/L. The plot clearly shows that the most power is radiated by the first mode when the ILA is near the tail where coupling is maximized. As the ILA is moved toward the center of the fuselage, coupling to the vehicle and radiated power decrease, and only the antenna radiates when positioned at the midpoint of the fuselage. As the ILA is moved toward the front of the vehicle, coupling to modes one and three increases, and there is an associated increase in radiated power.

The idea of exciting surface currents by locating antennas to promote coupling to the aircraft structure was taken a step further by Chen and Wang [21]. In this work, the authors not only wanted to exploit coupling to set up radiation from the vehicle itself, they also sought to control the direction of propagation. The vehicle considered in this study was UAV and the physical model used in the research is shown in Figure 2.11. It should be pointed out that the vehicle size is scaled down to the UHF range from HF in order to accommodate anechoic chamber size constraints. All work in this study was done at 800 MHz, and the desired radiation patterns were assumed to

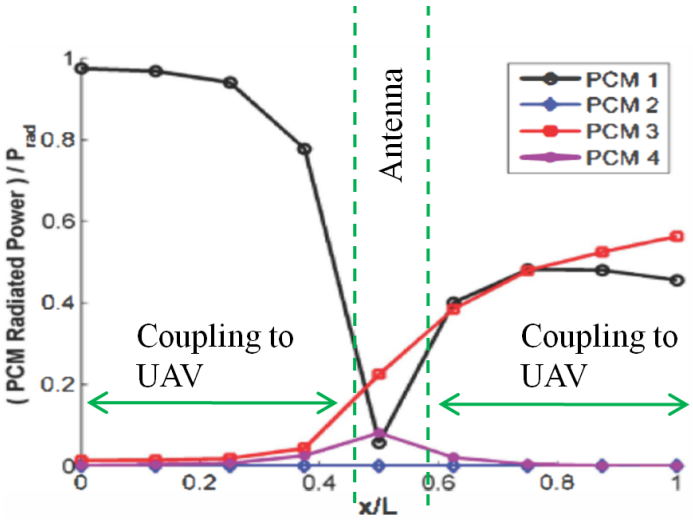

Figure 2.10: Power radiated by each of the first four vehicle characteristic modes as a function of location on fuselage [31].

Figure 2.11: Laboratory model of a metallic air vehicle [21].

be directed upward, to the front, and to the rear.

As in the previous study, the first step in the process was to analyze the structure to determine the nature of the characteristic modes supported by the UAV. The first four modes and associated radiation patterns are shown in Figure 2.12. With the characteristic modes determined, multi-objective optimization software was used to calculate the currents necessary to establish the desired radiation patterns. Inputs to the software included the design objectives of beam direction, front-to-back ratio, and gain along with data on the first ten characteristic modes. The software then

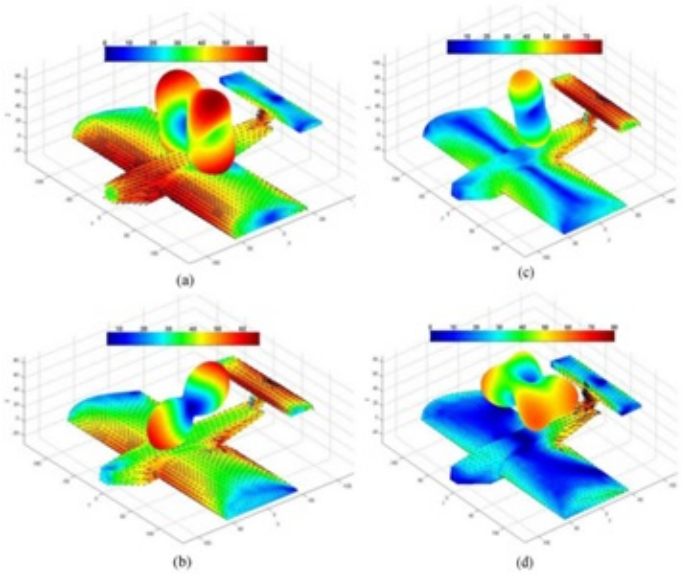

Figure 2.12: Characteristic currents and fields for a) mode 1, b) mode 2, c) mode 3, d) mode 4 [21].

manipulates modal coefficients to synthesize surface currents and radiated fields and seeks convergence between these quantities and objective functions derived from the design goals and input data. The output of the optimization software is a set of synthesized current and field solutions from which a particular solution can be selected manually. Figure 2.13 show the results of the optimization process, with real and imaginary currents shown on the surface of the aircraft and the resulting radiated fields for each case. It is interesting to note that the current excitation required to produce the forward and rearward beams differ only by a 180° phase reversal of the imaginary current.

To enable experimental validation of the simulated results, two antennas, a slot monopole and inverted F, were designed and are shown in Figure 2.14a and b. It is important to note that these antennas were optimized for use as probes to excite the surface currents shown in Figure 2.13, and S_{11} was on the order of -5 dB when measured with antennas isolated from the structure. A one-to-three power divider was designed to equally divide the input power among three output channels and also introduce a 120° and 180° phase delay at output ports 2 and 3, receptively. The

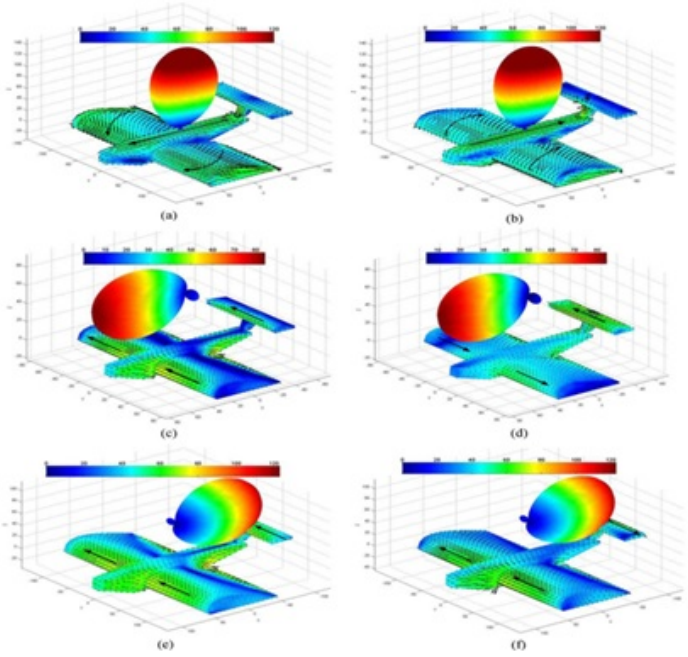

Figure 2.13: Synthesized real (right) and imaginary (left) currents and radiated fields resulting from the optimization process [21].

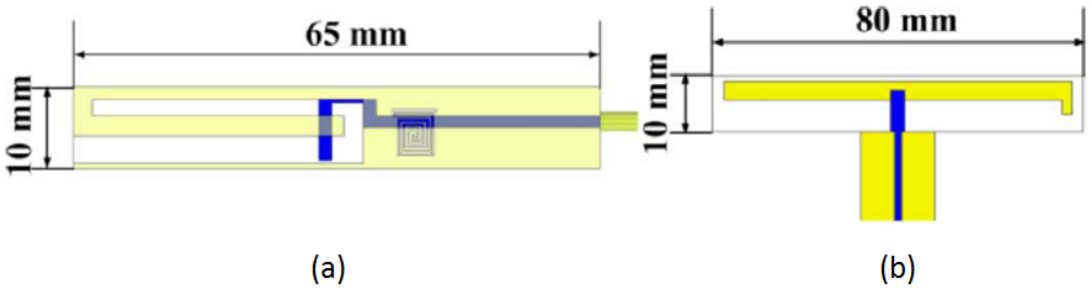

Figure 2.14: a) Slot monopole antenna. b) Inverted F antenna [21].

slot monopoles were attached to the wing of the vehicle model such that the ground plane was shorted to the wing, as seen in Figure 2.11, and the inverted F probe was attached to the tail of the model.

Measurements were conducted in an anechoic chamber and Figure 2.15 shows the observed radiation patterns. A comparison with Figure 2.13 reveals that the desired radiation patterns were achieved with peak gains of 3.31, 0.14, and 5.07 dB in the upward, forward, and rearward directions, respectively.

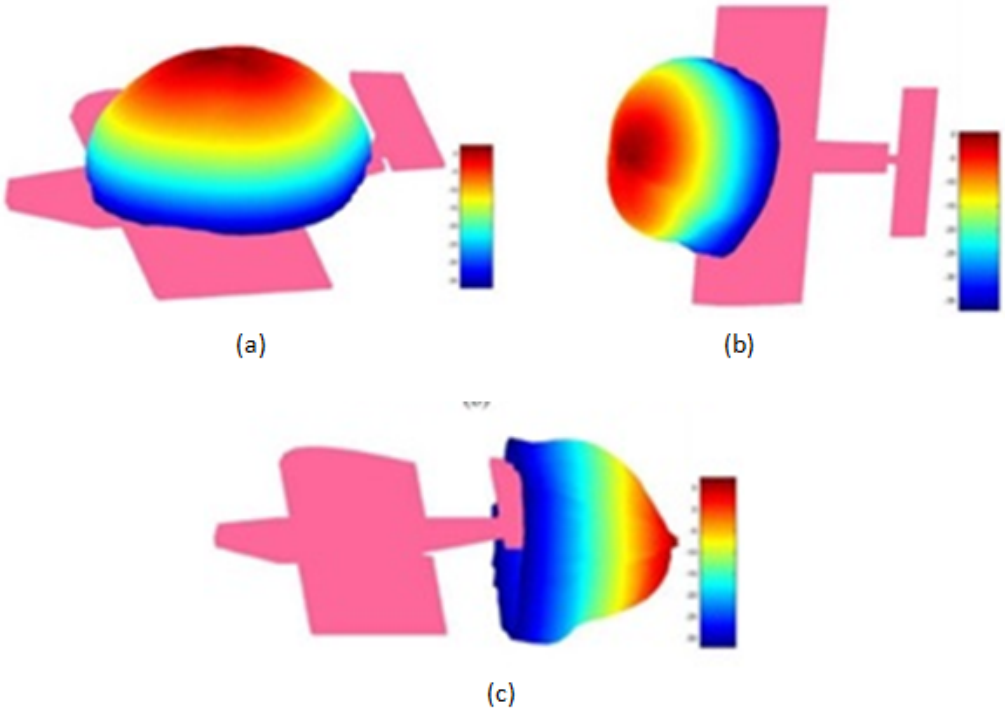

Figure 2.15: Measured data (a) 3dB upward (b) 0.14 dB forward (c) 5 dB rearward [21].

2.6 CLAS Literature

The first project that investigated the concept of load-bearing antennas was the Smart Skin Structures Technology Demonstration (S3TD) [8, 9]. The goal was to integrate a multi-use antenna into a composite panel that could take loads typical of those seen by the fuselage of a fighter aircraft, as indicated in Figure 2.16, and a cross sectional view of the structural antenna concept is shown in Figure 2.17.

The top composite layer, or outer face sheet, provides structural rigidity and environmental resistance and must be fabricated with dielectric materials to allow transmission of electromagnetic fields. The antenna layer is located underneath the face sheet, and the antenna is a four-arm Archimedean spiral that was designed to operate from 200 MHz to 2 GHz. The antenna was fabricated by etching the spiral geometry on a polymeric, non-structural substrate. A layer of dielectric material was placed below the antenna for size reduction purposes, but it plays no structural role.

A section of core material is located below the dielectric layer to provide structural stiffness in conjunction with the inner and outer face sheets. One significant feature of this assembly is the attachment of a non-structural, RF absorber behind the antenna to absorb fields radiated inward. While necessary for RF performance, the absorber and the housing that contains it represent parasitic weight. An alternative to this approach will be explored in Chapter 5. The S3TD program culminated with the successful testing of a 36 by 36 inch antenna panel that withstood strain levels of 4,000 microstrain and loads up to 148,000 kips as well as a buckling load of 4,000 pounds per inch. The panel survived 6,000 hours of fatigue testing and was subsequently tested to ultimate failure which occurred at 150% of design limit load.

In the Structurally Integrated X-band Array (SIXA) project, an effort was undertaken by Boeing and Raytheon to develop a large scale wing component that contained an X band array [16]. The concept was based on a composite sandwich structure in which the walls of an egg crate-shaped core (Figure 2.18a) hosted antenna elements. It should be noted that the core shape represents a trade-off between electrical and mechanical performance. A honeycomb shape provides optimal structural

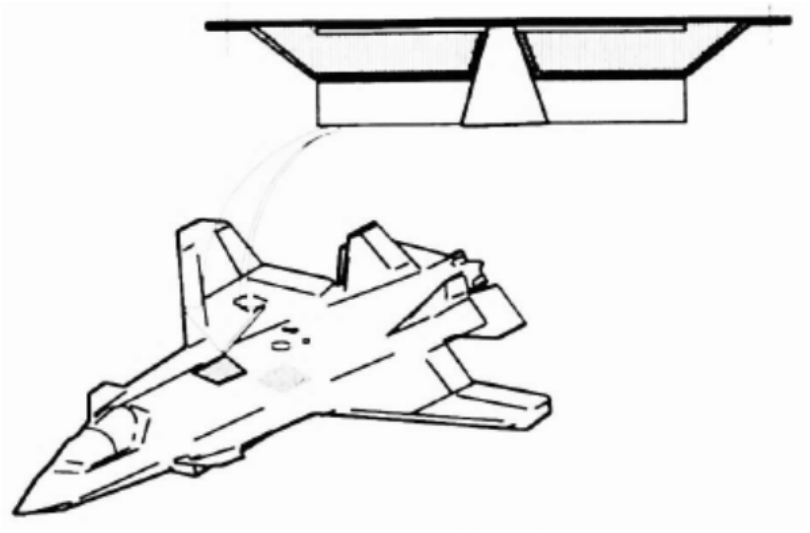

Figure 2.16: Target installation area for Smart Skin Structure Demonstration [8].

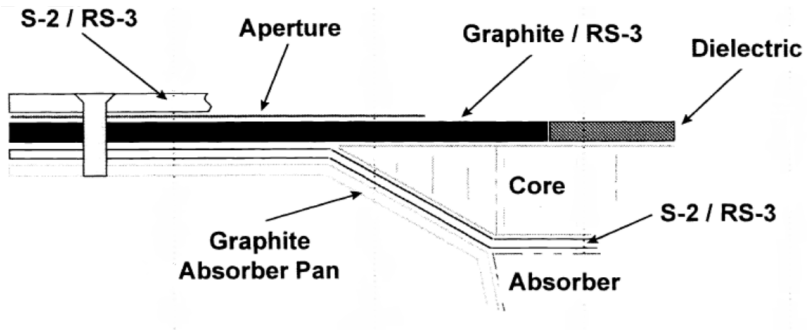

Figure 2.17: Cross-sectional view of S3TD assembly [8].

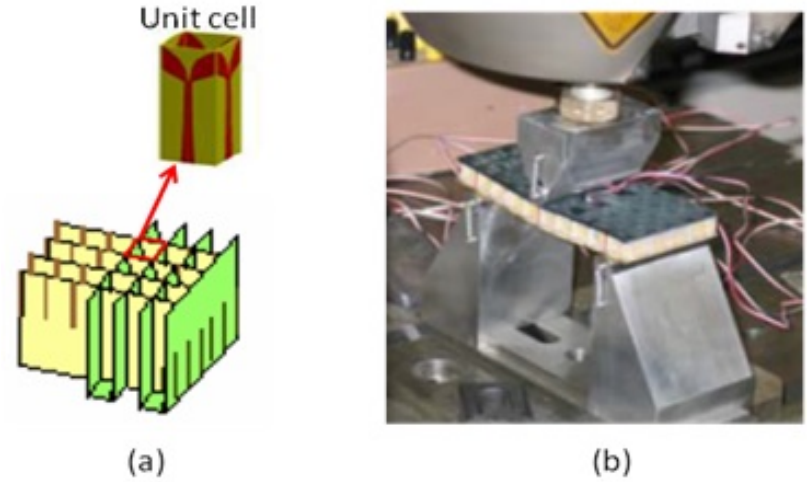

Figure 2.18: (a) Egg crate core section and unit cell depicting antenna elements (b) 3 point bending test of structural coupon [16].

performance, but the egg crate shape enabled a dual polarized array as is shown on the unit cell in Figure 2.18a.

The project followed an incremental implementation approach in order to reduce risk, beginning with materials study, design of skins to act as backplane and radome, and manufacturing trials and testing such as the three point bend test shown in Figure 2.18b. Another critical aspect was the development of an electrical interconnect method because the transmit/receive electronics were attached to the inner mold line of the structure, as depicted in Figure 2.19. The RF signals thus needed to be routed through the inner mold-line to the antenna elements. The interconnects therefore need to maintain good RF performance (e.g. low loss, impedance matching) while

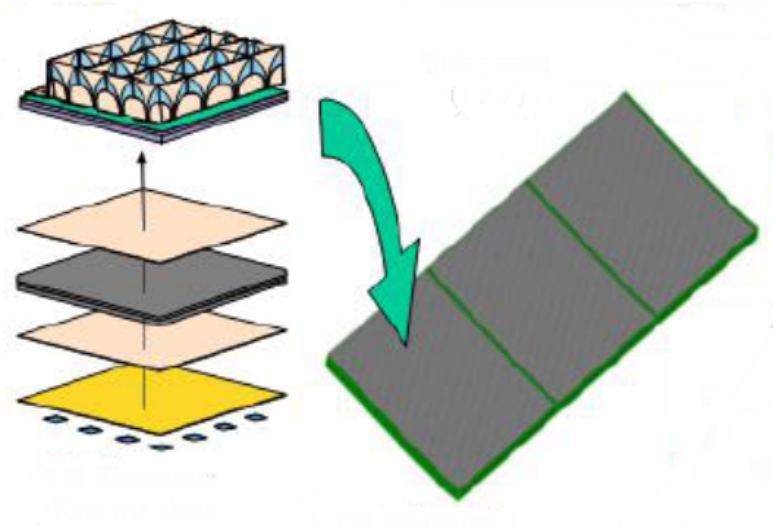

Figure 2.19: RF electronics are mounted on the inside of the structure [16].

withstanding high strain, temperature fluctuations, and mechanical fatigue.

This work ultimately resulted in the production and testing of a large scale wing box assembly. Figure 2.20 depicts the wing box assembly mounted in a test fixture in which four trunions and eight actuator/supports are used to enable application of a combination of bending and torsion loads. The initial mechanical tests went to design limit load conditions and included tension and compression panel bending, torsion, and combined loads. Review of test data did not indicate any structural or electrical interconnect failures (a subset of vias were monitored for continuity). Upon completion of the design limit tests, the wing box underwent two lifetimes of fatigue testing in three temperature regimes: room temperature, -60° F, and 160° F. Once again, review of the fatigue test data showed no indication of failure for either the structure or the electrical interconnects. Four additional test conditions were then executed to consider effect of gust load conditions. The final test on the wing box went to failure (in compression) which occurred at 5,700 microstrain. This project demonstrated the feasibility of both the structurally integrated array and the idea of mounting electronics conformal to the structure.

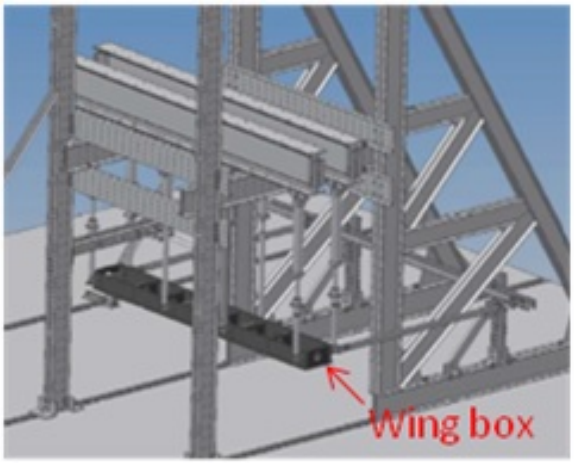

Figure 2.20: Wing box assembly mounted in a test rig [16].

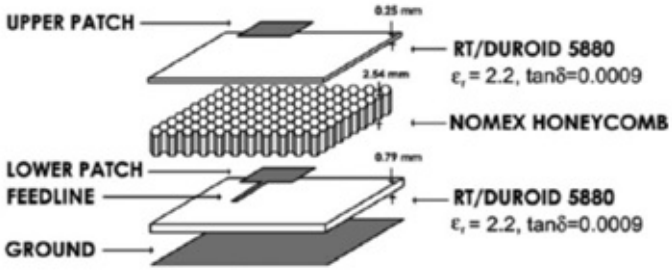

Figure 2.21: Antenna concept for structural integration [17].

Another approach for integrating an antenna with a composite structure was investigated by You et al. [17]. This work also incorporated a sandwich structure and was aimed at addressing the trade-off between electrical and structural performance. Figure 2.21 shows a stacked microstrip patch antenna concept that was considered for integration. The antenna is fabricated using Rogers Duroid 5880 boards that are typically used for RF circuitry and antennas. A unique feature in this case is the use of a 2.54 mm thick layer of Nomex honeycomb core material typically used in composite structures to separate the two patch layers.

The proposed structural integration scheme for the antenna is depicted in Figure 2.22. The antenna assembly is inserted as an inclusion between the lower layer of Fiberglass/epoxy skin and Nomex core in a composite sandwich structure. The core

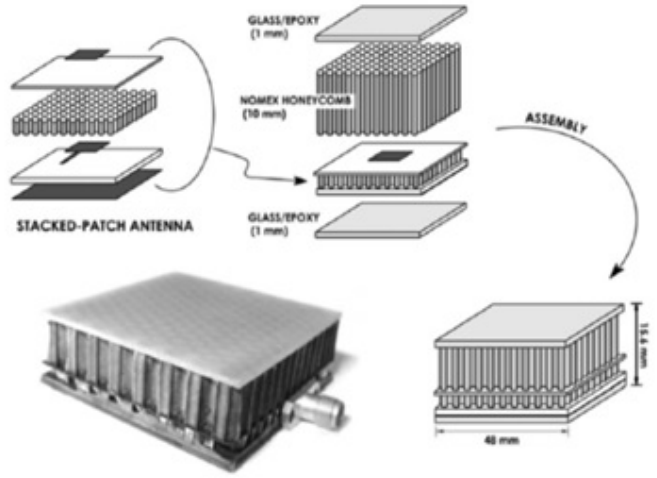

Figure 2.22: Integration of antenna into sandwich structure [17].

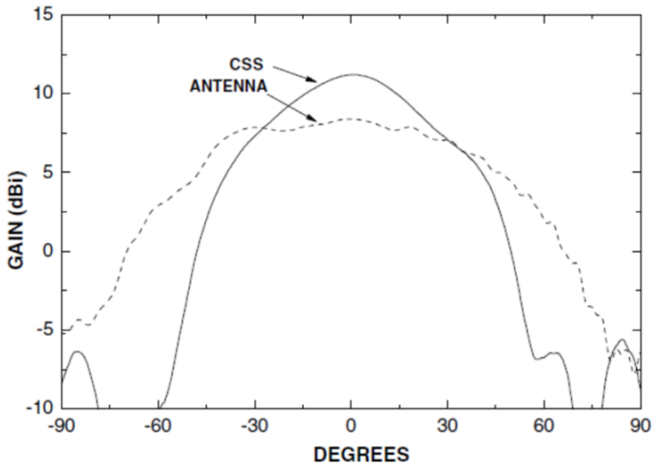

Figure 2.23: Comparison of gain of antenna alone versus structural antenna [17].

of the sandwich structure and the thickness of the upper skin were sized to enhance the electrical performance, and the effect of this approach can be seen in Figure 2.10. The dashed line in the figure indicates that the antenna alone had a peak gain of about 7.5 dBi and a half power beam width of approximately 100°. However, as indicated by the solid line, when the antenna is included in the composite structure, the beam is much more focused and the peak gain approaches 12 dBi.

While this is a good illustration of leveraging the size and material properties

of structural composite materials to enhance RF performance, it should be pointed out that the structure was sized solely to achieve improved RF performance. No indication was given in this work that mechanical loads of a specific vehicle or class of vehicles were taken into consideration.

Another CLAS concept based on a sandwich structure is the reconfigurable Yagi-Uda developed by Wright et al. [32]. The antenna in this case is formed using an array of metallic pixels as seen in Figure 2.24. A unique feature of this structure is that the metallic elements were created on a polyimide film using ink jet direct write technology. The film was then bonded to the surface of the sandwich structure. In theory, a number of different antenna geometries can be created by interconnecting the pixels with RF MEMS switches. However, this work considered the case of a driven dipole element at the center of the pixel field with switchable reflectors on either side of the driven element. This arrangement is depicted in the inset on the upper left side of the figure. Directors were located in the pixel field outside of each switchable reflector and were made by permanently connecting columns of pixels at the appropriate distance.

The concept of operation is that only the switches on one side of the driven element are active at any time (thus forming a reflector) and the opposite switched structure (with switches off) acts as a director. RF energy can be directed to the left by engaging the switches in the reflector on the right and vice versa. Because a ground plane was included in the lower skin of the sandwich structure, the beam will project at a 45° angle from the surface of the structure.

The measured pattern data at the bottom of Figure 2.24 shows that the antenna structure worked as designed, but the measured S_{11} data on the left shows that the matching could be improved. Given the bonded nature of the structure, adjustments to the feed could not be made. Nonetheless, this work demonstrated not just the feasibility of a structural composite hosting an antenna, but also the feasibility of

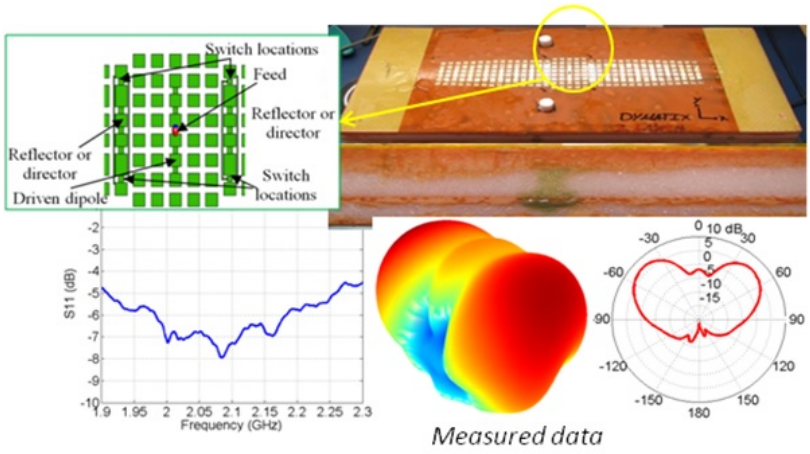

Figure 2.24: Reconfigurable Yagi-Uda antenna in sandwich structure [32].

incorporating RF MEMS switches into a mechanical structure.

Another example of the use of a composite structure to host an integrated antenna was investigated by Bishop [18] et al., and the concept is illustrated in Figure 2.25. The desired RF performance in this case was a linearly polarized directed beam with a bandwidth of over two octaves beginning at 350 MHz and a gain of 6 dBi or more across the band. One significant structural difference in this work was the use of Kevlar to fabricate the dielectric surfaces as opposed to fiberglass used in the previously described research. Kevlar is advantageous from an RF perspective being lower loss than fiberglass (ε_r= 3.85, tanδ= 0.008 at 10 GHz), but can be problematic structurally because it is hygroscopic and weak under compressive loads. Given the desired RF performance, the log periodic dipole array was studied to determine if it could be integrated with the composite structure. Ultimately, the upper and lower dielectric surfaces were used to host the dipole elements and were separated by 2.5 to 5 cm because of structural requirements. Thus, a feed structure was developed to connect to the upper and lower elements while simultaneously maintaining the impedance match. The feed structure consisted of a coaxial cable connected to the elements on the upper surface and a metallic tube that was connected to the dipole

arms on the lower surface. An important fabrication detail is that the connections were made with conductive epoxy which accounted for bending or flexing of the structure under mechanical loading. At the narrow end of the array, the center conductor of the coaxial cable was connected to the metallic tube to complete the feed assembly, as shown in the lower portion of Figure 2.25. It should also be noted that a meander line approach was used for the dipole arms to meet space constrained applications such as found on small UAVs.

A prototype of the antenna was fabricated to assess performance of the feed assembly and manufacturing techniques. A photo of the prototype is shown in the inset in Figure 2.26. Of critical concern was maintaining a 3 mm gap between the coaxial cable and feed tube over the length of the array. This was accomplished using 3-D printed spacers that are visible in the photograph. After assessment of the prototype was completed, a structural version was fabricated and subjected to both Mechanical and RF testing. The measured VSWR and gain are shown in the plots on the left and right side of Figure 2.26, respectively. As seen on the plots, the maximum VSWR is 3 around 480 MHz and the gain is 7 dB or more over most of the band.

Finally, the use of a structural stiffener as a slotted waveguide antenna has also been explored by the Australian Defense Science and Technology Orgainsation (DSTO) [33, 15]. Stiffeners are common structural features in aircraft, and Figure 2.27a illustrates one example of a stiffened composite panel which is representative of a hatch cover. The concept is to match the dimensions of the stiffener to those of a standard waveguide, such as the WR-90 investigated by the DSTO. The appeal of this approach is that there is no additional hardware needed because the stiffener provides both a mechanical and electrical function, and there is consequently little, if any, parasitic weight.

The DSTO was interested in developing a waveguide that consisted only of carbon

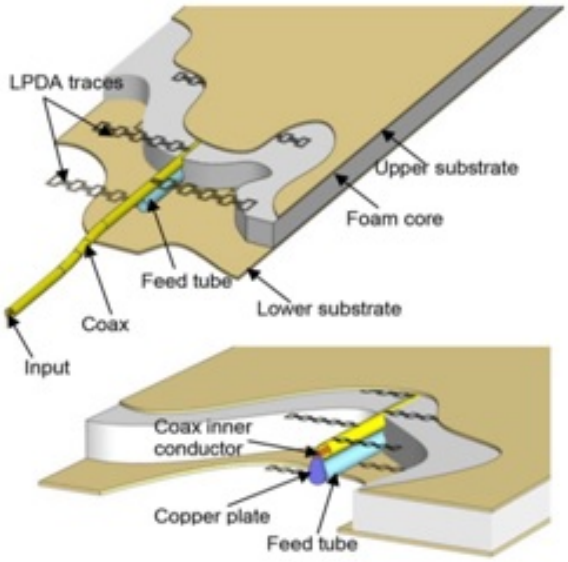

Figure 2.25: Log periodic dipole array hosted in a composite sandwich structure [18].

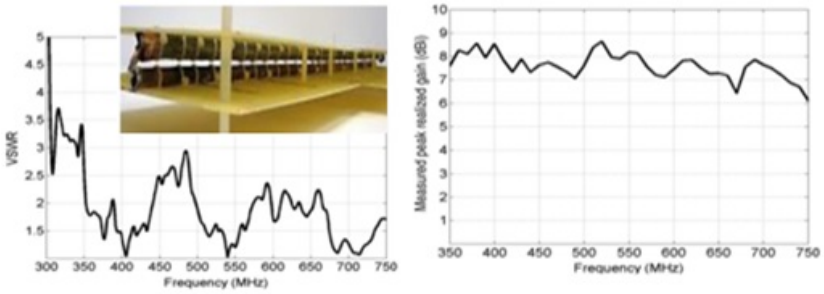

Figure 2.26: Measured VSWR (left) and gain (right) for the structural antenna; prototype in inset [18].

fiber composite and was devoid of any conductive liners or coatings on the interior surfaces. Various stiffener types and orientations were investigated along with a comparison of slots being placed in the long wall versus the short wall. Different slot orientations were also investigated, as shown by the composite panel in Figure 2.27b.

Several experiments were conducted to compare various carbon fiber waveguides having a single radiating slot to metal waveguides of the same configuration. The shape of the radiation patterns were found to be similar; however, the gain of carbon fiber slotted waveguides was found to be 3 dB lower than that of copper. This was

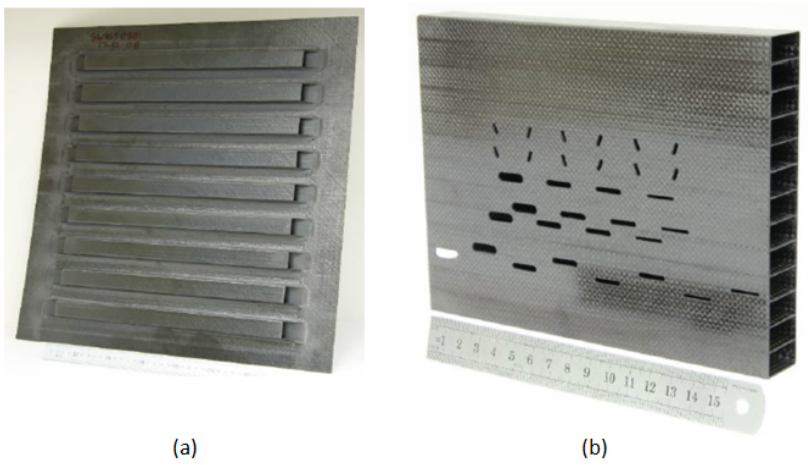

Figure 2.27: a. Stiffened composite panel. b. Stiffened composite panel with various radiating slots. [33].

attributed to the carbon fiber waveguides having an attenuation of 0.05 dB/cm versus 0.001 for copper.

Chapter 3

CMA analysis on a Dipole Antenna Loaded with DNG Material

3.1 Theoretical Approach

While commercial software packages such as FEKO now offer the ability to conduct CMA on complex geometries and materials (which we will do in a subsequent chapter), such an approach does not enable an understanding of the analysis method itself. For that reason, a theoretical study of a half-wave dipole was undertaken to understand the physics of the method and how it works. Previous work by Cabedo [34] covered the application of CMA to a conventional dipole, so this work focused instead on a DNG loaded dipole. Although the study of the impedance response by DNG material loading on a dipole antenna was proposed by Shams and Ali [35], the application of CMA to a DNG loaded dipole is new and thus extends the previous work by Shams and Ali. Specifically, our eigenvalue study sheds new light in terms of its prospects of antenna size miniaturization if DNG materials become available.

The geometry considered in our investigation is depicted in Figure 3.1. The overall length, L, is 30 cm, the wire radius is 0.75 mm, and the DNG material is 0.5 mm thick; thus, the diameter of the wire/sleeve structure is 2.5 mm. The DNG material is assumed to be isotropic and homogeneous.

A study was conducted using the Galerkin Method of Moments (MoM), a detailed description of which can be found in [35]. Under this scheme, the dipole was divided into N segments, with each segment much larger than the radius of the an-

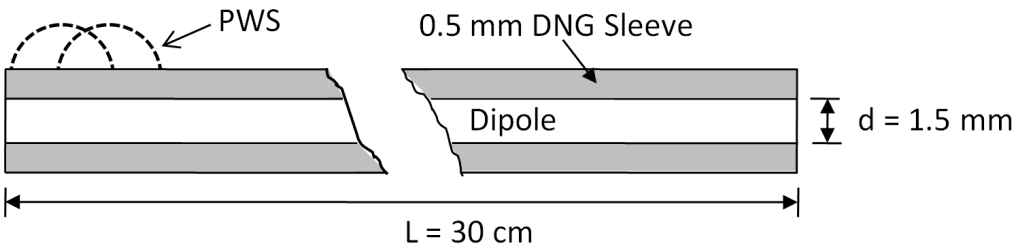

Figure 3.1: Dipole antenna with sleeve of DNG material.

tenna structure, to form what could be viewed as an array of smaller dipoles. The impedance matrix was then found using Equations (3.1) to (3.5) by first calculating the impedance matrix of the dipole in free space (given by Equation 3.1), calculating the effects of material loading using Equations (3.2) to (3.5) (where $F'_m(z)$ and $F'_n(z)$ are the Piecewise Sinusoidal (PWS) basis functions indicated in Figure 3.1, a is the radius of the wire making the dipole, and b is the wire radius plus the coating thickness), and finally calculating the first row of the impedance matrix as given by Equation 3.6. The complete matrix can then be populated using the Toeplitz algorithm, which can easily be accomplished by applying the *toeplitz()* function in MATLAB.

$$\boldsymbol{Z_d = -\left[\int_{z_{n1}}^{z_{n2}} \frac{\sin\beta(z-z_{n1})}{\sin(\beta\Delta)} + \int_{z_{n2}}^{z_{n3}} \frac{\sin\beta(z_{n3}-z)}{\sin(\beta\Delta)}\right] \frac{j30}{\sin(\beta\Delta)}}$$

$$\boldsymbol{\times \left[\frac{e^{-j\beta R_{m1}}}{R_{m1}} - 2\cos(\beta\Delta)\frac{e^{-j\beta R_{m2}}}{R_{m2}} + \frac{e^{-j\beta R_{m3}}}{R_{m3}}\right] dz} \quad (3.1)$$

$$\boldsymbol{Z_e = -\frac{P}{2\pi j\omega\epsilon_0}\int F'_m(z)F'_n(z)\,dz} \quad (3.2)$$

$$\boldsymbol{Z_m = Q\frac{j\omega\mu_0}{2\pi}\int F'_m(z)F'_n(z)\,dz} \quad (3.3)$$

$$\boldsymbol{P = \frac{\epsilon_2 - \epsilon_1}{\epsilon_2} \ln\left(\frac{b}{a}\right)} \tag{3.4}$$

$$\boldsymbol{Q = (\mu_r - 1) \ln\left(\frac{b}{a}\right)} \tag{3.5}$$

$$\boldsymbol{Z_1 = Z_d + Z_e + Z_m} \tag{3.6}$$

3.2 Results of CMA

As pointed out in the previous work by Cabedo[34], MATLAB provides a convenient method to calculate both eigenvalues and eigencurrents through use of the *eig()* function. As depicted in the flow chart of Figure 3.2, this feature can be used to create a plot of eigenvalues versus frequency by implementing a nested-loop script that first calculates the impedance matrix and then calls the *eig()* function to calculate the eigenvalues for that frequency. The highlighted processing block in Figure 3.2 is the impedance matrix calculation described above, and it comprises the inner loop of the script. The impedance matrix must be re-calculated at each frequency because it is frequency dependent. By storing the eigenvalue and frequency data as parallel arrays, it is straightforward to create eigenvalue plots that can be used to determine the resonant frequency of each mode by locating the points at which the eigenvalues cross zero.

Prior to studying the effects of DNG loading, the MATLAB script was used to perform CMA on a dipole with no dielectric and magnetic material loading. Figure 3.3 shows the eigenvalues of the dipole without a sleeve of DNG material, a condition brought about in the script by setting ε_r and μ_r equal to one. It was observed that the first mode resonates at 475 MHz; this is expected because the resonant frequency of a 30 cm long, infinitely thin, half-wave wire dipole is 500 MHz. The next three higher order modes are seen to be resonant at 971 MHz, 1.476 GHz, and 1.971 GHz. Similar

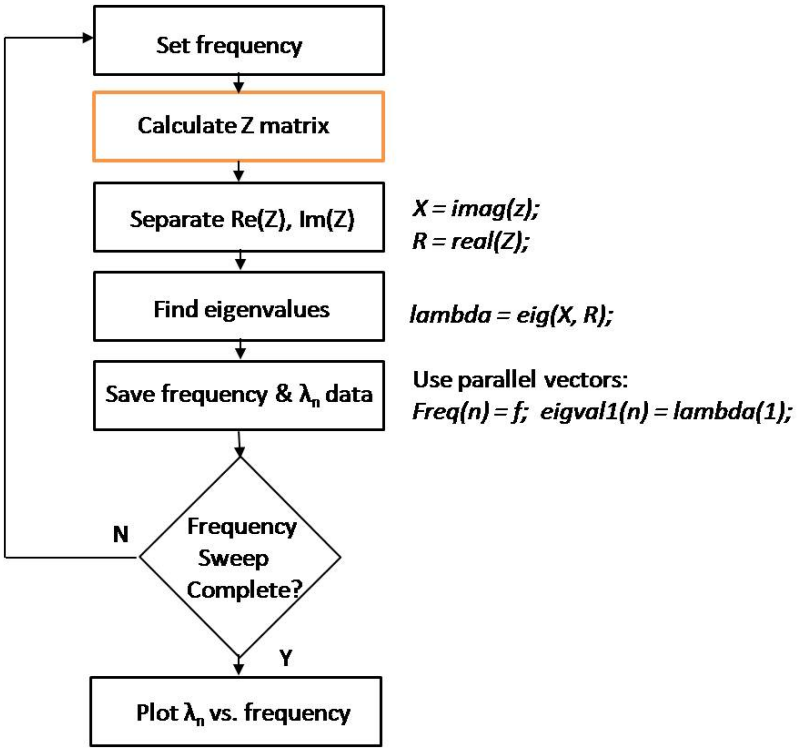

Figure 3.2: Flow chart describing eigenvalue calculation.

studies were also conducted (but not reported here) where other positive values of ε_r and μ_r were considered.

Initially the left-handed material loading study consisted of varying ε_r in a negative sense with $\mu_r = 1$, and resonant frequencies lower than 475 MHz were observed for this condition. Subsequently both ε_r and μ_r being negative were considered. Figure 3.4 is an eigenvalues plot with the DNG sleeve present and $\varepsilon_r = \mu_r = -1$. As indicated by the zero crossing of the first mode, the presence of the DNG material caused the resonant frequency of the first mode to decrease to 467 MHz. It was observed that when the absolute value of ε_r and μ_r were smaller than 1 further reduction in frequency was achieved. For example, the eigenvalues for $\varepsilon_r = \mu_r = -0.6$ are plotted in Figure 3.5. As apparent, the resonant frequency of the first mode now decreased to 430 MHz. The effect of the DNG sleeve on the resonant frequency was observed by sweeping the value of ε_r and μ_r over the range of -0.3 and -1. These data are listed in Table 3.1. Note that for $\varepsilon_r = \mu_r = -0.3$, the resonant frequency is 355 MHz; this value

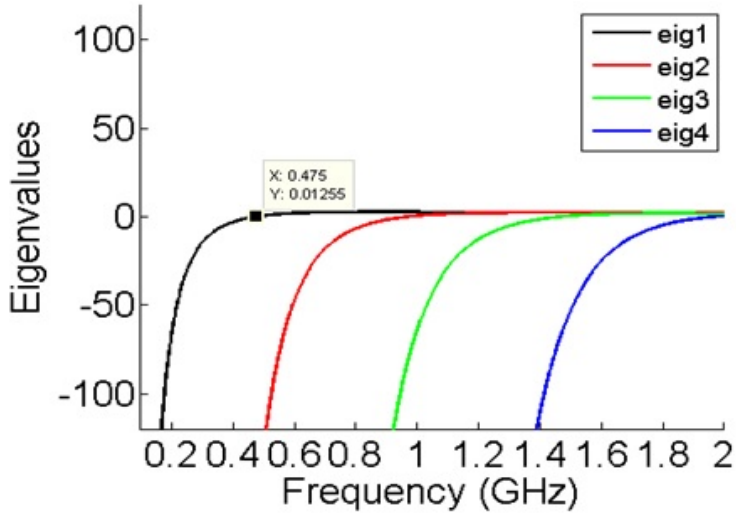

Figure 3.3: Eigenvalues for a 30 cm dipole having a diameter of 1.5 mm and no DNG sleeve.

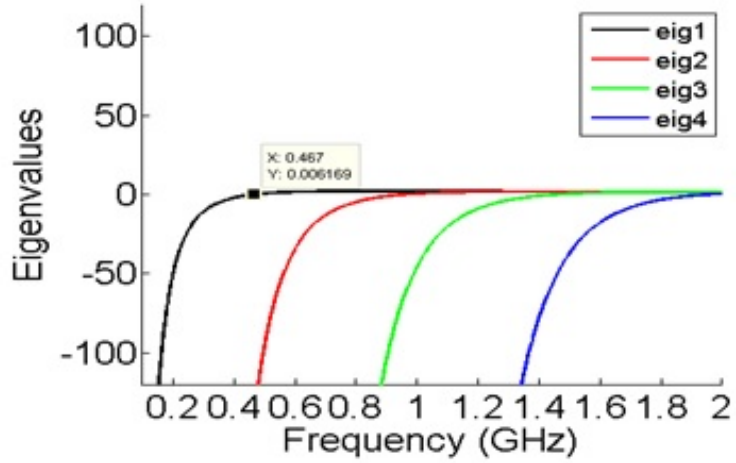

Figure 3.4: Eigenvalues for a 30 cm dipole having a 1.5 mm diameter and a 0.5 mm thick DNG sleeve with ε_r and $\mu_r = -1$

represents an antenna size reduction of 25% over the unloaded dipole. It should be emphasized that the thickness of the DNG material studied here is only 0.5 mm; it is expected that a further reduction in resonant frequency can be realized through the use of a thicker material.

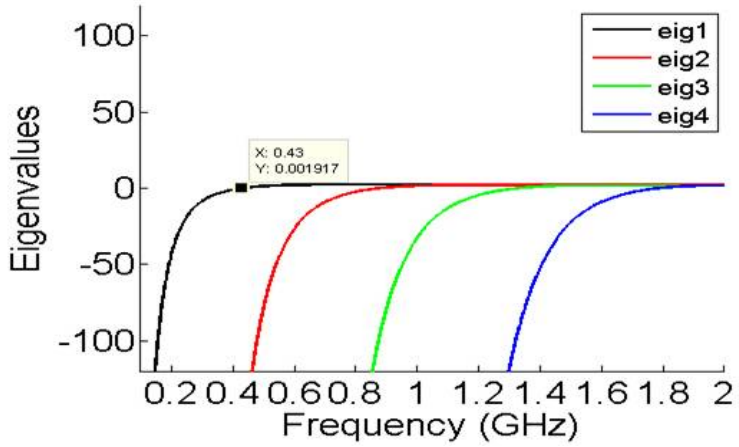

Figure 3.5: Eigenvalues for a 30 cm dipole having a 1.5 mm diameter and a 0.5 mm thick DNG sleeve with $\varepsilon_r = \mu_r$ = -0.6.

Table 3.1: Effect of a 0.5 mm thick DNG sleeve on the resonant frequency of a 30 cm long dipole antenna having a diameter of 1.5 mm.

ε_r,μ_r	Res. Fr. (MHz)	ε_r,μ_r	Res. Fr. (MHz)
-0.3	355	-0.7	442
-0.4	392	-0.8	451
-0.5	415	-0.9	459
-0.6	430	-1.0	467

Chapter 4

Airfoil-integrated VHF Antenna for MIMO Applications

VHF antennas are very important for air-to-ground voice and data communications [36] as well as SIGINT, COMINT, and radar [37]. VHF antennas are also widely used in military land vehicles [38] and shipboard applications. More recently they are being considered for cognitive radio communications and airborne internet service for remote and sparsely populated areas.

Conventional VHF aircraft antennas, such as blade antennas, are electrically small. In order to obtain sufficient bandwidth these antennas are resistively matched which results in very low efficiency. Gain of -20 or -30 dBi at the lower VHF frequencies is fairly common. Additionally, these antennas are usually externally mounted on the aircraft i.e., they protrude from the surface of the aircraft. As a consequence, aerodynamic efficiency is also reduced. While antennas such as annular slots could solve this problem, they have a narrow bandwidth.

Since many aircraft have airfoils such as winglets and various stabilizers that are oriented vertically, or nearly so, a composite airfoil could serve as a structure to host a VHF communications antenna. An airfoil has the general shape depicted in Figure 4.1a. The goal of this work is to design an antenna that lends itself to structural integration with the vertical stabilizer of an aircraft. This approach allows two benefits: (1) a larger, yet conformal, antenna and (2) improved efficiency. For the purpose of this work, the frequency range of 100 to 200 MHz and a nearly omnidirectional

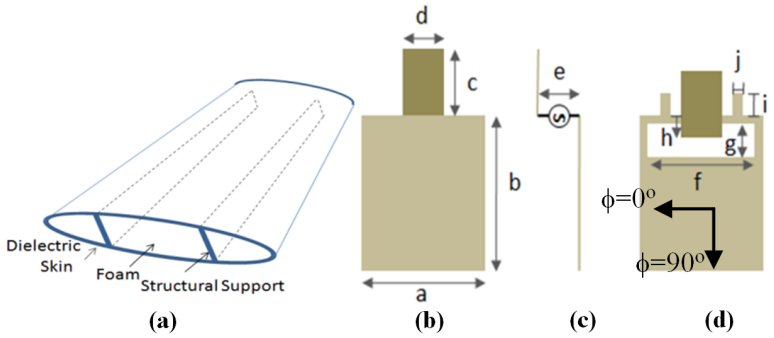

Figure 4.1: (a) Airfoil (b) Antenna geometry.

pattern are considered as performance goals. The choice of this frequency range is simply due to the number of applications in this range such as aircraft air-to-air and air-to-ground communication, RF navigation equipment, emergency locater beacons, marine radio for maritime search and rescue, military ISR and communications, and cognitive radio.

4.1 Antenna Development

The starting point in the development of such an antenna is shown in Figure 4.1b. The basic geometry consists of two conductive rectangular sheets separated by some vertical distance, denoted as e in Figure 4.1c, with the feed located at the midpoint of the two common sides. The size of the large rectangle is ultimately constrained by the size of the air foil, with more space being available span-wise than chord-wise, and we assume a limit of 76 cm x 62 cm for the large sheet. The initial length of the small rectangular sheet was determined by assuming that the antenna is a quarter wave monopole sized to operate at the center of the band of interest (150 MHz). Thus the initial length was determined to be 50 cm; however, the structural composite materials into which the antenna will eventually be placed have a dielectric loading effect. To compensate for this, the initial length for the small rectangle was shortened to 40 cm, which corresponds to an operational frequency of 187.5 MHz in free space. The width of the small sheet is a parameter to be studied and an initial value of 12

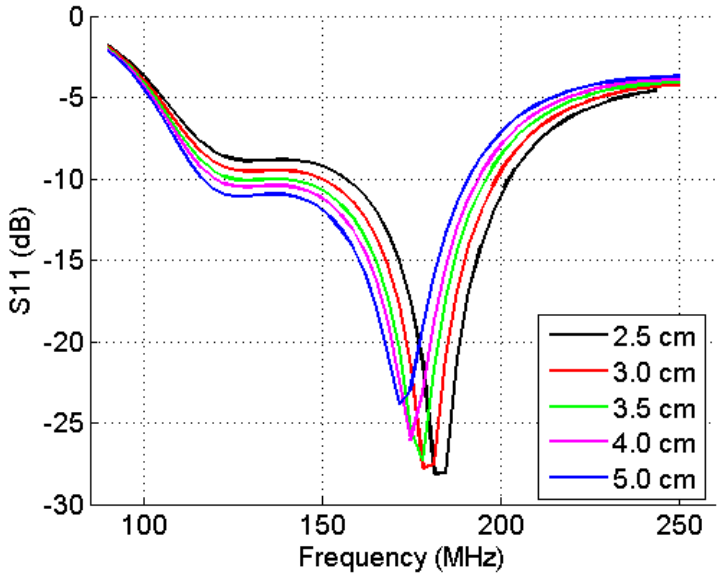

Figure 4.2: Effect of height variation on s11.

cm was assumed.

Antenna analyses and design were performed using FEKO. Figure 4.2 shows how variation in the vertical separation between the two conductive sheets affects the S_{11} performance. Two observations can be made from the plot. The first is that for e = 2.5 cm, a sharp resonance is seen at 185 MHz which agrees well with the resonant frequency of 187.5MHz for a 40 cm monopole. Secondly, it can be seen that the bandwidth increases and frequency of operation shifts lower as the distance between the sheets increases. An initial distance of 3.5 cm was selected because a lower height facilitates integration with an airfoil. The bandwidth within S_{11} < -10 dB is 120 to 200 MHz.

Following a literature example from Hossain [39], two stubs (15 cm x 4 cm) were placed on the edge of the large sheet in order to attain broadband/multiband performance (see 4.1d without the slot). The stubs were located such that the outer edge of each stub was inset 8 cm from the sides of the large sheet. However, despite investigating two sizes and several locations for the stubs, no significant benefit in terms of bandwidth was observed. Nonetheless, the two stubs were left in place and

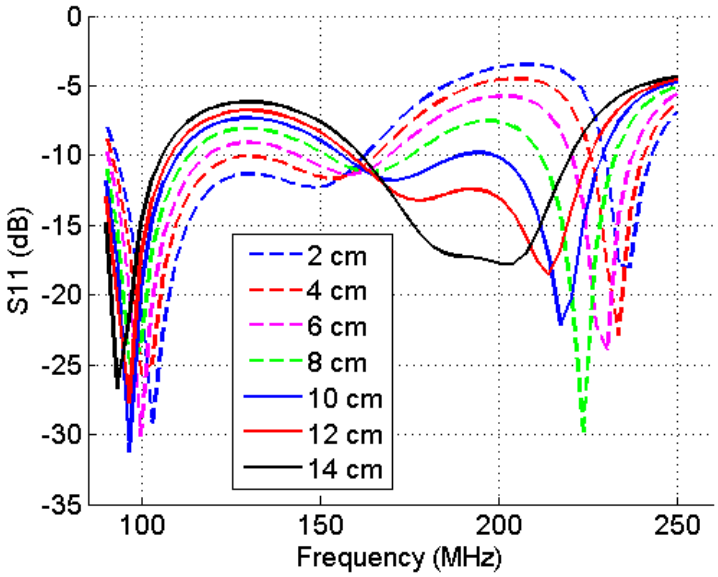

Figure 4.3: Effect of slot width on S_{11}.

the effects of adding a slot next to them were studied.

The location and geometry of the slot can be seen from Figure 4.1d. The impact of the slot was investigated by observing the effect on S_{11} while varying the slot depth (g) in 2 cm increments from 2 cm to 14 cm, and Figure 4.3 shows the data resulting from the simulations. The data show that a narrower slot contributes to bandwidth at lower frequencies while a wider slot increases bandwidth at higher frequencies. The sharp resonance at the high frequencies was determined to be caused by the stubs by repeating the simulation with stubs removed. A key observation is that a 12 cm slot depth provides the upper portion of the desired bandwidth, from 160 MHz to 224 MHz, and also a small segment at the low end of the band from 90 MHz to 106 MHz. Thus, the antenna would meet the desired impedance bandwidth if the match could be improved between 106 MHz and 160 MHz. The effect of the slot was also studied with a Smith chart, with the results shown in Figure 4.4.

As a means of improving the match in the lower portion of the band, an overlap was introduced such that the small sheet extended beyond the edge of the lower sheet with no change in vertical separation between the two. This was introduced in order

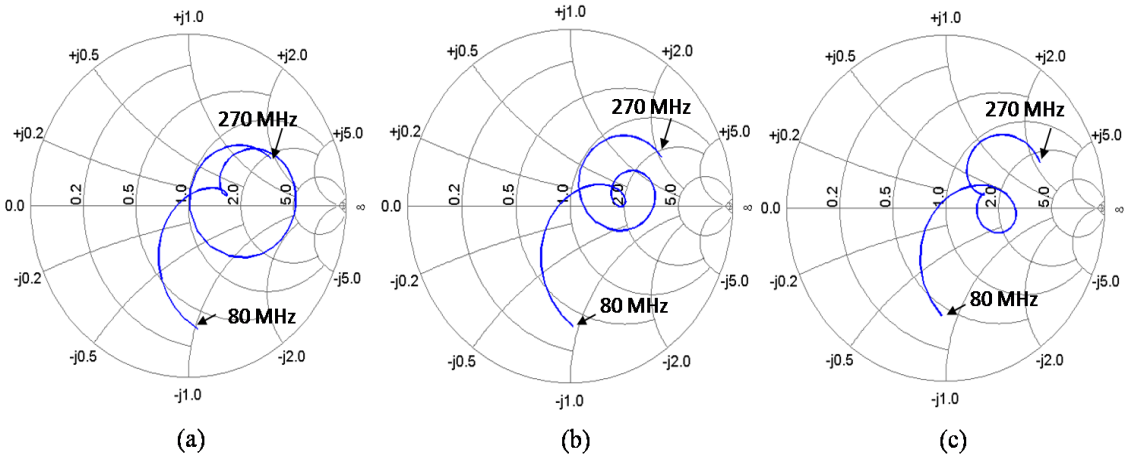

Figure 4.4: Smith charts for slot widths of (a) 2 cm (b) 6 cm and (c) 12 cm.

to control the equivalent shunt capacitance resulting from the sheet overlap, which is in parallel with the feed. Figure 4.5 shows the effect on S_{11} when the amount of overlap between the sheets is increased. As the plot shows, once the overlap reaches 8 cm, the S_{11} is below -10 dB from approximately 95 MHz to 235 MHz. Thus a 2.5:1 bandwidth is achieved. The effect of the overhang was also studied with the Smith chart, and the plots in Figure 4.6 show the results. A shift downward can be seen on the plots as overlap increases, as would be expected for increased capacitance due to a larger overlap area.

Table 4.1 shows the final antenna dimensions with the letters corresponding to the geometric features indicated in Figure 4.1b through d. The simulation showed the impedance bandwidth of the optimized geometry was 145 MHz with s11 less than or equal to -10 dB from 96 MHz to 241 MHz. The simulated pattern shown in Figure 4.7 is consistent over much of the band with some distortion present at the upper end. It should be noted that although Figure 4.7 shows the gain falling to -5 to -10 dBi, this is not necessarily problematic because some commercial blade antennas have a similar gain. For example, Antcom Corporation of Torrance, CA markets two blade antennas with part numbers 12B-20-500-XT-1 and 15B2-20-500-XT-2 that have a specified gain of -3 dBi and -7 dBi, respectively, at 240 MHz [40]. It is also a common

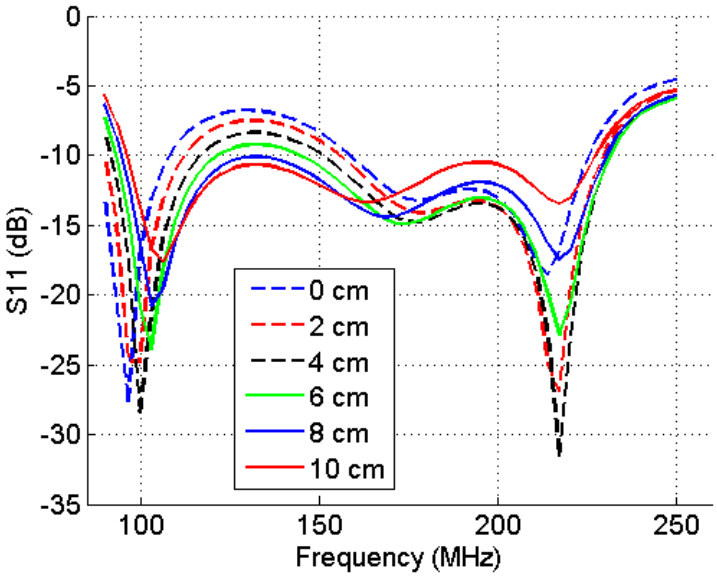

Figure 4.5: Effect of sheet overlap on S_{11}.

practice in industry to specify parameters under the best case conditions on data sheets. Thus, it is reasonable to expect that the antenna developed in this section would perform similarly to commercial products, and that RF systems utilizing this antenna would be able to function across the entire band despite the dips in the pattern at higher frequencies.

Table 4.1: Dimensions of the proposed antenna.

Parameter	cm	Parameter	cm
a	62	f	58
b	76	g	12
c	40	h	8
d	22	i	14
e	3.5	j	6

4.2 Characteristic Mode Analysis

With the initial antenna design in place, characteristic mode analysis was conducted on the antenna using the CMA feature of FEKO. The size of the antenna at VHF

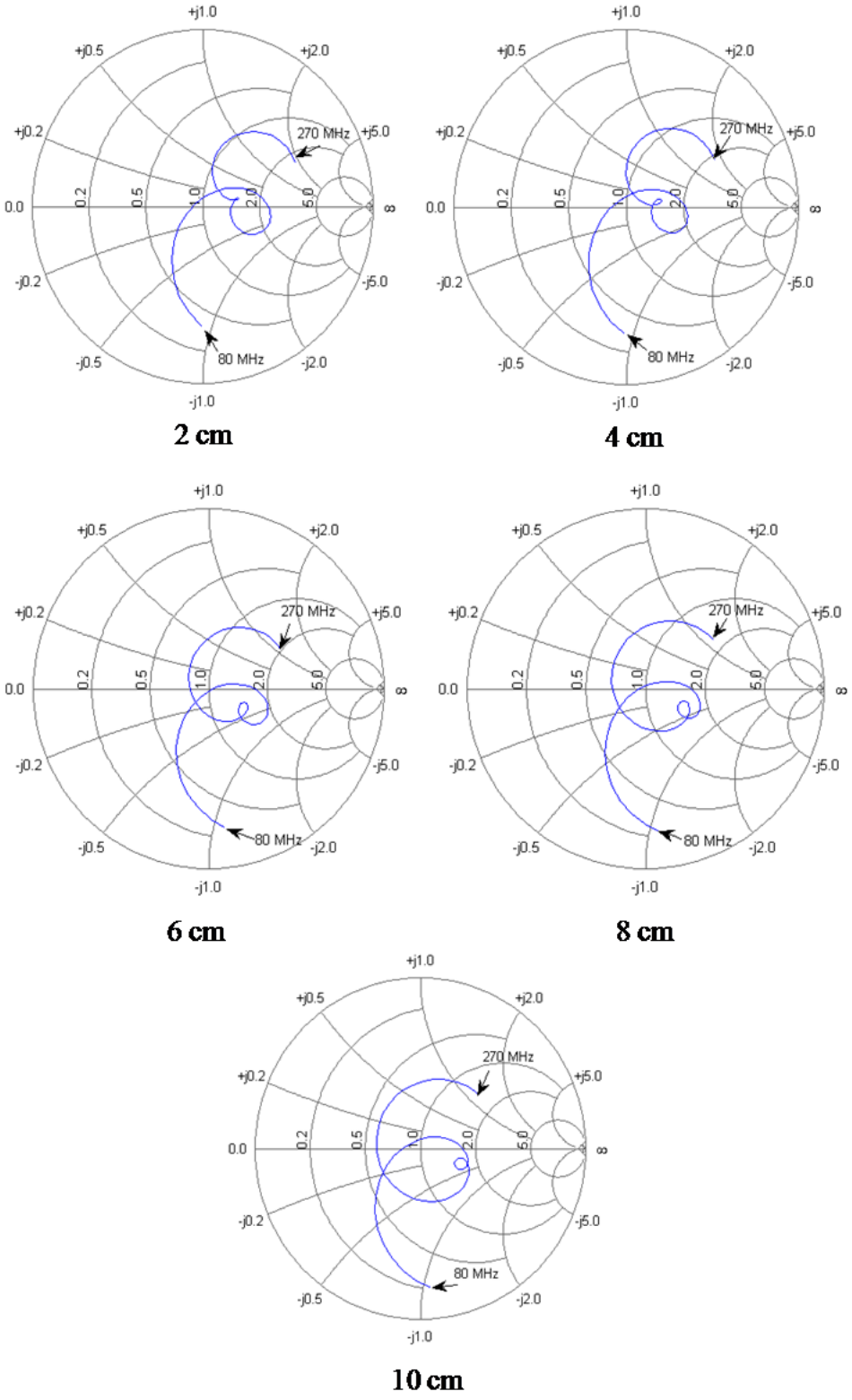

Figure 4.6: Smith charts showing impact of sheet overlap.

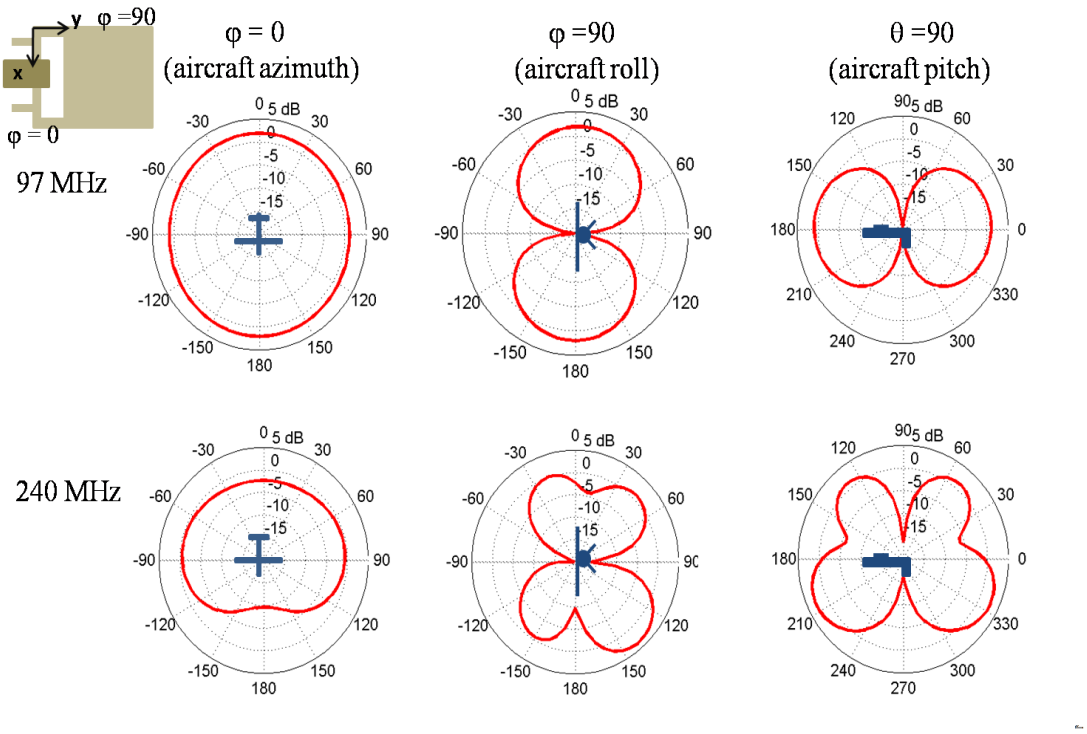

Figure 4.7: Radiation patterns at φ= 0, φ= 90,ϑ= 90 for 97 MHz (top) and 240 MHz (bottom).

frequencies becomes a potential problem when conducting modal analysis because a much finer mesh size is required, and this directly impacts both simulation time and memory usage. Altair's technical support staff for FEKO recommends mesh sizes in the range of $\lambda/20$ to $\lambda/25$. For the antenna under consideration, the upper frequency of 240 MHz implies a mesh size of 5 cm using the $\lambda/25$ constraint. An initial simulation was conducted from 80 to 250 MHz using a mesh with a 5 cm edge length, but a number of mode tracking errors were encountered. These errors result when the software loses track of a mode during the simulation and begins logging data of a previously detected mode under a new mode number, giving the appearance of more modes being present. FEKO detects this condition and issues a warning calling for a finer mesh size. It was determined through experimentation that $\lambda/30$ to $\lambda/35$ was the mesh size needed to reduce the occurrence of mode tracking errors for the VHF antenna. It should be noted that despite using a workstation with 16 cores and

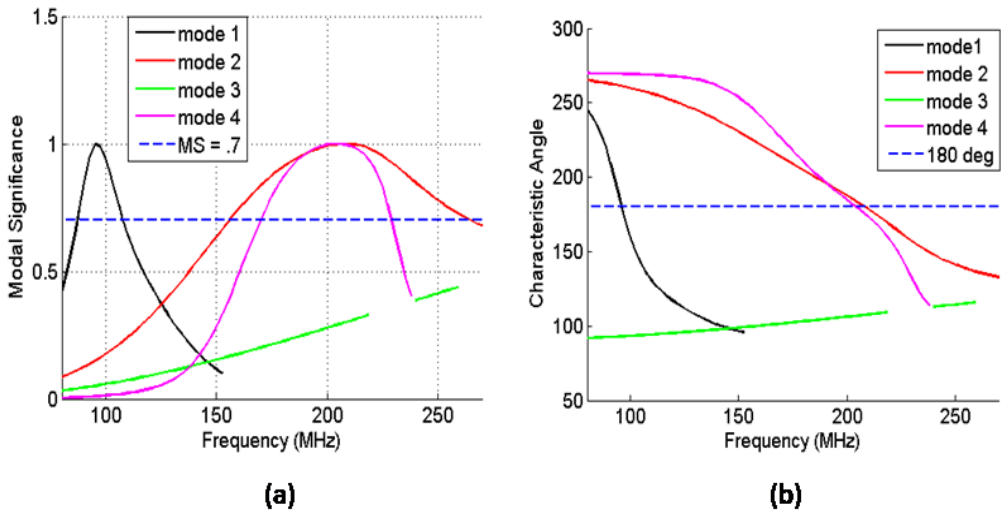

Figure 4.8: (a) Modal significance and (b) Characteristic angle for VHF antenna.

96 GB of RAM, the simulation took approximately 24 hours to complete because of the small mesh size.

Figure 4.8 shows the results of the FEKO simulation with modal significance shown on the left and characteristic angle on the right. Using the modal significance plot and recalling that a mode is considered significant for a value equal to or greater than 0.7, it is evident that there are three significant modes (modes 1, 2, and 4) and one non-resonant mode (mode 3) for the VHF antenna. Another observation that can be made is that mode 2 has a very broad bandwidth of 110 MHz, and mode 4 has roughly half that amount at 60 MHz. One interesting aspect of the modal significance plot is that there are no significant modes between 115 and 150 MHz; yet the S_{11} plot for the antenna in Figure 4.5 (solid blue line) shows the match is good over this frequency band. It would initially seem that there should be another dominant mode over this frequency range.

The concept of modal interaction discussed in Chapter 2, and specifically the equivalent circuit of Figure 2.7 can be used to explain the apparent discrepancy. Consider the characteristic angle plot in Figure 4.8b; modes 1, 2, and 4 are all initially

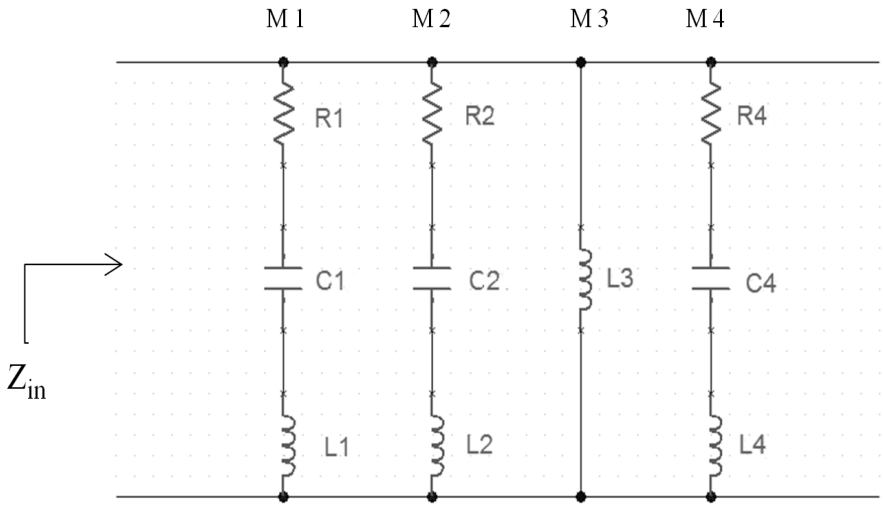

Figure 4.9: Antenna equivalent circuit from CMA perspective.

capacitive, go through resonance, and then become inductive, while mode 3 remains inductive over the entire band of operation. This observation can be used to construct the equivalent circuit model of Figure 4.9 where each mode is modeled as an arm of a parallel RLC circuit. As seen in Figure 4.8b, inductive mode 3 and capacitive mode 4 are essentially equal and opposite over the band in question, acting to cancel each other. Mode 1 dominates below 100 MHz and then goes inductive in a manner that acts to cancel the capacitive nature of mode 2. Thus the interaction of the modes acts to create a matching circuit.

The current distribution on the antenna was also studied with FEKO. Figure 4.10 shows the current distribution at four different points within the frequency band over which S_{11} is below -10 dB. The light and dark blue coloration indicates regions of lower current density. A comparison of the current distribution on the small sheet for the four cases studied shows little variation. The current distribution on the large sheet is characterized by a higher value along the longer edges which then diminishes toward the center. At 96, 142, and 238 MHz, a strong current distribution parallel to the slot is also evident. The color change on the stubs between Figures 4.10a-d shows that they become more active as frequency increases.

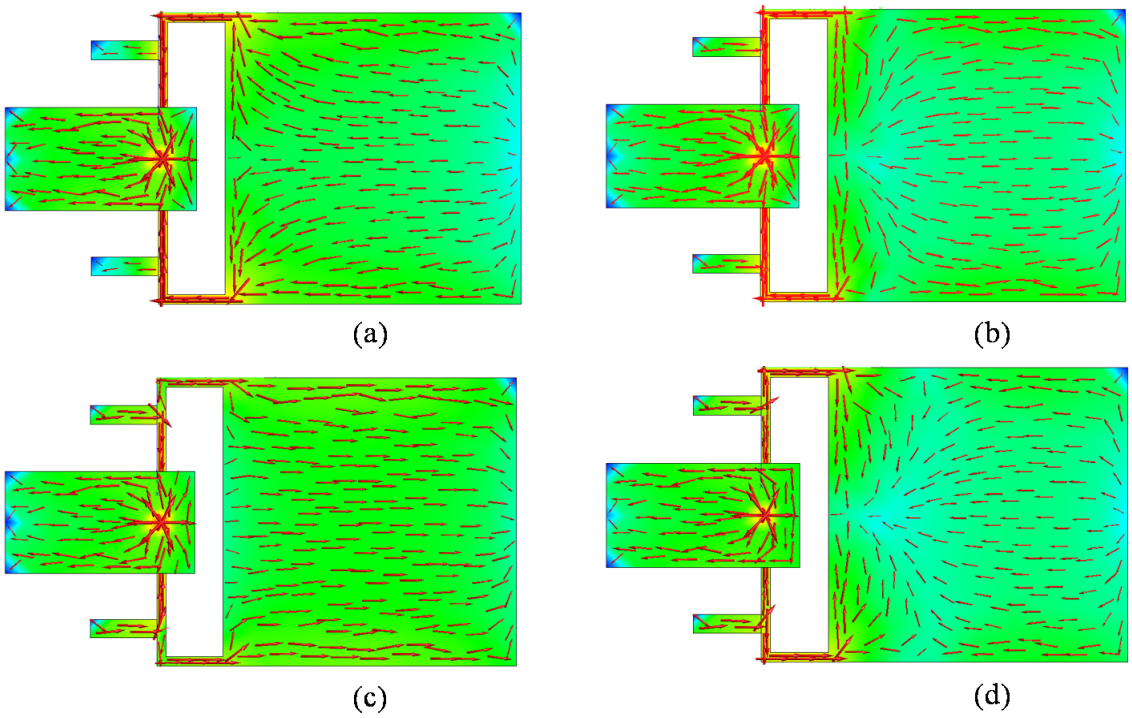

Figure 4.10: Current distribution for (a) 96 MHz (b) 142 MHz (c) 190 MHz (d) 238 MHz.

4.3 Prototype Antenna

A prototype antenna was fabricated using the dimensions detailed in Table 4.1. A 0.91 m (3 ft) wide roll of copper sheeting with a thickness of 127 µm (5 mil) was procured to enable a solid conductive surface for the large rectangular sheet, and both the large and rectangular sheets were precision cut from the roll using a Gerber cutter. Two 3.5 cm thick pieces of foam were cut from a large block to serve as a spacer between the sheets. Foam is commonly used as a core material in composite sandwich structures, and, although aircraft-grade foam is more dense than what was used on the prototype, ε_r for structural foam is on the order of 1.08 and would have minimal impact on antenna performance. An L-shaped piece of polyethylene was attached to the ends of the foam spacers with plastic screws to add mechanical stiffness. Figure 4.11 is a photograph of the prototype antenna with the slotted copper sheet, stubs and feed location visible; the smaller sheet is on the opposite side of the foam substrate.

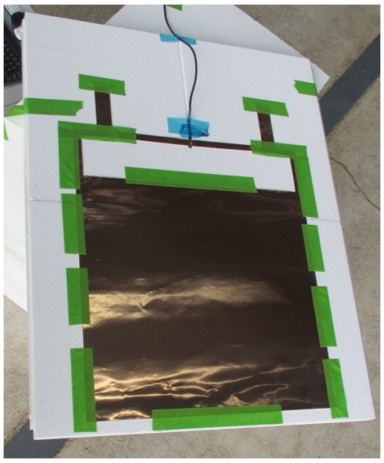

Figure 4.11: Prototype of the VHF antenna.

At the feed point, a section of foam between the sheets was removed, and a PCB containing an RF balun from RF Micro Devices (part no. RFXF9503) was positioned between upper and lower plates. The PCB, shown in Figure 4.12a, has a 50 ohm microstrip at the input (left side of Figure 4.12a), and two traces on the output side to attach wires for connection to the copper sheets. A coaxial cable was soldered directly to the PCB input and the opposite end of the cable was terminated with an SMA connector. The PCB is 3.5 cm wide, and is installed vertically between the two copper sheets to minimize wire lead length. Wires with a diameter of 0.9 mm were soldered to each terminal, and the wires were in turn soldered to the copper sheets at the feed point. A close-up of the balun itself can be seen in Figure 4.12b.

Upon completing assembly of the antenna, an S_{11} measurement was taken. Given the VHF operating range of the antenna, the S_{11} measurement was made in a large aircraft hanger with a ceiling height of approximately 24 m. The antenna was placed on two foam blocks at a height of approximately 1.5 m above the floor and secured in place with masking tape. An Agilent E5071C VNA was placed on a cart and positioned next to the foam blocks with the connection between the VNA cable and antenna feed cable secured to the top of the foam block with tape. A photograph of the measurement setup is shown in Figure 4.13, and a plot comparing the measured

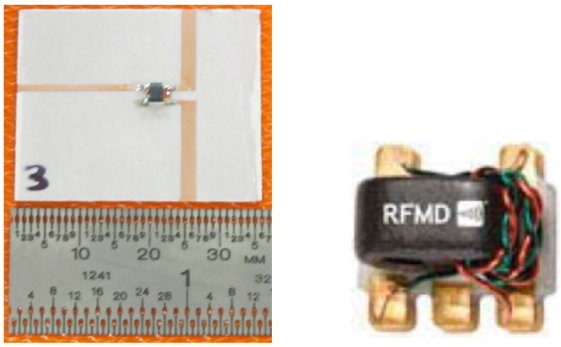

(a) (b)

Figure 4.12: (a) RF balun mounted on PCB (b) Closeup of chip balun [41].

Figure 4.13: Experimental setup for S_{11} measurement.

and simulated data can be seen in Figure 4.14.

As seen in Figure 4.14, there is close agreement between the measured and simulated data. The measured S_{11} was below -10 dB from 93 MHz to 230 MHz, for a bandwidth ratio of 2.47:1. This agrees well with the simulated -10 dB bandwidth of 96 to 241MHz (2.5:1 ratio), as was reported in section 4.1. The main discrepancy is at the upper end of the band. This could be due to a slight difference in the feed between the model and the prototype antenna. A larger diameter wire (5 mm) was

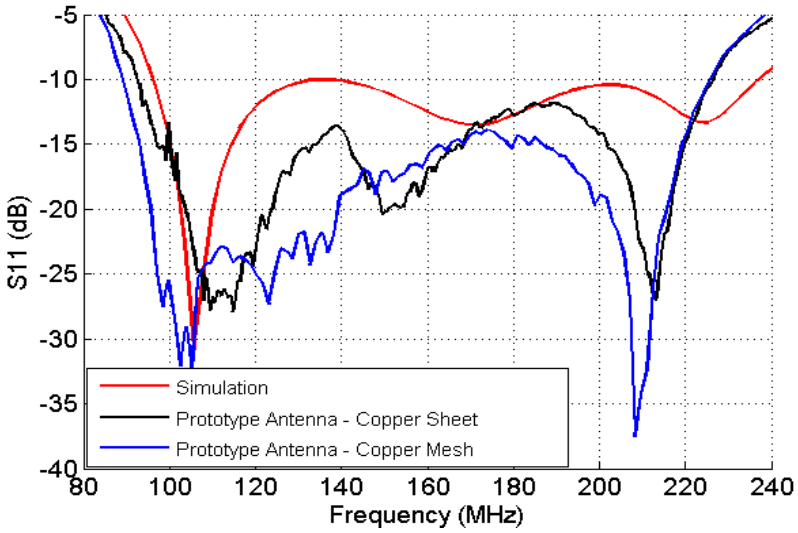

Figure 4.14: Comparison of measured and simulated S_{11}.

used in the simulation than was available when the prototype was constructed, and the smaller 0.9 mm wire and thin PCB trace used to feed the prototype could have caused this reduction in bandwidth.

As a preliminary step toward a more structural version of the antenna, a second prototype was constructed using expanded metal instead of the solid copper sheets. Solid copper cannot be used in structural composite applications because it is difficult to bond to a component, and, even if this were possible, it would represent a parasitic weight increase for the structure. Expanded metal is commonly used on composite aircraft for lightning strike protection, and it is essentially a metallic mesh that is produced by either interweaving small diameter wires or stamping a mesh pattern from a solid conductive sheet. The porous nature of the mesh allows structural epoxy to flow through and bond the mesh to the surface of a composite part during curing. From a mechanical perspective, the mesh is easier to conform to complex shapes and contributes less parasitic weight than a solid sheet. A mesh material from Astroseal Products Mfg. Corp. having grid dimensions of 1 mm by 1.6 mm and a thickness of 130 microns was used for the prototype antenna. Figure 4.15 shows the mesh prototype with the slotted side visible. The nature of the mesh material can be seen

in the close-up on the upper right, which shows the area around the feed. The same PCB that was used on the first prototype was used for the mesh version and is shown on the upper left of Figure 4.15. The S_{11} measurement was repeated, and the results are shown by the blue line in Figure 4.14. It was found that mesh antenna had a slightly higher bandwidth ratio (2.5:1) than the first prototype (2.47:1). This came about because the first prototype was inadvertently fabricated with 5 mm less vertical spacing between the upper and lower traces.

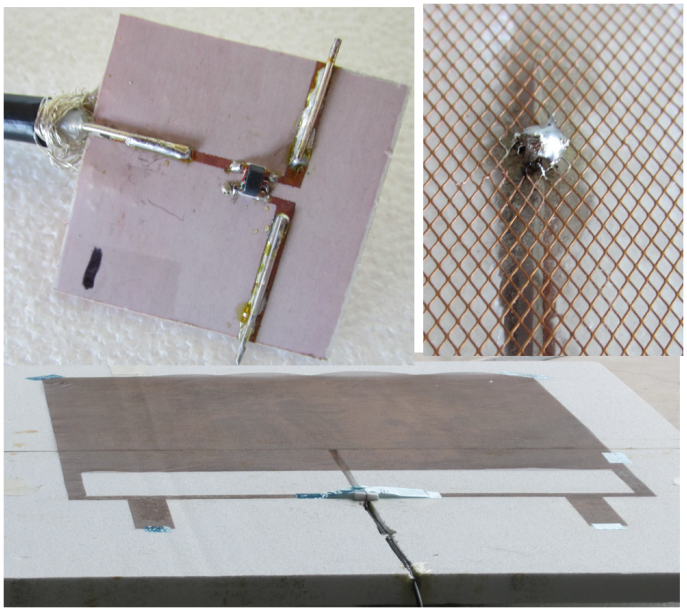

Figure 4.15: VHF prototype with expanded metal.

4.4 Basic Structural Effects

The effects of structural integration were studied through simulations with FEKO. The initial study considered only the dielectric skins on both sides of the airfoil and assumed a foam core would be present. Although it is recognized that some additional support structure would be required, this was not included in the initial simulations. It was also assumed that the airfoil would have a significant through-thickness dimension because only a large airfoil would be able to host the 1.16 m

x 0.62 m antenna. The initial distance between the dielectric layers was taken as 14.5 cm. The dielectric layers themselves were modeled as 1.5 m x 1 m fiberglass composite sheets with a thickness of 5 mm. The structural model is shown in Figure 4.16 with the dielectric skins shown in blue.

The initial integration scheme was to attach the large slotted sheet of the antenna to the inner side of the lower dielectric sheet, as seen in Figure 4.16. A 3.5 cm layer of foam would be placed on top of this assembly, and the small rectangular sheet would be positioned on top of this foam layer. Another 11 cm foam layer would be then added to achieve the desired 14.5 separation distance followed by the upper dielectric sheet. The feed was modeled with 5 mm diameter wire with a voltage source located at the center point. The dielectric properties of the fiberglass panels were taken to be $\varepsilon_r = 4.0$ with tanδ= 0.01, and the foam was modeled as air ($\varepsilon_r = 1$), although, as previously mentioned, some of the more dense foams used in structural composites can be slightly higher with $\varepsilon_r = 1.08$.

The results of the FEKO simulation for the pseudo-structural antenna are shown by the black trace on the S_{11} plot in Figure 4.17. For comparison, the red trace on the same graph shows the baseline simulated S_{11} plot for the antenna in air as presented in Figure 4.14. It is obvious from comparing the S_{11} plots that the presence of the structural material has significantly degraded antenna performance. To examine the variability in dielectric constant and its effect on antenna performance, a second simulation was performed by replacing the fiberglass skins with cyanate-ester/quartz

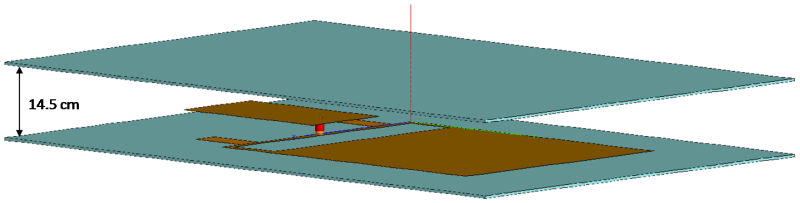

Figure 4.16: Initial FEKO model of antenna and surrounding structure.

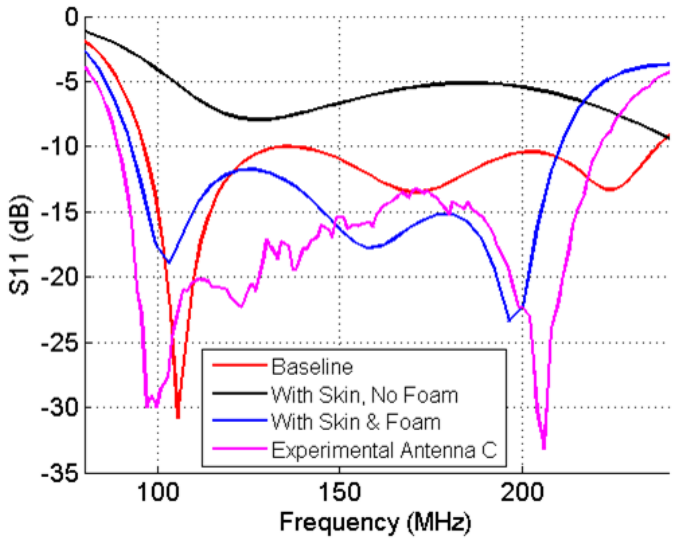

Figure 4.17: S_{11} changes due to structural integration.

($\varepsilon_r = 3.25$, $\tan\delta = 0.006$) to determine the extent to which material properties contributed to the degradation. Interestingly, the results were the same as for fiberglass. This seemed to indicate a problem with the integration scheme itself.

The integration concept was reconsidered, and it was noted that the only major difference between the structural and non-structural antenna was that the lower dielectric sheet was in direct contact with the slotted conductive trace in the structural version. The dielectric sheet was moved downward 5 mm (see Figure 4.16) in the FEKO model to determine if the mere presence of dielectric material near the feed and slot area was affecting the input impedance of the antenna. This 5 mm of separation could be achieved in a composite structure by adding an additional foam layer between the lower sheet and the slotted trace.

As indicated by the blue line on the S_{11} plot of Figure 4.14, a significant portion of the previously observed bandwidth was recovered through the inclusion of the foam buffer. The bandwidth ratio for the structural antenna is 2.26:1 with the reduction occurring at the high end of the operational band. It was also noted that the beginning of the operating band shifted downward slightly from 96 to 93 MHz.

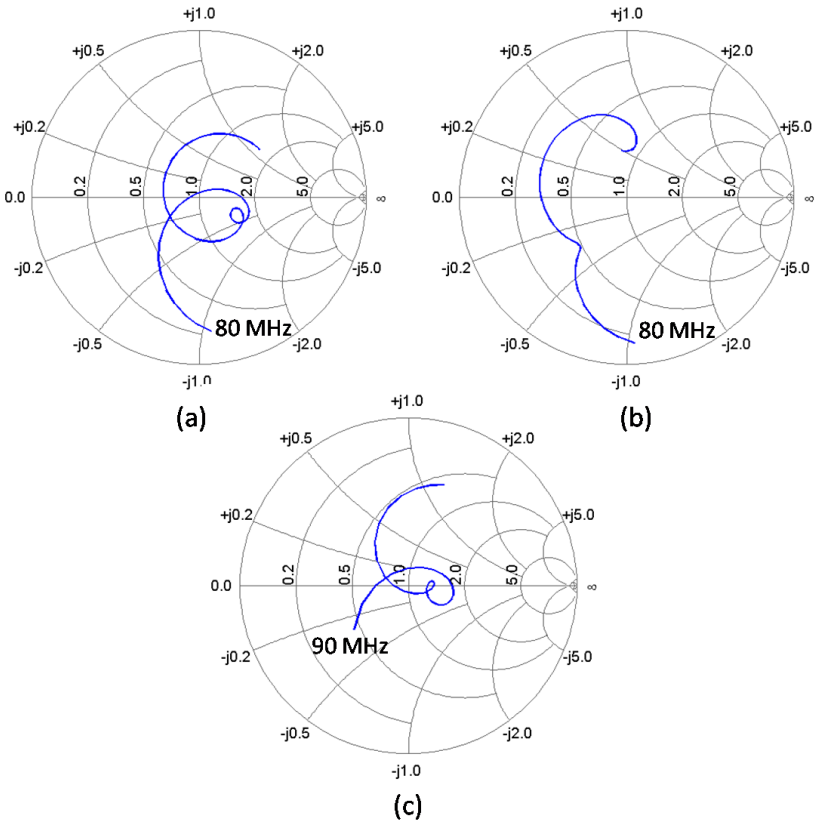

Figure 4.18: Smith charts showing effects of dielectric material.

Figure 4.18 shows the structural interaction discussed above on a Smith chart. Figure 4.18a is the baseline antenna in air, and Figure 4.18b shows the deleterious effect of the dielectric skin being in direct contact with the slotted rectangular sheet of the antenna. The Smith chart of Figure 4.18c shows that the inclusion of the foam buffer results in much improved performance that is similar to that observed for the baseline antenna.

The effect of the foam buffer thickness on S_{11} was investigated through additional simulations, and the resulting data are shown in Figure 4.19. It was determined that a foam thickness greater than 5 mm resulted in slightly more bandwidth, while a thickness under 5 mm resulted in less bandwidth. The buffer thickness was ultimately left at 5 mm because it provided a slightly better match over most of the band and facilitated structural fabrication by making the antenna less intrusive into the

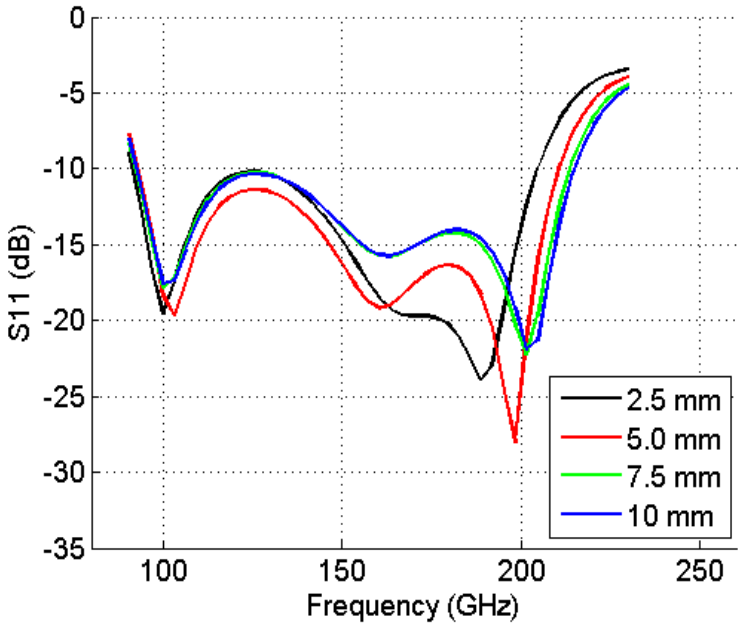

Figure 4.19: Effect of foam buffer thickness on S_{11}

structure.

Simulated radiation pattern plots are shown in Figure 4.20, and Table 4.2 shows the peak gain at discrete points in the operating band for each of the dielectric materials that were studied. From a comparison of Figure 4.20a - c and Figure 4.7a-c, it is evident that the patterns in each of the principal planes at the lower end of the band are similar. Comparing the patterns at the upper end of the band in Figure 4.20d-f to those in Figure 4.7d-f, it is seen that there is close agreement in the ϑ = 90 degree plane, but some variation is found in the other planes. This is because the upper end of the band is 210 MHz in Figure 4.20 whereas it is 240 MHz in Figure 4.7.

Table 4.2: Comparison of simulated peak gain for different composite materials (dBi).

Dielectric	100 MHz	150 MHz	200 MHz
None	2.2	2.7	2.7
Cyanate-Ester / Quartz	2.4	2.7	2.7
Fiberglass	2.3	2.6	2.4

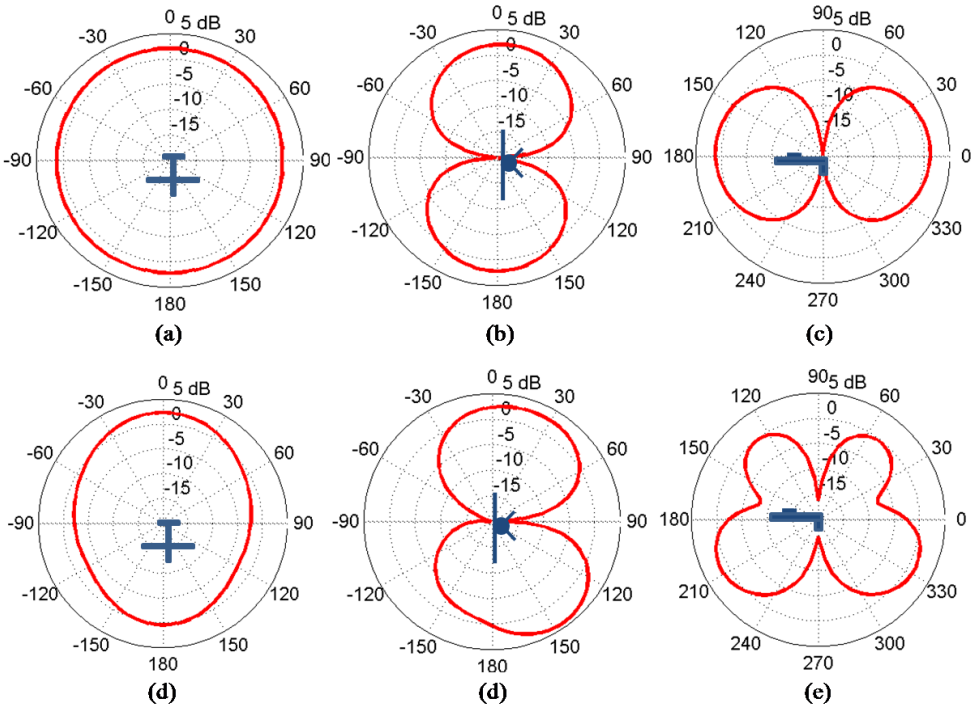

Figure 4.20: Simulated radiation patterns at $\varphi = 0$, $\varphi = 90$, and $\vartheta = 90$ planes respectively, for (a-c) 95 MHz and (d-f) 210 MHz.

4.5 Characteristic Mode Understanding

The CM analysis discussed in section 4.2 was repeated with the dielectric material included in the model. The analysis was conducted in two ways with the first being a single sweep from 80 to 235 MHz, and the second being a segmented approach consisting of three separate simulations over subsets of the operational band. The latter approach was adopted because FEKO indicated that tracking errors occurred during the single sweep analysis.

Figure 4.21 shows the modal significance plot that resulted from the single sweep analysis. In general, the results agree with that seen in Figure 4.8a for the non-structural antenna, but we note two differences. First, the resonant modes have all shifted downward in frequency. Second, mode 2 has much less bandwidth for the structural antenna than the non-structural version. It should be noted that the mesh

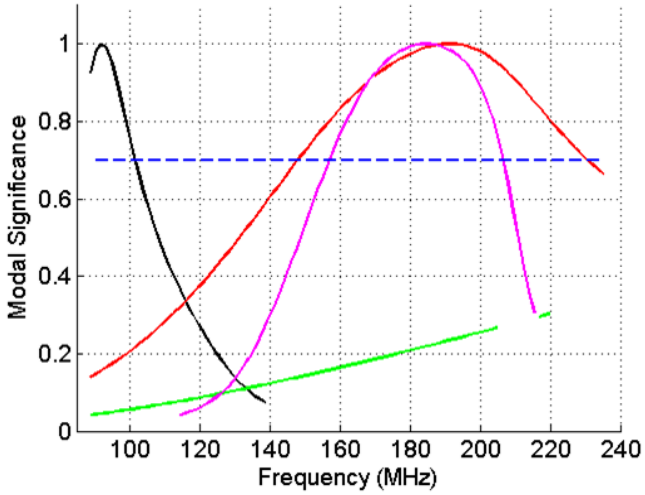

Figure 4.21: Results for single sweep CMA.

size used for the single sweep analysis was $\lambda/32$ at 235 MHz, which is approximately 4 cm.

To address the mode tracking errors, the bandwidth was divided into three segments, 75 to 130 MHz, 129 to 179.5 MHz, and 179.5 to 230 MHz, and a modal analysis was conducted separately for each segment. Care was taken to maintain the same frequency increment of 2.29 MHz for each analysis segment to aid in merging the data from all segments. It was speculated that this segmented approach would enable a finer mesh to be used, if needed, to eliminate the mode tracking errors. The initial mesh selected was a triangle edge length of 3.5 cm, which is $\lambda/37$ at 230 MHz

Upon completion of the 75 to 130 MHz segment, FEKO indicated that two mode tracking errors had occurred. The data for the first segment was saved in a spreadsheet, including the two error modes, and the model was re-meshed with a triangle edge length of 2.2 cm for the 129 to 279.5 MHz segment. As a result of the finer mesh, the problem size grew large enough that FEKO ran out of memory despite having 96 GB of RAM available. The mesh size was then increased to a 3 cm edge length, and the analysis was restarted. Although the analysis completed for the new mesh size, FEKO again indicated that four mode tracking errors had occurred. All

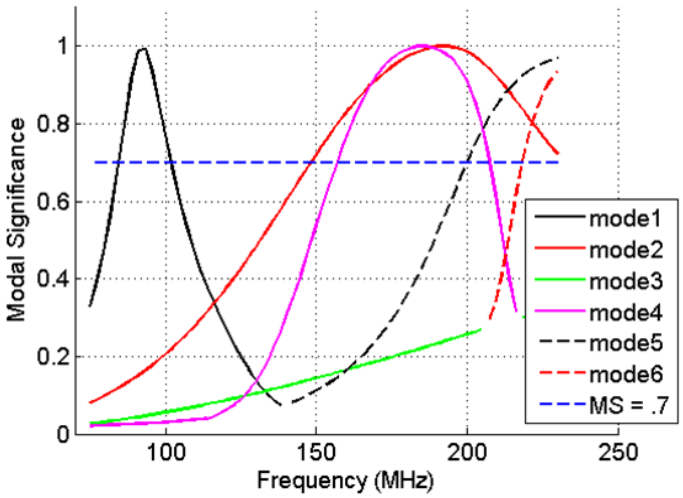

Figure 4.22: Results for segmented CM analysis.

data for the second segment was saved to the spreadsheet, and the last segment was analyzed using the 3 cm mesh size.

Several problems were encountered with the segmented approach. One issue is that the FEKO mode labels were inconsistent between segments; for example, modes 1 and 2 were interchanged between the first and second segment, as were modes 3 and 4. Another problem was the time required to complete an analysis using the 3 cm mesh size, which, for segment two, was over 66 hours. Finally, manual inspection of the data from all segments revealed that some of the mode tracking errors were caused by FEKO starting a new data set for a previously detected mode. Ultimately, this manual inspection process enabled the modes to be pieced together, and two of the so-called errors were actually higher order modes. Figure 4.22 shows the resulting modal significance plot for the segmented analysis, and Table 4.3 lists some of the details such as mesh size and run time recorded during the analysis process.

Tables 4.4 and 4.5 summarize the effect of the dielectric structural materials on the resonant frequency and bandwidth of each mode, respectively. Consistent with what was observed in the case of dielectric loading in Chapter 2, structural materials caused the resonant frequency of each mode to decrease. Mode 1 saw the smallest

downward shift at 2.8 MHz, followed by mode 2 with a 17 MHz reduction, and the resonant frequency of mode 4 decreased by 20 MHz. The structural dielectric material also caused a reduction in modal bandwidth with modes 1 and 4 being reduced by 14.5% and mode 2 decreased by 24.3%.

Upon completing the analysis of structural integration effects, a structural antenna was constructed and is shown if Figure 4.23. The fiberglass sheets used for this antenna were 2 mm thick instead of the 5 mm thick fiberglass and cyanate-ester quartz sheets used in the simulations. The thinner sheets were already on-hand, and this change saved the cost of purchasing commercial composite sheets or the supplies

Table 4.3: Metrics observed during segmented analysis.

Frequency Range (MHz)	Edge Length (cm)	Triangle Count	Modes / Track Errors	Run Time (hours)
75 - 130	3.5	15,567	4/2	34.6
129 - 179.5	2.2	-	-	Error
129 - 179.5	3.0	20,897	4/4	66.2
179.5 - 230	3.0	20,897	4/2	57.8

Table 4.4: Effect of structural material on modal resonance.

Mode	F_r No Dielectric (MHz)	F_r Dielectric (MHz)
1	94.9	92.1
2	208	191
4	204	184

Table 4.5: Effect of structural material on modal bandwidth.

Mode	Bandwidth No Dielectric (MHz)	Bandwidth Dielectric (MHz)
1	21.4	18.3
2	106.7	80.8
4	59.5	50.8

needed to manufacture custom composite panels, not to mention the labor cost and time associated with manufacturing. The expected impact of the thinner material was that measured performance would be slightly better than for the thicker dielectric used in simulations. The measured S_{11} versus frequency for this antenna are shown in Figure 4.17 using the magenta line. As seen, the operating bandwidth within -10 dB S_{11} is from 89 to 221 MHz. As expected, the measured performance of the structural antenna was better than the simulation results (2.48:1 bandwidth ratio vs. 2.26:1), but it is evident by comparison with Figure 4.14 that the structural antenna has less bandwidth than the first two prototype antennas - which agrees with what was observed in simulations.

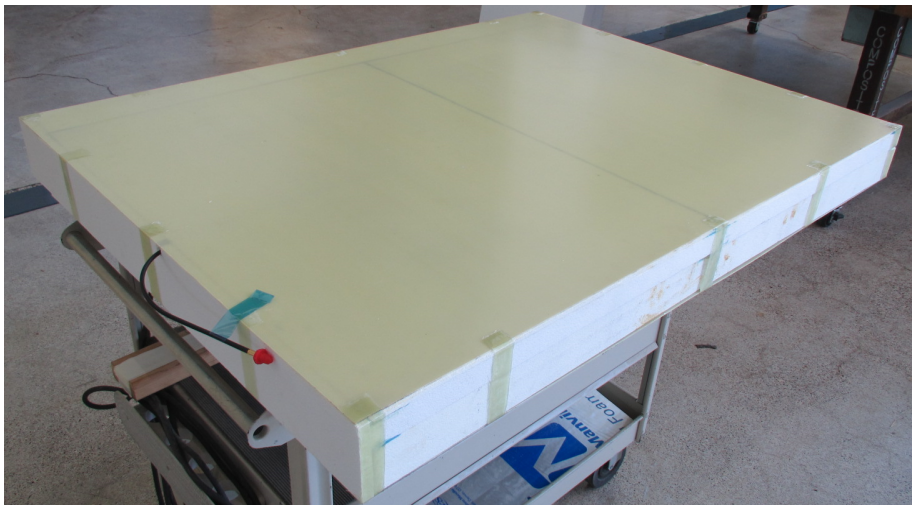

Figure 4.23: Prototype of the structural VHF antenna.

4.6 MIMO Application

A common vehicle configuration for UAVs is the inverted V tail, in which the conventional horizontal and vertical stabilizers are replaced by two airfoils that are oriented downward at an angle from the horizontal. Such a structure could be used to implement a structural VHF antenna to enable an airborne multiple input, multiple output (MIMO) capability. MIMO has been suggested as a means of increasing throughput

for communications links [42, 43, 44] and improving radar performance [45].

To investigate the feasibility of this concept, two vertically oriented structural antennas were used to approximate an aircraft having two parallel tails. Because independent antennas are required for MIMO applications, the envelope correlation coefficient (ECC) was used to characterize the relative independence of the antennas. The ECC study was conducted by first using FEKO to calculate the S-parameters with the antennas being separated by distances of 1m, 1.25m, and 1.5m. The resulting data was post-processed using MATLAB to calculate ECC for each case. Simulations indicated that the efficiency of the antenna is on the order of 98%, so accurate results for ECC can be expected through the use of S parameters as given by Equation 4.1 [46].

$$\boldsymbol{ECC} = \frac{|\boldsymbol{S_{11}^* S_{12} + S_{21}^* S_{22}}|}{(\boldsymbol{1 - |S_{11}|^2 + |S_{21}|^2})(\boldsymbol{1 - |S_{21}|^2 + |S_{12}|^2})} \tag{4.1}$$

Figure 4.24 shows plots of ECC versus frequency for each separation distance over the band of interest. The data indicate that not only is ECC low for all separation distances, the case of 1 m separation results in the lowest overall ECC across the band. This result is encouraging because a 1 m separation distance is a reasonable value for tail separation on a twin tail UAV.

Given the encouraging ECC results obtained with the parallel tail configuration, another study was conducted with the antennas canted at a 52 degree angle from the horizontal to represent antennas being integrated with inverted V tails. Figure 4.25 shows the FEKO model used for the study. The model is intended to represent the aft section of a small UAV through the inclusion of a fuselage section. The fuselage is modeled as a half cylinder with a radius of 69 cm and length of 110 cm. It was assumed that the fuselage is a cyanate-ester quartz composite with a thickness of 5 mm. The forward and aft sides of the fuselage are closed out with a 5 mm

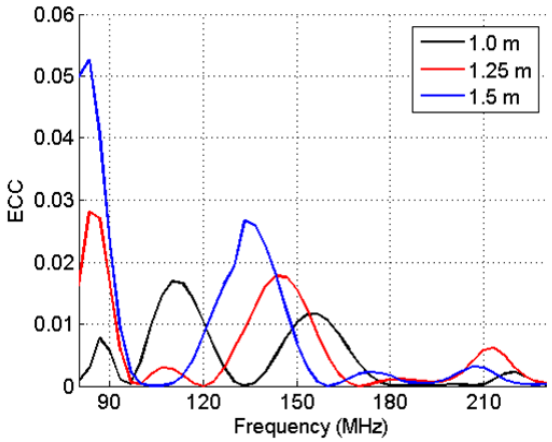

Figure 4.24: ECC for vertical tails separated horizontally by 1.0, 1.25, and 1.5 m.

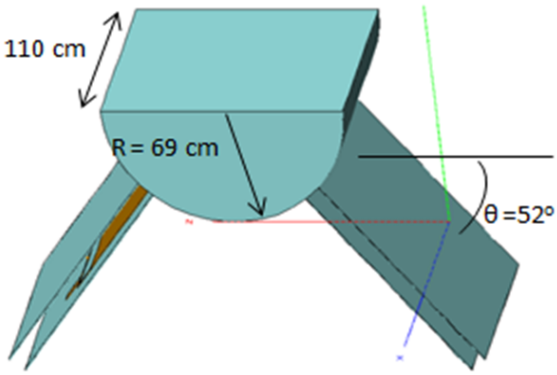

Figure 4.25: FEKO model of an inverted V tail UAV.

thick composite panel representing a bulkhead, although we note that the aft panel would be partially open to accommodate a propeller shaft. The tails themselves are represented as the structural VHF antenna of Figure 4.23 and have the same dimensions with the exception that the spacing between the dielectric sheets was reduced to 10 cm.

The previously described process was used to calculate ECC based on Equation 4.1 for the inverted V tail model, and the results are shown in Figure 4.26. A comparison between this result and the ECC plots of Figure 4.24 shows that the inverted V tail configuration achieves a lower ECC than was realized with any of the parallel tail

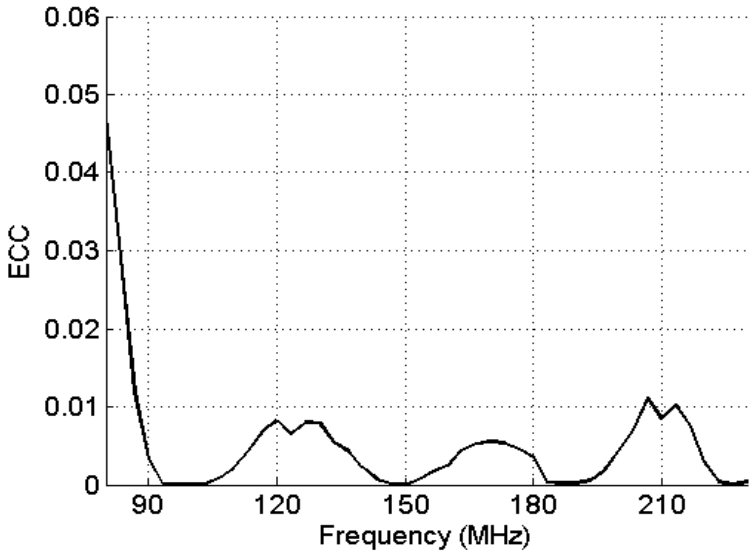

Figure 4.26: ECC for the inverted V tail model.

configurations previously studied.

Simulated radiation patterns for the inverted V tail concept are shown in Figure 4.27. Two rounds of simulations were conducted. In the first case, the antenna on the left side was excited and the antenna on the right was terminated with a 50 Ω load. In the second case, the excitation and load were switched to the opposite sides. The patterns for each case were found to be nearly identical except for the orientation in the roll plane being canted at +/- 52 degrees as would be expected from the physical orientation of the antenna structure. The patterns depicted in Figure 4.27 are for the first case with the left side antenna excited. The plots at the low end of the band in Figure 4.27a-c show good symmetry with slightly more gain in the forward direction than aft (Figure 4.27a). At the upper end of the band in Figure 4.27d-f, the patterns become more directional with energy being directed forward and outboard. While the null directed to the aft at the upper end of the frequency band could be undesirable in some applications, the independent patterns combined with low ECC value across the band indicate the use of tail-integrated antennas for MIMO is feasible.

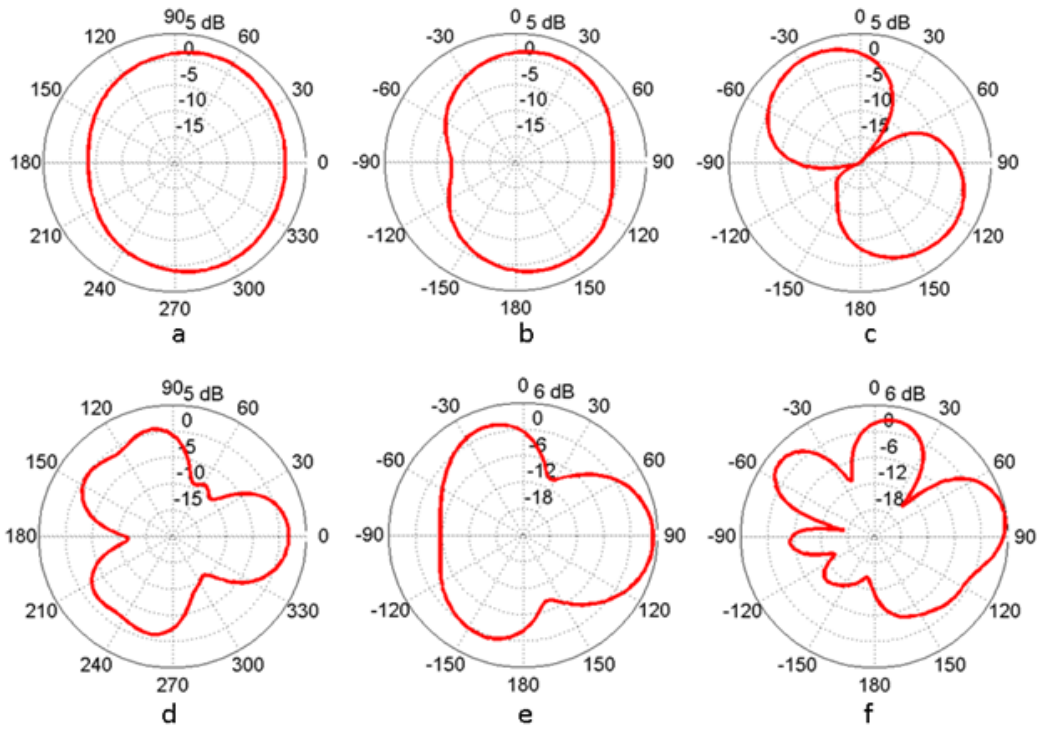

Figure 4.27: Simulated patterns for aircraft azimuth, pitch, and roll planes for (a-c) 95 MHz and (d-f) 208 MHz.

Chapter 5

Structural High Impedance Surface

Satellite communications (Iridium, Globalstar, Inmarsat, MUOS) and navigation systems (GPS, GLONASS) need Circularly Polarized (CP) antennas [47]. While microstrip patch antennas or cross-fed dipoles can provide CP radiation if properly excited such antennas are very narrowband. For broadband applications equiangular spiral or Archimedian spiral antennas are preferred [48]. For airborne applications, the antenna is almost always required to operate against a metallic reflector or ground plane. While this allows a unidirectional beam it presents a challenge in terms of obtainable bandwidth both in terms of impedance and gain. Since the reflector needs to be placed about a quarter wavelength from the antenna at the lowest frequency of operation at the UHF frequencies this becomes prohibitively thick for the aircraft structure. For example, at 450 MHz the required separation could easily exceed 15 cm (6 inches). Although absorbing material loading have been proposed and considered they lead to significant reduction in efficiency and hence gain. In addition, these solutions all contribute parasitic weight to the aircraft in terms of either an externally mounted assembly or structural enhancements and absorbing material needed for a conformal installation. While this approach is used on large commercial and military aircraft, it is not a viable option for smaller UAVs with limited payload capacity.

In recent years focus has been placed on reducing the spacing between a spiral antenna and the metal reflector with the help of High Impedance Surfaces (also referred to as Electromagnetic Bandgap or EBG structures) [49, 50]. Bell et al. presented findings from EM simulation studies of an Archimedian spiral over a mushroom EBG

was presented for X-band [49]. Nakano presented a more comprehensive work on a pseudo-mushroom EBG and an equiangular spiral where axial ratio, pattern, and gain were investigated and optimized. The focus of this chapter is to investigate and design a low profile spiral antenna for aircraft structural integration with the help of EBG structures. To that end, non-via progressive EBG structures are considered. A broad frequency range of almost an octave (425-800 MHz), right hand circular polarization with axial ratio less than 3 dB, and gain greater than 3 dBi are targeted while restricting the total antenna plus EBG height to no greater than 7.5 cm (3 inches). Furthermore, material weight reduction is considered by leveraging the volume inside a composite sandwich structure which consists of foam or other materials having a low dielectric constant.

We begin with an illustration of how structural components can impact the performance of a conformal spiral antenna before going into the development of the structural concept that allows an EBG-backed spiral to be integrated with a composite structure. The chapter then concludes by showing that the developed structure successfully mitigates the problems that come about from radiated fields interacting with conductive structural subcomponents.

5.1 Conformal Antenna on Composite Structure

Although we eventually desire an antenna structure that provides good performance from 425 to 800 MHz, we begin with the analysis of how structural features can impact antenna performance by considering the case of a spiral antenna attached to a UAV fuselage in a conformal manner and operating from 200 to 700 MHz. The desire is for low frequency operation, so the results of the study are assessed primarily in the 200 to 400 MHz range.

Given that equiangular spiral antennas are well known in the literature and in industry, a commercial software package known as Antenna Magus was used to layout

the physical geometry of the antenna. The primary input to the design software was the operating frequency range and the dielectric properties of the material, which were taken as $\varepsilon_r = 3.25$ and $\tan\delta = 0.006$ to represent a cyanate-ester/quartz composite skin. It should also be noted that the lower end of the frequency range has implications for the size of the structure to be used in the study. The outside diameter of the antenna determines the lowest frequency of operation, with this dimension being a half wavelength [51]. Thus, in order to support operation at 200 MHz, the structure must provide enough surface area to host a spiral with an outside diameter of 0.75 m.

The resulting two-arm spiral design consists of two complete rotations of copper having a through-thickness of 127 µm and tapering from a width of 1 cm at the center to 8.3 cm at the widest point of the arms. The magnitude of the input impedance averages 216 ohms across the band, which is slightly higher than the theoretical value of 188.5 Ω [48].

A monocoque aircraft structure was considered for this work. This type of structure is characterized by the use of formers and bulkheads to give the fuselage its shape, and the skin carries the primary stresses due to a lack of bracing members such as longerons and stringers [52]. Figure 5.1 shows a representative fuselage section that was used in the analysis. It has an overall length of 2 m and a simple half cylinder cross section having a radius of 0.4 m. The fuselage skin was assumed to be cyanate-ester/quartz composite with a thickness of 3 mm. The spiral antenna was centered on the top surface of the fuselage and was placed on the inner side of the fuselage skin. Attachment of the spiral arms to the composite surface through bonding or additive manufacturing techniques results in a very lightweight installation; however, the electrical properties of the composite will have an impact on antenna performance. Bore-sight gain has been shown to decrease as the dielectric constant and/or the thickness of the substrate is increased [53].

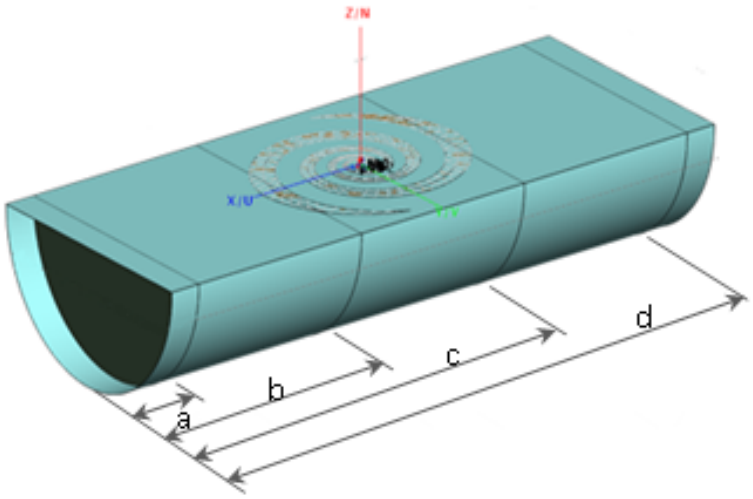

Figure 5.1: Monoqocue fuselage section with conformal spiral antenna.

Several structural configurations were considered that incorporated up to four bulkheads located at various distances from the front of the fuselage section, as indicated by the dimensions a through d in Figure 5.1. The bulkheads were considered to be made from carbon fiber re-enforced polymer (CFRP) panels with a thickness of 3 mm and a conductivity of 1000 S/m. Table 5.1 summarizes the various bulkhead configurations that were investigated. Structure 1 has no bulkheads and is used only for comparison because it is not a practical mechanical structure. Structures 2 and 3 have two and four bulkheads, respectively; however, no bulkheads are located directly below the antenna. Structure 4 has four bulkheads with two of these located under the outermost arms of the antenna.

Table 5.1: Bulkhead positions relative to forward edge of fuselage section (m).

Parameter	a	b	c	d
Structure 1	n/a	n/a	n/a	n/a
Structure 2	0.4	n/a	n/a	0.4
Structure 3	0.1	0.5	1.5	1.9
Structure 4	0.1	0.7	1.3	1.9

Simulations were conducted using FEKO. Figure 5.2 shows the simulated S_{11} for

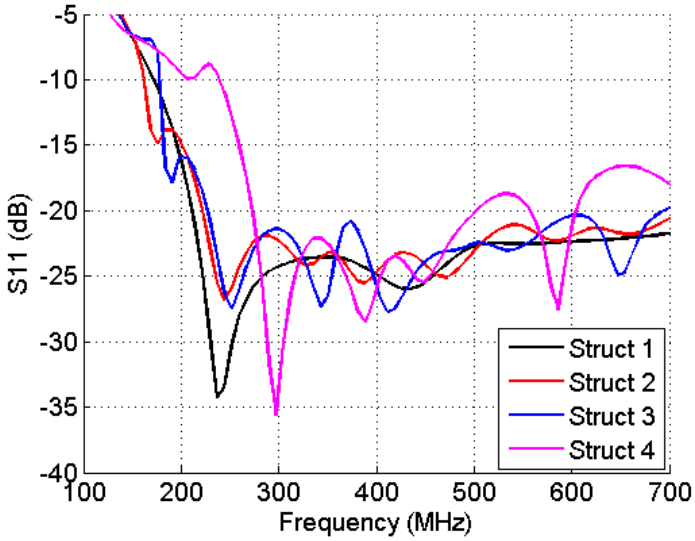

Figure 5.2: Simulated S_{11} for the various bulkhead configurations of Table 1.

all of the configurations listed in Table 1. Structure 4 is clearly the worst configuration for achieving operation down to 200 MHz, while structures 2 and 3 have a response similar to the no bulkhead configuration, albeit slightly more oscillatory in nature.

Simulated RHCP gain data for the antenna in the $\varphi = 0$ plane is shown in Figure 5.3. Structures 2 and 3 provide the best gain from 200 to 400 MHz. The gain for structure 2 is near 3 dB at the lower end of the band while structure 3 has higher gain at the high end of the band. Interestingly, structure 1 offers the lowest overall gain while structure 4 outperforms all others within 450-580 MHz. These results clearly illustrate that antenna performance is influenced by the structural configuration.

Figure 5.4 shows the simulated axial ratio results for each of the four structures investigated. It is evident that the presence of the bulkheads has a detrimental effect in terms of axial ratio over the range of 200 to 400 MHz. Structures 2 and 3 appear to provide better axial ratio than structure 4. Nevertheless, even for the two best cases (structures 2 and 3), the axial ratio exceeds 3 dB at frequencies below 285 MHz. Comparing both gain and axial ratio structure 3 is a good compromise. It provides less than 3 dB axial ratio above 285 MHz and also has 2 to 4 dB RHCP gain above

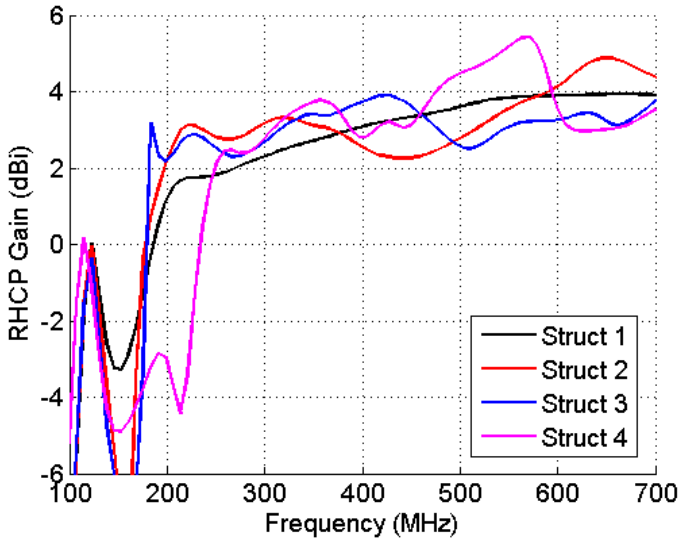

Figure 5.3: Simulated gain vs. frequency for the structures of Table 5.1.

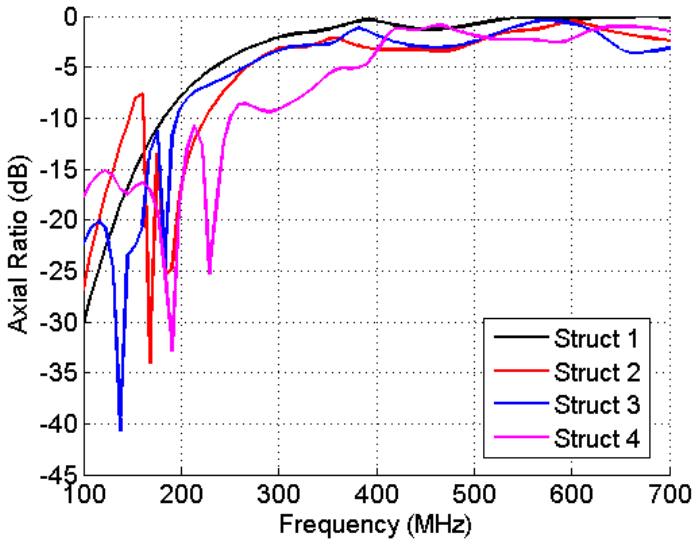

Figure 5.4: Simulated axial ratio for the structures of Table 5.1.

that frequency.

5.2 Reflector for Isolation and Directional Performance

One approach to mitigating the effects of structural interaction would be to place a reflector between the antenna and underlying structure. The simple approach

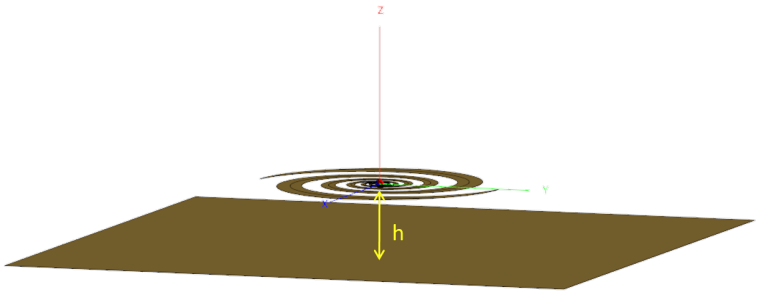

Figure 5.5: Spiral antenna backed by a reflector.

of placing a metallic reflector behind the spiral is an attractive solution because it provides the desired directional radiation pattern and the planar layout lends itself to integration with a composite sandwich structure. The concept is illustrated in Figure 5.5, with the primary factor being the spacing required between the spiral and the ground plane to bring about the desired RF performance.

The feasibility of this concept was investigated with FEKO by simulating the physical layout for three different reflector - antenna separation distances (designated as h in Figure 5.5). The initial distances selected for study were 17.6 cm, 12.2 cm, and 9.4 cm, which correspond to a quarter wavelength at 425 MHz, 612 MHz, and 800 MHz, respectively. The reflector was assumed to be a square with sides 1.5 m in length and centered under the origin of the spiral. It should also be noted that the antenna used in this study was smaller and more tightly wound than the antenna used in the previous section. Figure 5.6 shows the antenna which has 3.25 turns, an outside diameter of 64.4 cm, and an inner diameter of 3.9 cm. The simulated S_{11} with reference to 120 Ω is shown on the right of the figure.

The simulated S_{11} for each separation distance is plotted with reference to 180 Ω in Figure 5.7 while the peak gain is plotted in Figure 5.8. The 9 cm separation distance was the only case in which S_{11} rose above -10 dB over a portion of the desired frequency band. In terms of gain, a separation distance of 17 cm was found to result in a gain roll-off beginning around 700 MHz and falling below 3 dB at 765 MHz.

Figure 5.9 shows the simulated axial ratio for each of the separation distances. Of

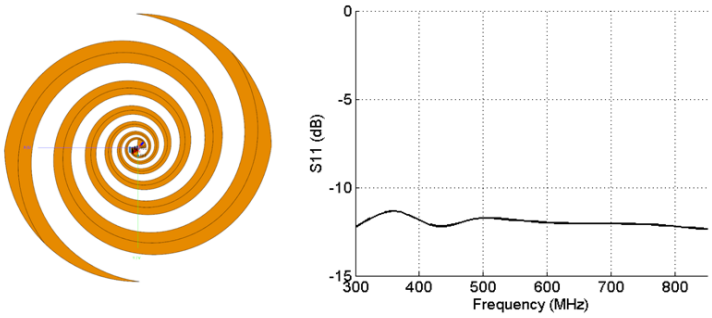

Figure 5.6: Spiral antenna and simulated S_{11}.

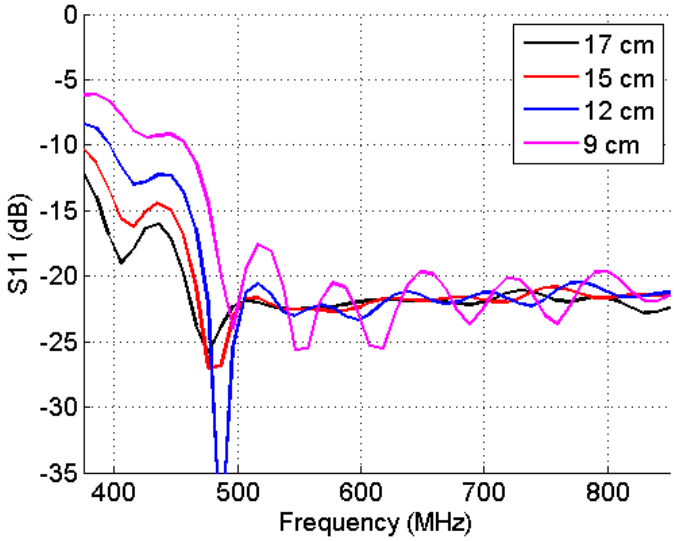

Figure 5.7: Simulated S_{11} for various distances between spiral and reflector.

the three initial distances considered, only the 17 cm was better than 3 dB across the desired frequency range. It was also noted that the a separation of 12 cm resulted in axial ratio better than 4 dB across the desired frequency range. Given these results, a fourth simulation was conducted for a separation distance of 15 cm.

As seen by the magenta trace in the preceding plots of S_{11}, gain, and axial ratio, a separation distance of 15 cm meets all of the desired performance objectives. However, from a structural integration perspective, 15 cm (nearly 6") is too large to be practical for a sandwich structure core thickness on a small UAV. Hence, a means of reducing the distance between the reflector and spiral is needed. Note that the 15 to 17 cm

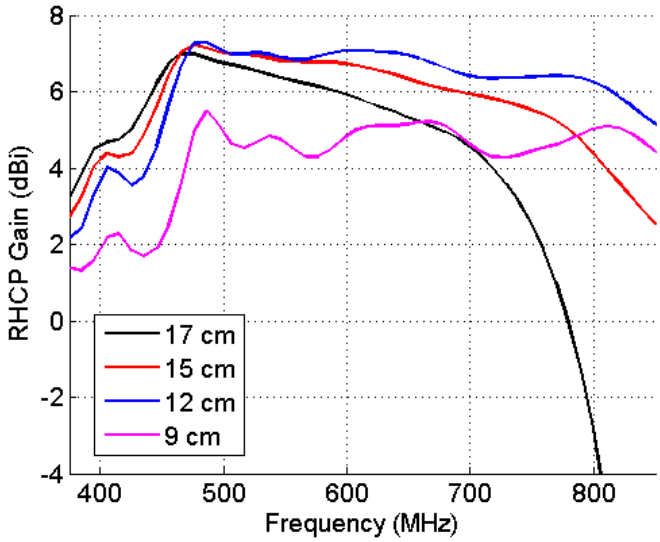

Figure 5.8: Simulated gain for various distances between spiral and reflector.

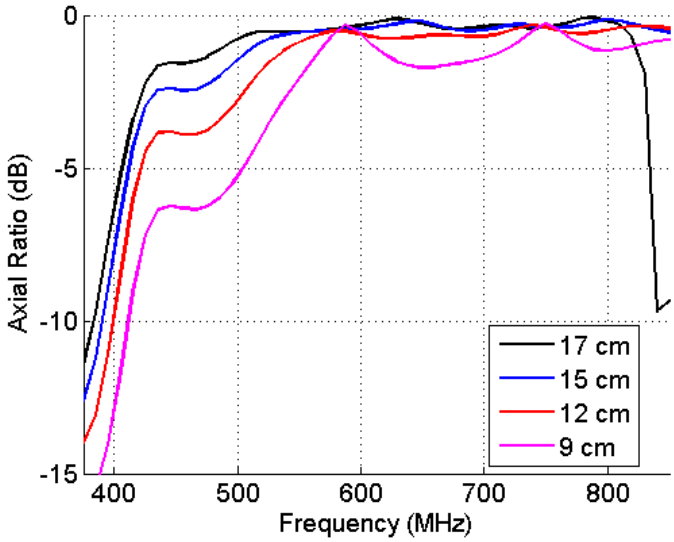

Figure 5.9: Simulated axial ratio for various distances between spiral and reflector.

separation is about one quarter of the wavelength at the lowest frequency of operation e.g. 425 MHz. One structure that demonstrates significant promise in order to reduce antenna to reflector separation is the electromagnetic bandgap structure.

Electromagnetic bandgap (EBG) structures were originally proposed by Sievenpiper [54] and have been investigated in such situations [55] as well as for isolation

improvement between antennas [56, 57] and gain enhancement for antennas [58, 59]. An EBG is a periodic arrangement of conductive patches, with or without vias connecting the patches to an underlying ground plane, that acts to suppress surface waves and can also reflect incident waves without a phase change [60].

5.3 Square EBG

In order to be used for aircraft structural applications, a mechanically robust EBG structure needs to be developed. As was stated previously, composite sandwich structures consisting of two composite laminates separated by a core material that is often a dielectric are common in aircraft construction. They are a logical choice for implementing a load-bearing EBG because they provide good mechanical stiffness from a structural perspective and the three-dimensional geometry combined with the ability to layer the core material aligns well with the layout of EBGs.

The development of an EBG for a broadband dipole has been previously investigated [61, 62], and an EBG design described by Chamok et al. [62] was adapted to serve as a starting point for the structural EBG. The original design consisted of an 8 by 8 array of 50 mm by 50 mm metallic patches, with each patch connected to an underlying ground plane by a 25 mm via. The EBG structure was initially studied on an FR4 substrate and subsequently implemented on Plexiglass. The gap between each patch was 5 mm; yielding a period for each unit cell of 55 mm. Using the governing equations for a mushroom EBG in Equations (5.1) to (5.3) [61, 62], where the symbols have their usual meanings, the resonant frequency of this structure was determined to be 576 MHz; which is close to the midpoint of the desired 425 MHz to 800 MHz operating band. To accommodate the spiral antenna, the patch array was expanded to 18 by 18 patches as shown in Figure 5.10, which is the FEKO model used to simulate the initial layout. The antenna was positioned 2.5 mm above the surface of the EBG.

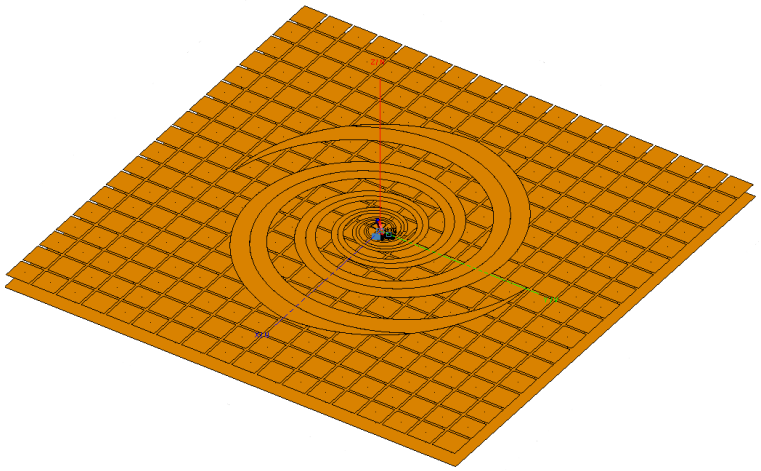

Figure 5.10: 18 x 18 EBG under spiral antenna.

$$L = \mu_0 h \tag{5.1}$$

$$C = \frac{w\epsilon_0(1+\epsilon_r)}{\pi} \cosh^{-1}\left(\frac{w+g}{g}\right) \tag{5.2}$$

$$f_0 = \frac{1}{2\pi\sqrt{LC}} \tag{5.3}$$

As indicated by the black line in the simulation results of Figures 5.11 to 5.13, the initial geometry did not produce the desired effects, the S_{11}, gain, and axial ratio were all poor across the desired frequency band. This was attributed to a thick layer of dielectric material that was present in the design by Chamok et al. [62], but not included in the initial FEKO model of the modified EBG. The via length was subsequently increased to 4 cm and the simulation was repeated with the results indicated by the red line in Figures 5.11 to 5.13. As seen, the performance above 600 MHz has improved, but all parameters remain poor at the lower end of the frequency band. The EBG was resized for a much lower frequency (350 MHz) by increasing the patch size to 10 cm and the gap to 1 cm which reduced the patch array to 9 by 9. The antenna height above the EBG was increased to 1 cm. The simulated S_{11} and gain,

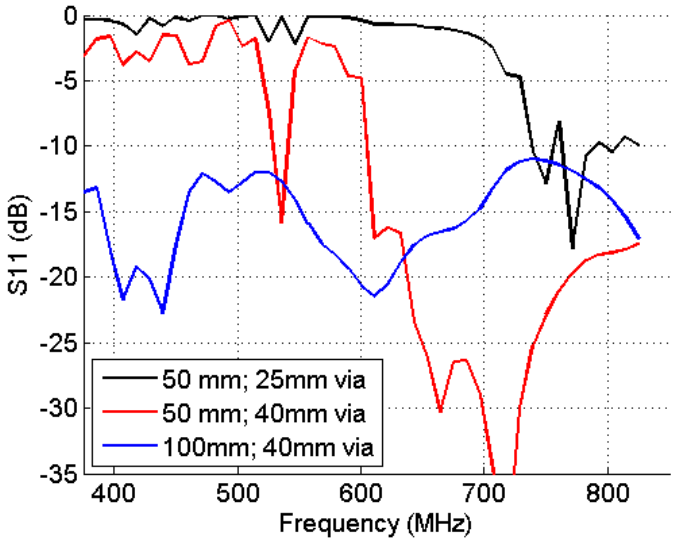

Figure 5.11: Simulated S_{11} for EBG-backed spiral antenna with no dielectric material in the model and EBG unit cells consisting of 50 mm patch and 5 mm gap and 100 mm patch and 10 mm gap.

shown by the blue line in Figure 5.11 and 5.12, now meet the desired performance characteristics across the entire frequency band. The axial ratio indicated by the blue trace in Figure 5.13 is much more stable; however, it varies between -8 dB and - 3 dB and thus remains outside the acceptable range over the entire frequency band of interest. This phenomenon was previously reported by Nakano [50], and the axial ratio only improved in that work when the EBG was removed from the area under the antenna.

5.4 Circular Metasurface

The increasing via length and poor results for axial ratio led to a reconsideration of the EBG concept. It was decided to investigate a circular EBG structure and evaluate the feasibility of eliminating the vias to simplify manufacturing and avoid potential electromagnetic issues (discussed later) that could arise from imprecise positioning of the vias.

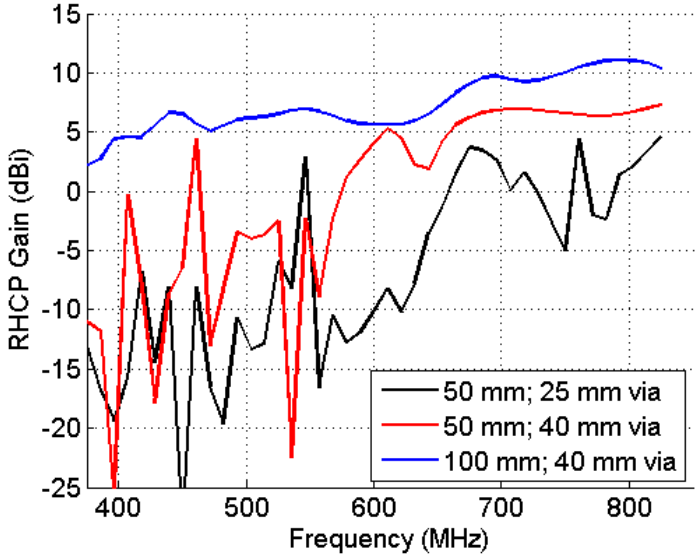

Figure 5.12: Simulated gain for EBG-backed spiral antenna with no dielectric material in the model and EBG unit cells consisting of 50 mm patch and 5 mm gap and 100 mm patch and 10 mm gap.

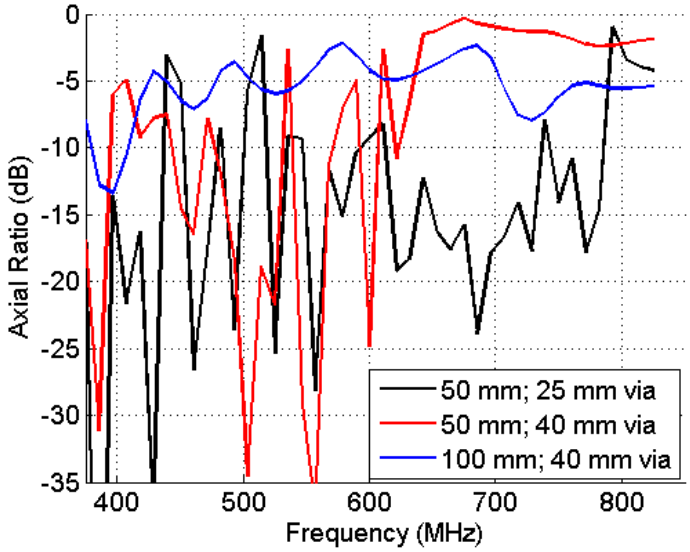

Figure 5.13: Simulated axial ratio for EBG-backed spiral antenna with no dielectric material in the model and EBG unit cells consisting of 50 mm patch and 5 mm gap and 100 mm patch and 10 mm gap.

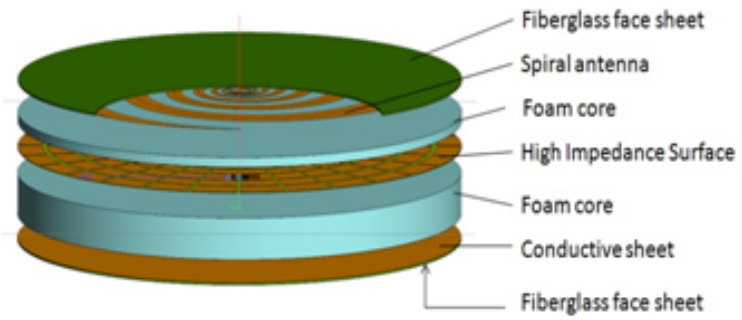

Figure 5.14: Concept for structural integration of EBG and spiral antenna.

Several factors were considered in the conceptual design for a structural EBG. First, a structural integration scheme was developed that was driven by the following key choices and observations:

1. The limit on total thickness was set at half the 15 cm distance between the reflector and antenna as shown in Figure 5.5.

2. Further study of the mushroom EBG showed that axial ratio improves with both via length and antenna height above the EBG.

3. For better power handling capability, the use of a Dyson balun [63] was preferred over a chip balun.

Figure 5.14 shows the initial integration scheme. The structure which consists of a 6 cm thick foam core, a 0.5 mm thick dielectric substrate containing the EBG, a 1.4 cm thick foam layer between the EBG and antenna, and 2 mm thick composite skins on the top and bottom. The antenna is shown on the inner surface of the upper composite sheet in Figure 5.14, but could alternatively be located on the outer surface by using a different impedance matching technique.

Next, the use of vias was carefully considered. Vias are a significant factor in mushroom-like EBG designs, to the extent that a polarization-sensitive EBG can be created simply by manipulating the point at which the via connects to the metallic

patches [64]. This is important from a structural integration perspective because through-thickness reinforcement in composites can be accomplished with so-called Z-pins that potentially could also be used as vias in a mushroom-like EBG. However, the exact position of the Z-pins cannot be precisely controlled during insertion into the structure thereby introducing a significant variable into the design. This risk, combined with a desire to simplify the manufacturing process, drove the design away from incorporating vias in any form. It was also noted that the impedance equation for a surface without vias does not change for the TE case, and varies with the incident angle, $\boldsymbol{\theta}$, by a factor of $\mathbf{cos^2}\,\boldsymbol{\theta}$ for the TM case [64].

A review of the literature revealed that EBGs are commonly designed to operate around a single resonant frequency; however, broadband operation is desired in this case. Considering that the active region of a spiral antenna moves outward from the center as the frequency of operation decreases, a design concept was developed in which rings of patches that were each sized for a different operating frequency were arranged concentrically with the highest frequency ring being the innermost of the set. A similar scheme, known as a progressive EBG was described by Palreddy [65], although this was in actuality a conventional Cartesian EBG consisting of patches designed to resonate at three different frequencies for Ku band operation. The focus here will be on a circular EBG at UHF frequencies which is more similar to those previously studied by Tanabe et al. for operation from 1 to 10 GHz [66, 67].

To begin the design of the circular EBG, seven frequencies were selected across the desired operating band, and these are shown in the first column of Table 5.2. Using the simplifying assumption that Equation 5.1 remains unchanged in the absence of vias, Equation 5.3 was rearranged to solve for the capacitance at each frequency and the resulting values are shown in the second column of Table 5.2. Amiri et al. modified Equation 5.2 for use on a circular EBG as shown in Equation 5.4, where r_i and r_o are the inner and outer radii of the patch, w is the width of the patch, and

g is the space between the patches [68]. The inner two rings were designed using this equation by plotting the capacitance as a function of r_o and selecting the value of r_o from the graph at the point at which the capacitance, C, achieves the desired value. The initial inner radius, r_i, was assumed to be 3 cm, and the spacing between consecutive rings was initially selected as 1 cm. The values of g were derived from the number of patch/gap unit cells in each ring. The number of patches in the center ring was selected as 24 and the second ring was selected as 48, based on previous work [69] in which a larger number of patches was observed to cause the zero reflection phase for the angular mode to occur at a lower frequency.

Table 5.2: Calculated dimensions for initial EBG.

Frequency (MHz)	C Required (pF)	Rect. Patch Length (cm)	r_o (cm)	r_i (cm)	Num. (Cells)
725	0.767	-	7	3	24
625	1.032	-	15	8	48
570	1.462	3.28	19	16	28
505	1.798	3.89	23.4	20	28
455	2.232	4.59	28.3	24.4	28
430	2.519	5.07	33.3	29.3	28
300	2.867	5.60	38.5	34.3	28

$$C = \frac{\epsilon_0(1+\epsilon_r)}{\pi} \cosh^{-1}\left(\frac{w+g}{g}\right)\left[r_o \ln\left(\frac{r_o}{r_i}\right) - r_o + r_i\right] \tag{5.4}$$

After using 5.4 to design the two center rings, it appeared that the aspect ratio of the patches designed for subsequent rings was becoming too large. The patches were much longer in the radial direction than in the angular direction, and thus a different approach was used to size the metallic patches for the five outer rings. The concept of converting a square EBG to a circular EBG by maintaining the surface area of the metallic patches has been studied previously [70, 71], and this was the approach used to calculate the patch sizes for the outer rings. The method involves

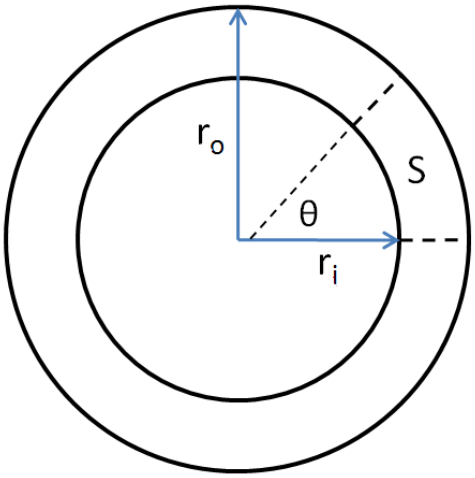

Figure 5.15: Parameters needed to calculate the area of partial circular sector, S.

first calculating the required Cartesian patch length using Equation 5.2 in conjunction with the desired capacitance value, and subsequently calculating the area of the patch by squaring the length. Next, we consider the equation for determining the area of a circular section, shown in Equation 5.5, along with Figure 5.15 which illustrates the parameters of Equation 5.5 needed to determine the area of the partial circular sector, S. By rearranging Equation 5.5 as shown in Equation 5.6, we can solve for the outer patch radius (r_o) using the previously calculated area of the square patch, an assumed initial value of the inner radius (r_i), and the angle subtending the patch, $\boldsymbol{\theta}$. The number of patches per ring was selected as 28, because, as pointed out by Amiri et al. [68], the patches begin to approach a rectangular shape as the number of cells increases. Therefore, the required angle subtending each patch is 11.77°, and the angle subtending each gap is 1.08°. The fourth and fifth columns in Table 5.2 show the inner and outer radii for each ring, and the resulting EBG is shown in Figure 5.16.

$$\boldsymbol{A = \frac{\theta}{2}(r_o^2 - r_i^2)} \tag{5.5}$$

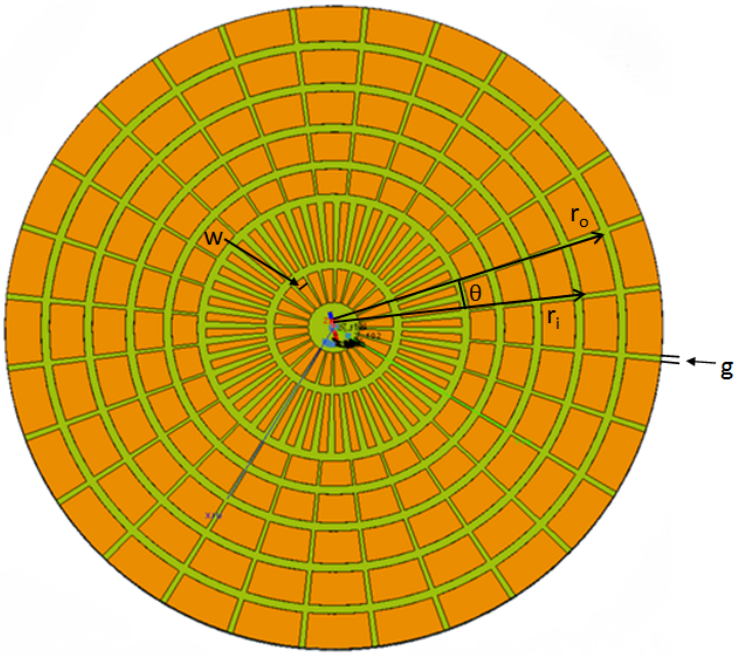

Figure 5.16: Initial EBG design with outer diameter of 77 cm and constant 1 cm ring spacing.

$$r_o = \sqrt{\frac{2A}{\theta} + r_i^2} \tag{5.6}$$

FEKO was then used to simulate the structure of Figure 5.14 with the EBG inserted as the high impedance surface layer. As seen from the black line in the plots of Figures 5.17 to 5.19 the axial ratio is better than 3 dB above 495 MHz, the gain varies between 6 and 10 dBic between 425 and 800 MHz, and the S_{11} is below -10 dB across the frequency band.

Given that the axial ratio was worse than 3 dB below 495 MHz, the outer rings of the EBG were re-sized for a wider frequency spacing between rings using the previously described procedure. Table 5.3 shows the new dimensions which resulted in a 3 cm increase in the outer radius of the EBG. Additionally, the space between the outer five rings was changed from constant 1 cm gaps to a tapered scheme in which gap spacing increased with the radius of the EBG as depicted in Figure 5.20. Beginning with the gap between the third and fourth rings from the center, the space

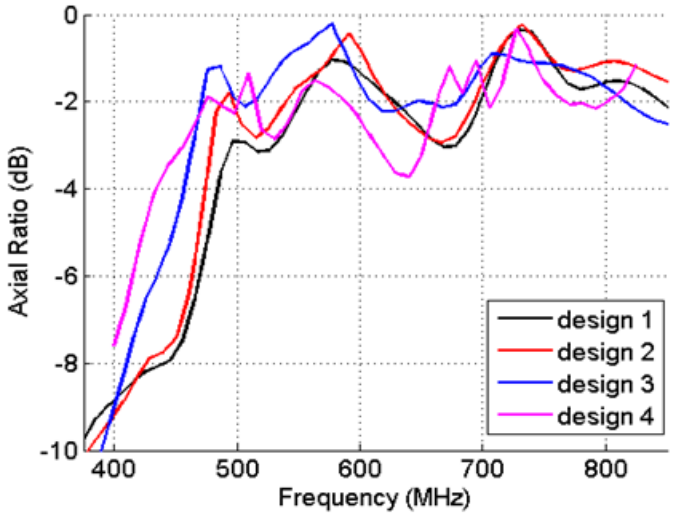

Figure 5.17: Simulated axial ratio for the circular EBG.

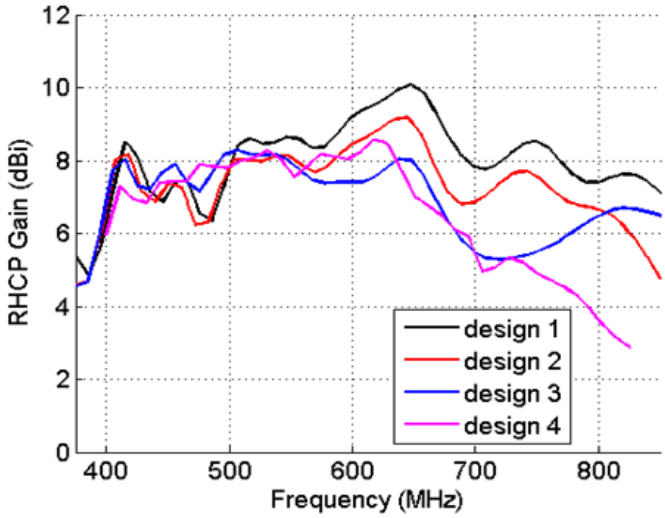

Figure 5.18: Simulated gain for the circular EBG.

between rings was set to 0.4, 0.8, 1.2, and 2.4 cm. The simulation results are shown by the red line in Figures 5.17 to 5.19. As seen, the axial ratio is above 3 dB above 480 MHz, the gain is greater than 7 dBic over most of the band, and S_{11} has improved above 500 MHz. Thus, the frequency at which the axial ratio falls below 3 dB was extended downward by 15 MHz with the cost being a decrease in gain of 0.5 to 1 dB above 600 MHz.

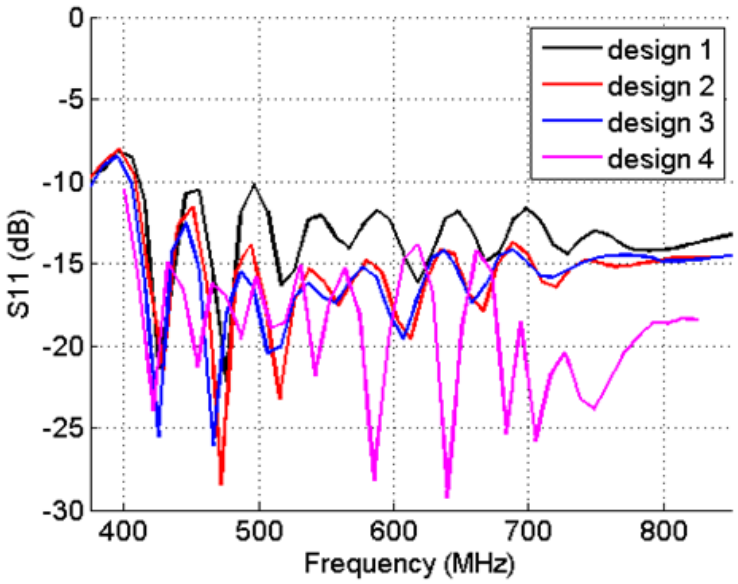

Figure 5.19: Simulated S_{11} for the circular EBG.

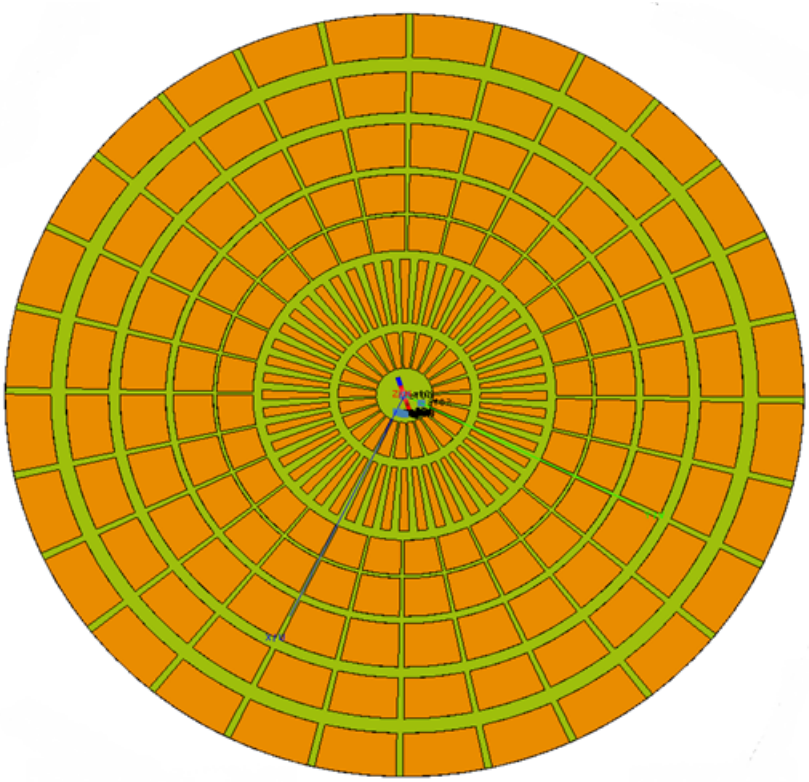

Figure 5.20: Revised EBG design with outer diameter of 83 cm and tapered ring spacing.

Drawing on the idea of the cavity-backed spiral antenna, a conductive side wall was added between the ground plane and the EBG layer as shown in Figure 5.21. The patches in the outermost ring of the EBG are in contact with the wall. This complicates mechanical fabrication, but as seen by the blue line in the simulation results of Figures 5.17 to 5.19, the axial ratio, gain and S_{11} are all within the acceptable range above 465 MHz. This represents an improvement of 15 MHz over the previous design, and inspection of the plot in Figure 5.17 in the region below 465 MHz shows that it is again the axial ratio that falls outside the threshold value of 3 dB. As was noted for the second design iteration, the gain has decreased in the upper half of the desired operational frequency range.

Several additional iterations were made on the design of Figure 5.21 to arrive at the configuration shown in Figure 5.22. The following points summarize the changes that were made.

1. Simulations showed that the outer ring had minimal effect and could be eliminated, thus reducing the outer diameter of the structure to 71.4 cm.

2. The 48 element patch ring was eliminated and the patches in the inner ring were moved outward 2 cm and lengthened to 10.5 cm as suggested in [70].

Table 5.3: Calculated dimensions for re-sized EBG.

Frequency (MHz)	C Required (pF)	Rect. Patch Length (cm)	r_o (cm)	r_i (cm)	Num. (Cells)
725	0.77	-	7	3	24
625	1.03	-	15	8	48
525	1.46	3.7	19.7	16	28
475	1.80	4.3	24.1	20.1	28
425	2.23	5.1	29.4	24.9	28
400	2.52	5.6	35.1	30.6	28
375	2.87	6.2	41.5	37.5	28

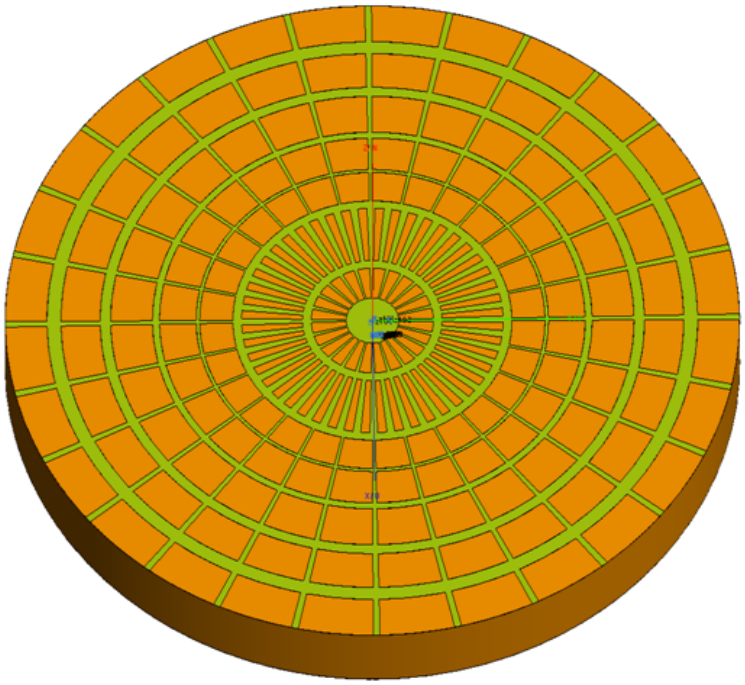

Figure 5.21: Metallic wall added below the EBG layer.

3. The conductive wall was extended upward 1.4 cm to meet the inside of the upper face sheet.

The results of these changes can be seen by the magenta line in the graphs of Figures 5.17 to 5.19. The S_{11} plot (Figure 5.19) shows little change at the lower end of the frequency band but an improvement at the upper end. The simulated gain is also similar to the results for the previous design up to 730 MHz, but begins to decrease beyond this frequency. While not desirable, it is noted that the predicated gain of 3.6 dB at 800 MHz is still within the acceptable range. The axial ratio is generally lower across most of the frequency band with a slight dip outside the acceptable range to -3.7 dB at 640 MHz. However, it can also be seen that the slope of the line is more gradual from 430 MHz to 475 MHz; suggesting that it might be possible to improve the axial ratio at lower frequencies with additional design modifications.

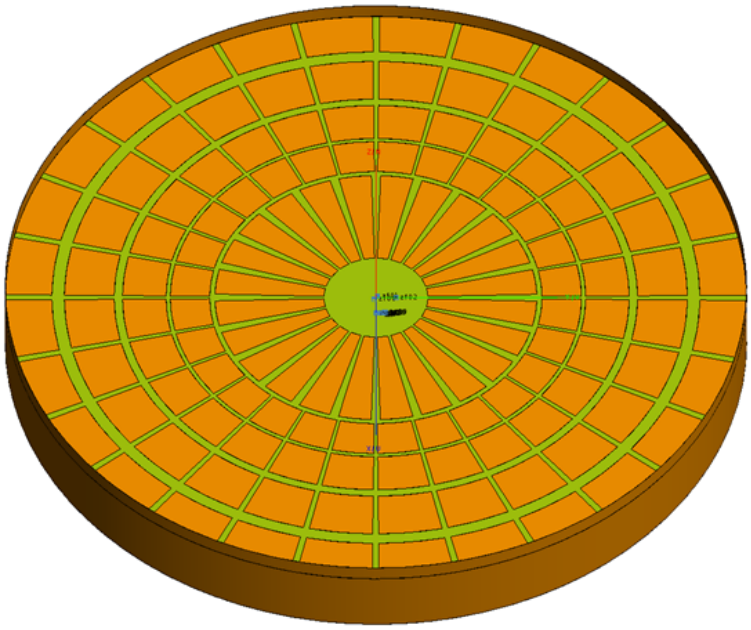

Figure 5.22: Modified EBG with longer center patches.

5.5 Structural EBG Prototype

Given that the major change to the EBG of Figure 5.22 was a lengthening of the inner row of patches in the radial direction, another round of simulations was conducted to investigate the effects of lengthening additional rows of patches. The following is a list of changes that were made to the EBG configuration to arrive at the surface shown in Figure 14a, which is a photograph of the prototype EBG.

1. The radial patch length of the innermost ring was set to 6.3 cm and the inner edge of the ring was moved 5 mm inward.

2. The patches in row two were lengthened to 6.75 cm and the inner edge of the ring was moved 3.25 cm inward.

3. The patches in the two outer rows were merged to give an overall radial length of 10.3 cm.

4. The innermost and center inter-ring gaps were set to 9 mm and 5 mm, respectively.

The prototype was fabricated by transferring the spiral antenna and patch geometry to copper clad boards and employing an acid etching technique to remove unwanted copper. The transfer process was unique in that the copper clad boards were covered with tape and a laser was used to cut the tape to form the desired geometry. Before placing the boards in the etching tank, the tape was removed in the areas where copper was to be etched, and left in place to prevent etching in desired areas. This process was used to create both the EBG and spiral antenna. The bluish cast on the patches in Figure 5.23 is due to the tape still being in place.

To create the Dyson balun, the shield of an RG223 co-axial cable was bonded along the length of one spiral arm using conductive epoxy (Epoxy Technology, Inc., H20E), and the center conductor was bonded to the opposite arm at the feed point at the center of the spiral. The attachment of the Dyson balun in the area of the antenna feed point is shown in Figure 5.24. The final step prior to assembly of the structure was to machine Rohacell foam into two, 71.4 cm diameter cylinders with

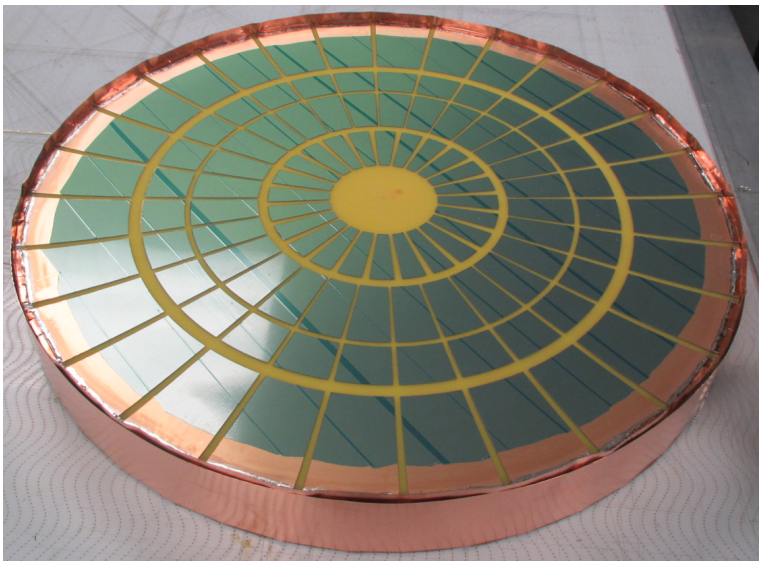

Figure 5.23: Prototype EBG with elongated patches.

Figure 5.24: Attachment of the Dyson balun.

the required thicknesses of 6 cm and 1.4 cm.

The prototype structure of Figure 5.25 was constructed by stacking the various layers as depicted in Figure 5.14: the lower fiberglass sheet with an integrated layer of copper mesh, 6 cm foam core, EBG, 1.4 cm foam core, and the top fiberglass layer containing the antenna. Copper tabs were soldered to the outermost patches of the EBG and bent upwards at a 90° angle to enable contact with the cavity wall. A copper sheet was then wrapped around the foam core to make mechanical contact with the tabs on the EBG and form the side of the cavity.

Measured data was collected using the prototype structure. An Agilent E5071C VNA was used to measure S_{11} of the prototype, and the same experimental setup shown in Figure 4.13 was used for the measurement. The measured and simulated S_{11} data are shown in Figure 5.26. The difference between the two traces is because the simulated data is shown with reference to 150 Ω.

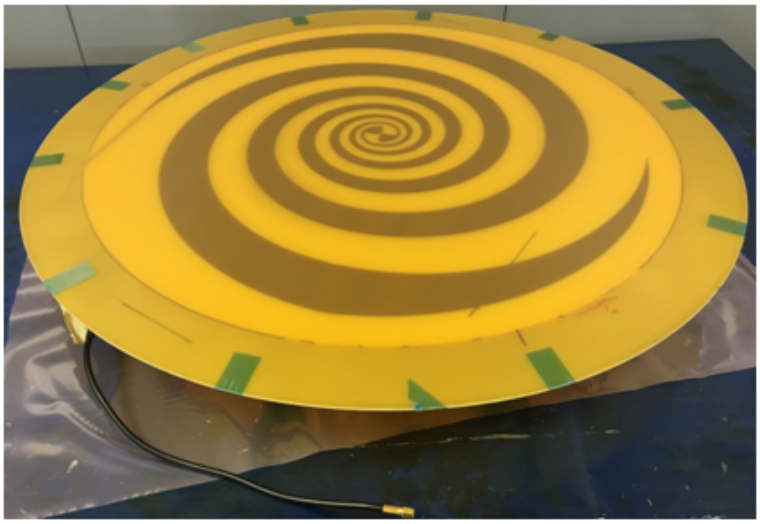

Figure 5.25: Prototype EBG Structure.

The prototype then underwent testing in a Satimo anechoic chamber, and the measured and simulated axial ratio is shown in Figure 5.27. There are two interesting observations regarding the axial ratio data. The first is that the drop in axial ratio occurs at a lower frequency and is more severe than was shown by simulations. The second point is that the measured axial ratio is much better than the simulated data below 430 MHz, and the antenna may actually achieve acceptable performance below 400 MHz. However, this could not be investigated because the low end of the measurement range for the Satimo chamber was 400 MHz. The axial ratio generally meets the 3 dB requirement across the desired frequency range other than over a narrow, 25 MHz band from 505 MHz to 530 MHz.

A comparison of the simulated and measured peak gain is shown in Figure 5.28. The gain roll-off occurs approximately 85 MHz lower in the measured data than in the simulation. Nevertheless, the measured gain recovers from the roll off more quickly and remains between 4 and 5 dB from 530 MHz to 800 MHz. As was observed for the axial ratio, the gain requirement of 3 dB or better is realized across the band with the exception of a 11 MHz band from 515 MHz to 526 MHz.

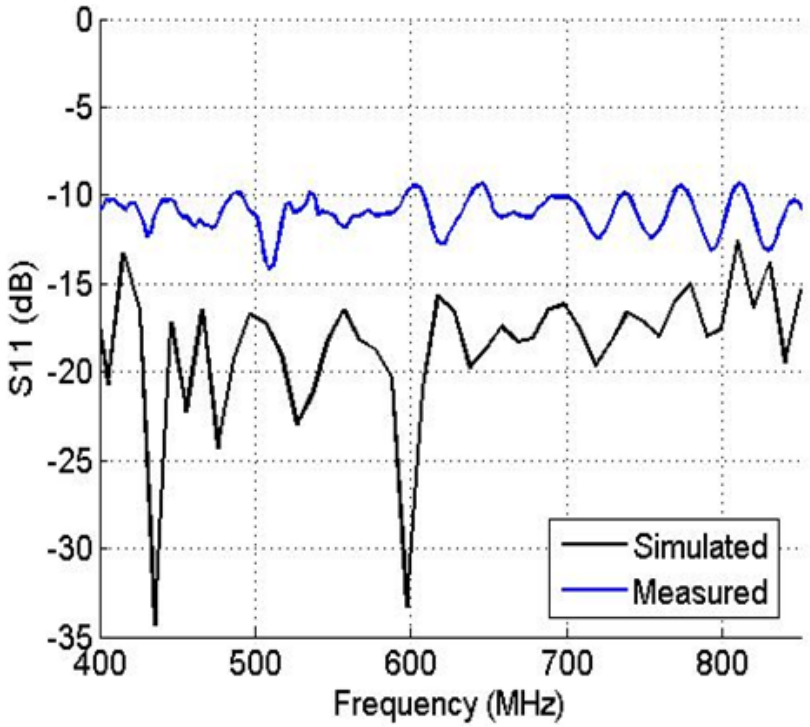

Figure 5.26: Measured and simulated S_{11} for the prototype structure.

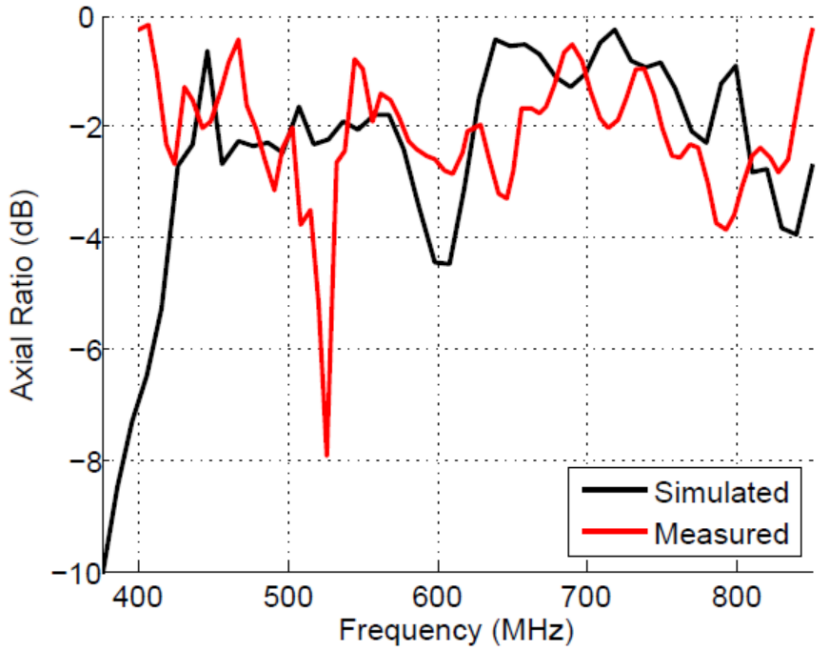

Figure 5.27: Measured and simulated axial ratio for the prototype structure.

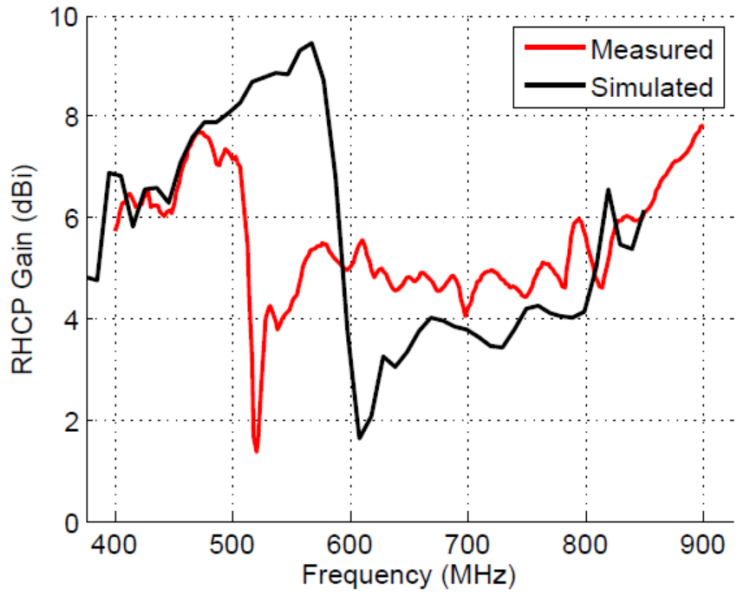

Figure 5.28: Measured and simulated gain for the prototype structure.

To determine the cause of the roll off in gain and axial ratio, the design information in Tables 5.2 and 5.3 was studied along with the simulation results in Figures 5.17 and 5.18. A comparison of the radial patch length for the five outer rings in each design is shown in Table 5.4, and it is noted that the patches in design 2 are longer. Comparing the simulated gain for these designs in Figure 5.18, the gain at the upper end of the band is lower for design 2 than design 1; however, as seen on the axial ratio plot in Figure 5.17, design 2 has better axial ratio performance at the lower end of the desired operating range.

Table 5.4: Comparison of radial patch length in designs 1 and 2. (cm)

Ring	Design 1	Design 2
3	3.0	3.7
4	3.4	4.0
5	3.9	4.5
6	4.0	4.5
7	4.2	4.8

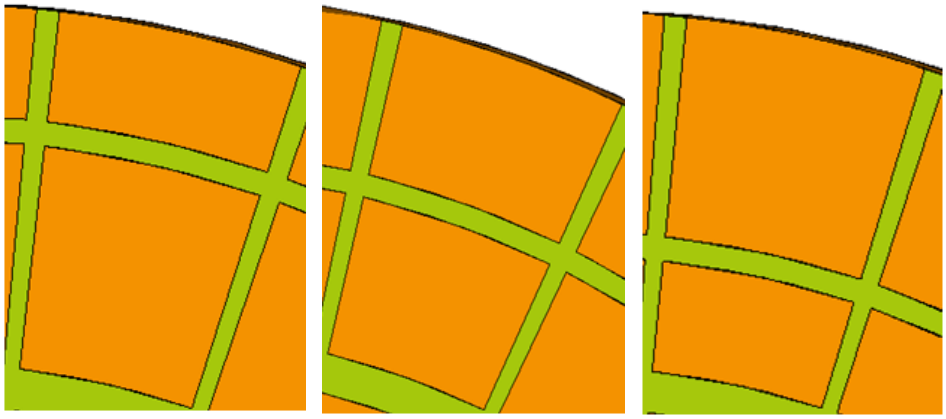

(a) Case 1. (b) Case 2. (c) Case 3.

Figure 5.29: Test cases to study patch length impact on gain roll off.

Design 4 was the next case where patch length was increased with the innermost row of the EBG being lengthened. As seen by the magenta line in the graphs of Figures 5.17 to 5.18, axial ratio at the low end of the frequency band has improved and both a dip in axial ratio and roll off in gain are also present. These observations led to the hypothesis that a longer radial patch length promotes axial ratio performance at the lower frequencies, but this comes at the cost of gain at higher frequencies.

Another round of simulations was conducted to test this hypothesis. The experiment considered effects of changes in radial patch length in the outermost patch ring where the largest patches are located. Figure 5.29 shows the three different cases considered in which a 7 mm gap is introduced at three different points along the length of the patch. For the first case shown in Figure 5.29a, the gap is positioned to set up a radial patch length of 3.2 cm in the outer row of patches. In the second case (Figure 5.29a), the patch length is 4.7 cm, and Figure 5.29c shows the gap positioned to establish a 6.4 cm patch length in the outermost ring.

The simulated gain and axial ratio for the three different patch lengths are shown in Figure 5.30 and 5.31 , respectively. The gain plot clearly shows that as the patch length increases, the gain rolls off at a sharper rate. The simulated gain for the prototype EBG, with an outer row patch length of 10.3 cm, is shown by the dashed

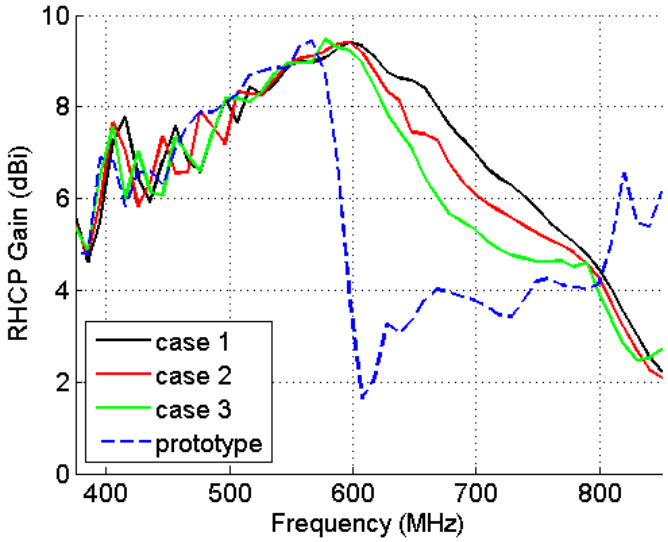

Figure 5.30: Simulated gain showing effect of patch length in the outermost row.

line for reference.

Several observations can be made on the axial ratio plot. First, the dip at 600 MHz is seen to become more pronounced as the patch length increases, ultimately reaching the value for the prototype structure shown by the dashed line. Second, an improvement in axial ratio can be seen in the 400 MHz to 425 MHz range as the patch length is increased. Finally, after getting worse in each of the test cases at the upper end of the frequency band, the axial ratio improves from approximately 630 MHz to 750 MHz for the 10.3 cm patch length used on the prototype EBG.

Based on the test case results, it appears that the lengthening of the patches does improve axial ratio at the lower end of the operating band, but this comes at the expense of gain at the high end of the frequency band. The long patch length was also seen to cause the abrupt drop off in axial ratio that occurred at 600 MHz in the simulations. It is believed that the length of the patch sets up a parasitic coupling to the adjacent arm. Figure 5.32 shows an overhead view of the spiral and EBG, and it is clear that the EBG patches extend under adjacent arms at several points along the length and at the ends of the arms that could promote coupling. Tanabe

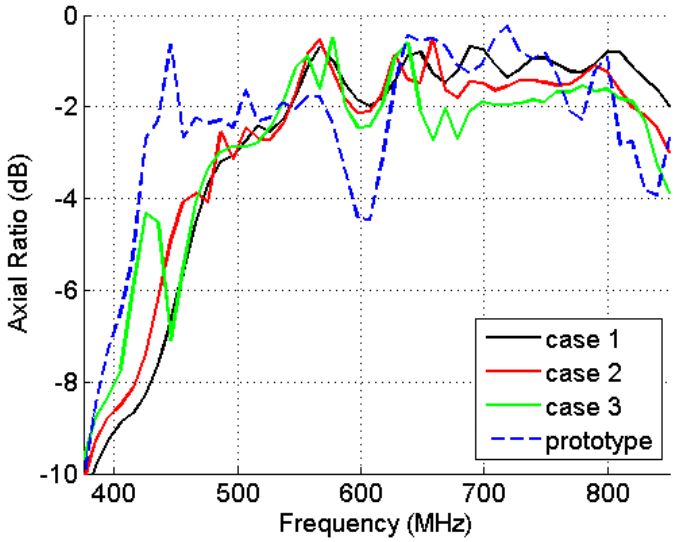

Figure 5.31: Simulated axial ratio showing effect of patch length in the outermost row.

et al. showed that shorting the ends of an Archimedean spiral to the adjacent arm improved axial ratio at the lower end of the antenna's operating range[71], and the capacitive coupling seems to provide a similar effect here.

To further investigate the effects of interaction between the spiral arms, another set of simulations was performed with the arms shorted at different locations, as indicated by points A, B, and C in Figure 5.32. There were no changes to the length of any of the EBG patches for these simulations; the only change was the introduction of the short circuits to the FEKO model of the prototype structure. Figure 5.33 shows the effect of the short circuits on the axial ratio. As seen, at position A where the arms are closer together, the drop off in axial ratio is more severe with the short in place and thus enhancing interaction between the adjacent arms. At point B, there is more separation between the arms and the effect is less severe; although it is still worse than the for prototype with no short. Finally, with a short at point C, the drop off in axial ratio is slightly better than for the prototype at 600 MHZ, but otherwise axial ratio is seen to be generally worse from 425 MHz to 800 MHz. Interestingly, at the low end, there is some evidence of improvement in axial ratio with the short in

place as described by Tanabe.

Figure 5.34 shows the effect of the shorted arms on gain. The main impact of the short is seen just above 600 MHz where the shorts at points A and B make the gain roll-off worse, and the short at point C results in a slight improvement over the non-shorted case. Outside of this point, the shorts have minimal impact and result in at most a 1.5 dB variation in gain compared to the prototype.

The measured radiation pattern for the prototype structure taken at 520 MHz is shown in Figure 5.35. This pattern is obviously not what is desired, but such a result is not unexpected given the axial ratio plot in Figure 5.27. However, outside of this region, the pattern is fairly consistent across the frequency range of 400 MHz to 800 MHz as seen in the plots of Figure 5.36.

The measured efficiency is shown in Figure 5.37. As seen, the efficiency is -3 dB or better over most of the desired 425 MHz to 800 MHz operating band, with

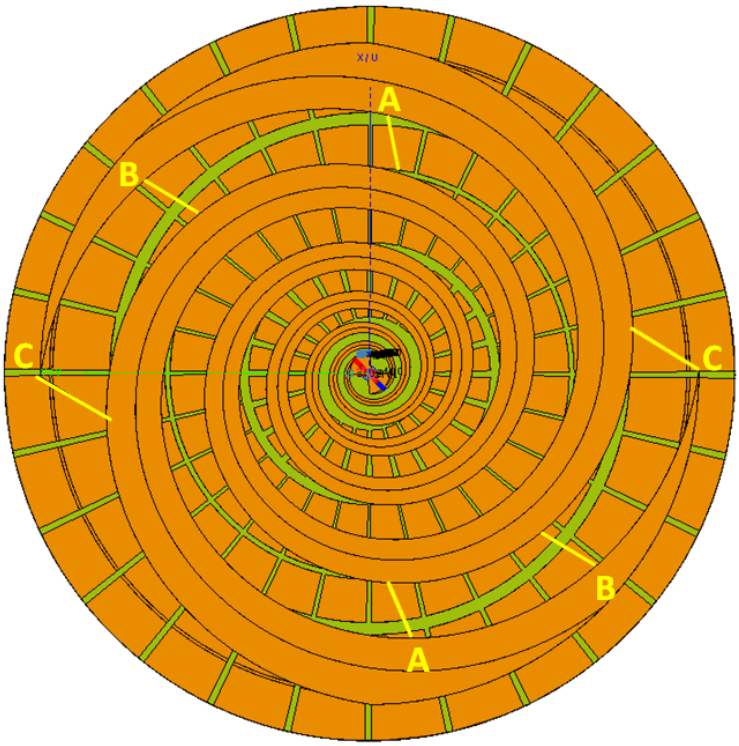

Figure 5.32: Overhead view of the spiral antenna above the EBG.

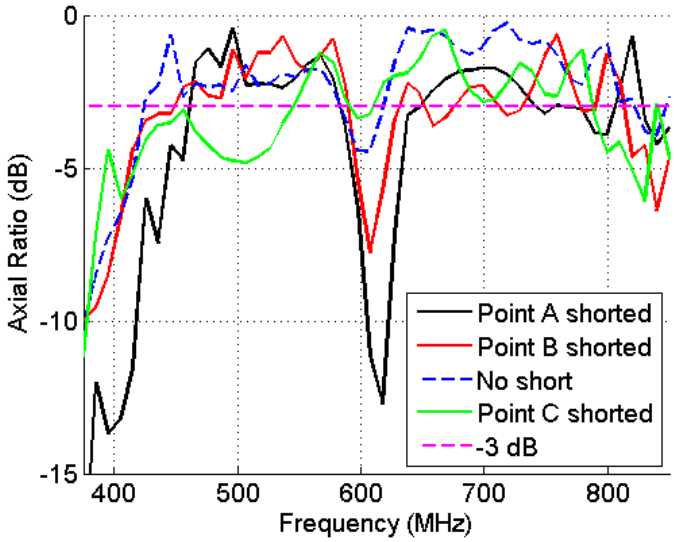

Figure 5.33: Impact of shorted spiral arms on simulated axial ratio.

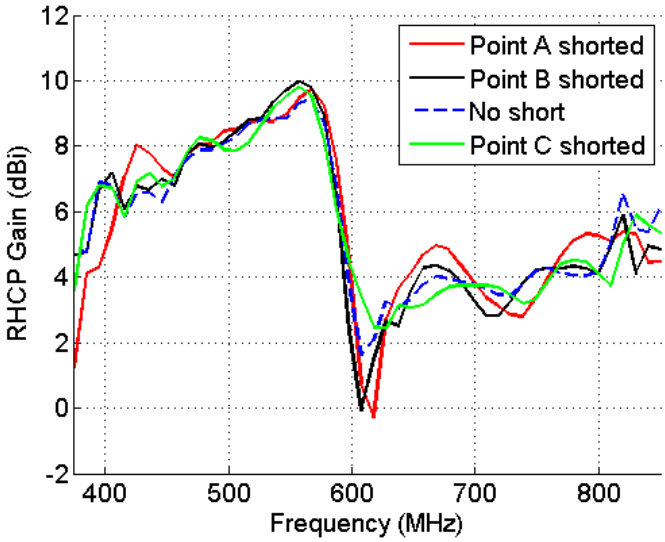

Figure 5.34: Impact of shorted spiral arms on simulated gain.

the average efficiency being -2.75 dB. The lowest efficiency occurs at 520 MHz and coincides with the gain roll-off that was discussed previously. There are a number of factors contributing to inefficiency in the prototype. Obviously, resistive loss in the spiral arms and dielectric loss in the fiberglass composite material are both present. The Dyson balun is another source of loss. First, the balun was attached to the spiral

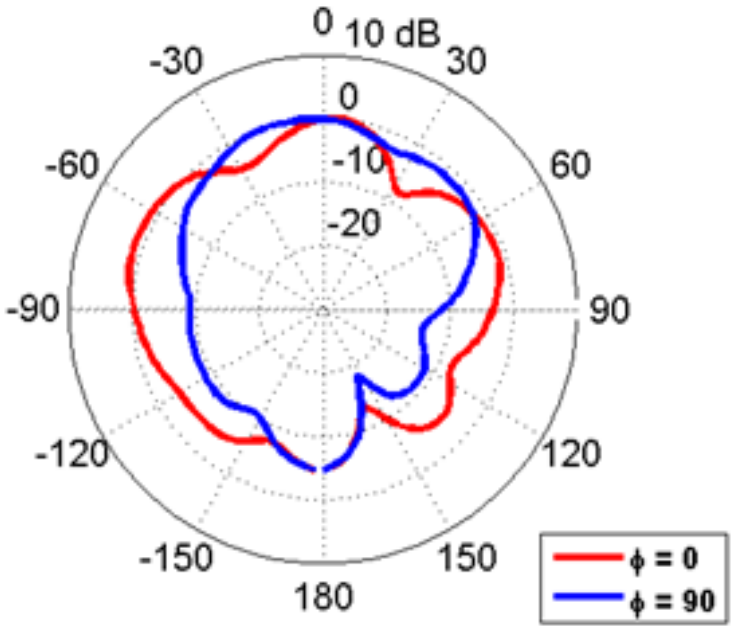

Figure 5.35: Measured radiation pattern at 520 MHz.

arm with conductive epoxy. Although this establishes a good electrical connection, there is more resistive loss with epoxy because it is less conductive than solder. Second, the cable that was used to implement the balun is 9 feet long. Based on the data sheet for RG223 cable, the loss for this cable length is estimated to range from 0.8 dB at 425 MHz to 1 dB at 800 MHz [72]. Finally, mismatch loss is also a factor, given that S_{11} is near -10 dB in the frequency band of interest, as seen in Figure 5.26.

5.6 Simulation on Fuselage Section

Section 5.1 illustrated the effects of carbon fiber bulkheads placed in the proximity of a conformal spiral antenna on the top surface of a UAV fuselage. In this section, the simulated and measured performance of the EBG structure is compared to simulated results when the structure is installed on a fuselage section similar to that used in the conformal antenna study. There were three bulkheads included in the fuselage model for this analysis, and the EBG assembly was positioned directly above the center bulkhead as shown in Figure 5.38 where a portion of the skin has been removed to

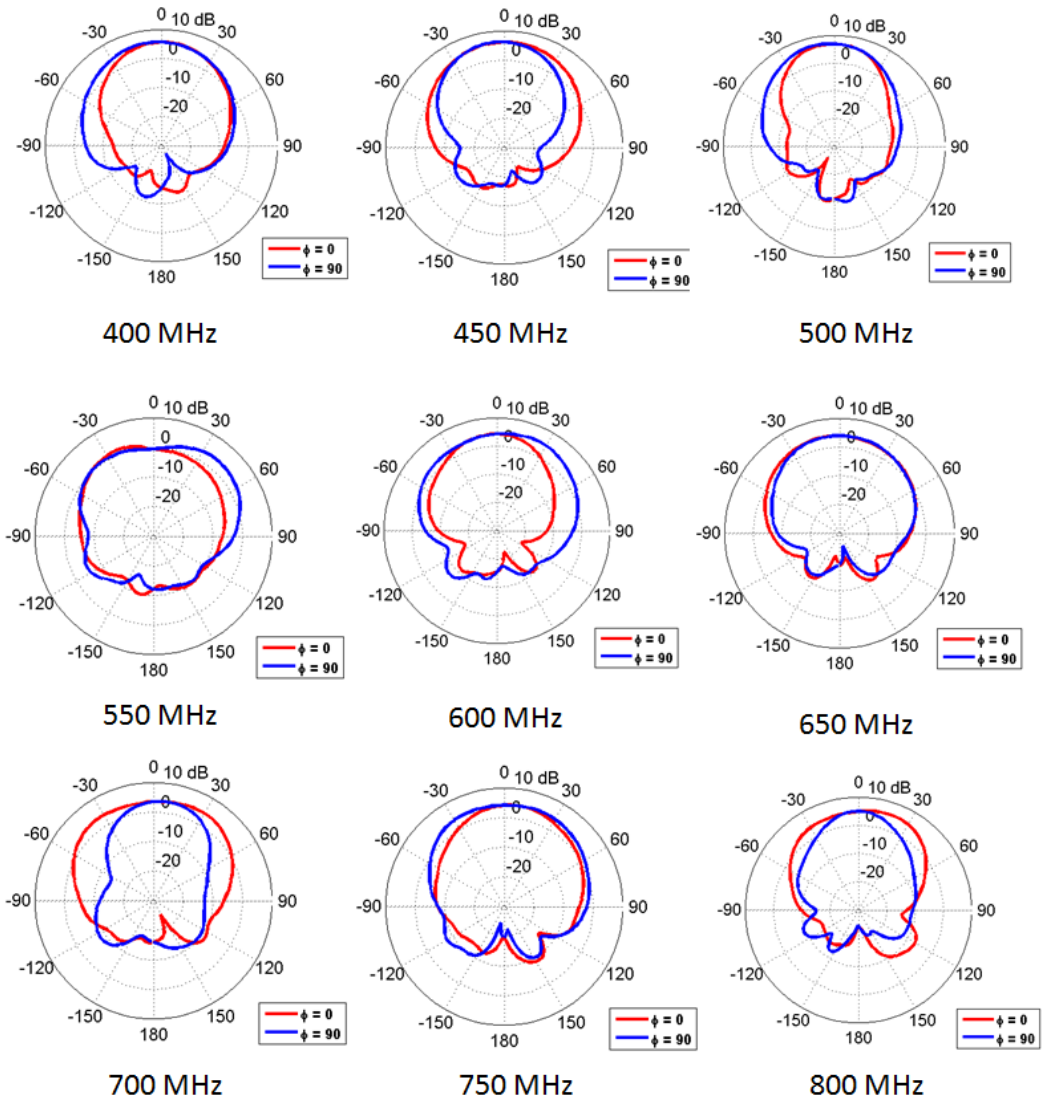

Figure 5.36: Measured radiation patterns for the prototype structure.

reveal the antenna location. The two remaining bulkheads were situated on either side of the center bulkhead and 24.3 cm away from the forward and aft edges of the EBG assembly. These bulkheads are also visible in the figure. Simulations were conducted at 425 MHz, 600 MHz, and 800 MHz with the results shown in Figure 5.39 where the left and center columns show the simulated and measured gain of only the EBG assembly, and the right column shows the simulated gain of the EBG assembly installed on the fuselage.

At 425 MHz, close agreement between all data sets can be seen from a comparison

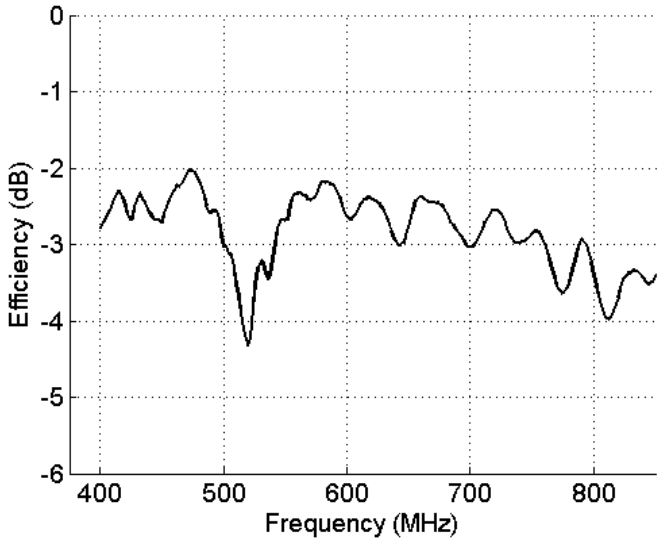

Figure 5.37: Measured efficiency of the prototype.

of the simulated and measured results for the standalone EBG structure and the simulated data from the combined EBG/fuselage model. Similar results were also obtained for the simulated structures at 800 MHz in the bottom row of Figure 5.39. The measured data from the prototype generally agrees with the simulated data for the standalone EBG although it is noted that the beam is not as broad as predicted

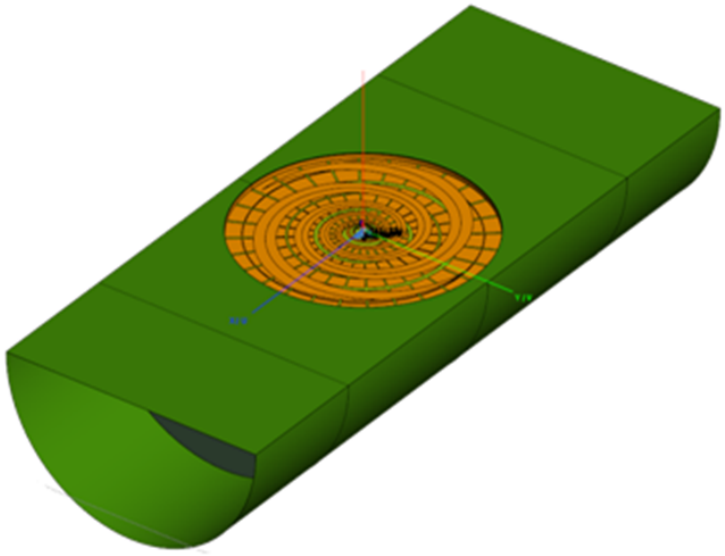

Figure 5.38: Fuselage section showing location of EBG assembly.

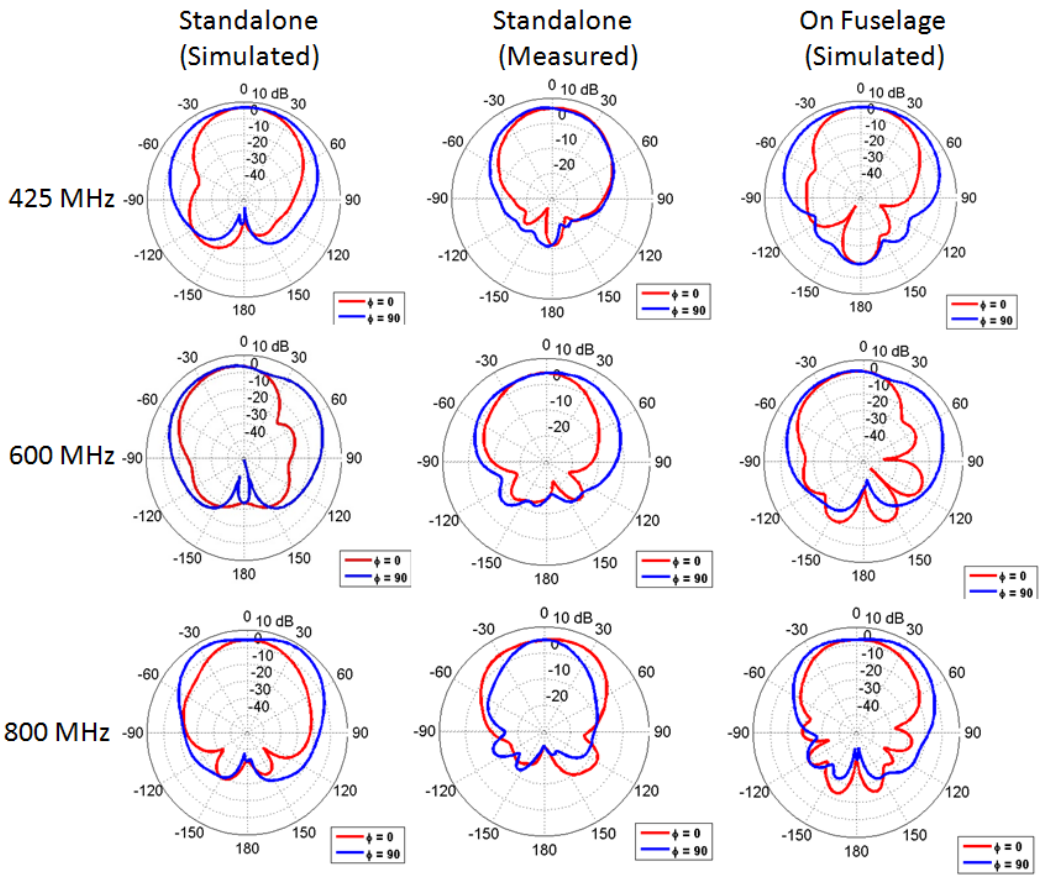

Figure 5.39: Comparison of radiation patterns of standalone vs. installed EBG assembly.

in the $\varphi = 90°$ plane. At 600 MHz, simulations predict structural interaction as seen by comparing the $\varphi = 0°$ plane for the two simulated cases. The null at $\vartheta = 45°$ for the standalone EBG assembly has been reduced by approximately 4 dB for the combined EBG/fuselage model. We also see a deep null at $\vartheta = 90°$ for the fuselage model that is not present in the simulated standalone EBG pattern. Interestingly, the measured data shows no evidence of the null at $\vartheta = 45°$. This is likely due to the difference in frequency at which the gain and axial ration roll-off occurred between the simulated and measured data. In general, the simulations indicated minimal impact on radiation patterns from the conductive bulkheads at the frequencies considered.

Chapter 6

Contributions and Future Work

6.1 Contributions

The focus of this dissertation research was on the analyses, design, and development of structurally integrated VHF and UHF antennas. As stated earlier, antennas with more bandwidth and higher efficiency could be developed if the space and materials available in an aircraft could be judiciously exploited and optimized for multifunctional usage. This is improbable with bolt-on approaches, such as blade antennas or antennas housed within a wing pod or fairing.

As an analysis tool, first a method called Characteristic Mode Analysis (CMA) is studied and used both for a dipole antenna and a VHF airfoil integrated antenna. The significance of CMA lies in its ability to identify, select and optimize the radiating modes of a structure without considering the excitation. Thus CMA is an ideal technique to understand the modes as function of the geometry and material parameters of the structure. Although computationally intensive, it provides fundamental insights on the significance of each mode, modal interactions, and overall achievable bandwidth. Although CMA can be performed using commercial Method of Moments (MoM) solvers, such as FEKO, that does not help in the understanding of the underlying fundamentals of the method. This is why the CMA of a dipole antenna loaded with a thin coating ($\lambda_0/2000$, where λ_0 is the free-space wavelength) of DNG material is undertaken. The presented analysis considers the MoM Galerkin formulation. The eigenvalues and eigenvectors are computed from the generalized

impedance matrix with the help of the Toeplitz function. Initially, a standard wire dipole is studied to validate the mathematical formulation developed in MATLAB. Then a dipole with a thin DNG coating is considered and investigated. The analyses presented demonstrate that when ε_r and μ_r is between -1 and 0, the configuration shows potentials for antenna size reduction. For example, a 25% size reduction is achieved for $\varepsilon_r = \mu_r$ = -0.3.

Secondly, the study, design, and development of a broadband (2:1 frequency ratio), positive gain (> 0dBi), VHF antenna integrated within a composite structure are undertaken to overcome the limitations of very low gain (-20 dBi typical at low VHF frequencies) associated with resistively matched, electrically small, broadband, airborne blade antennas. It is demonstrated that a broadband antenna operating from 89 to 221 MHz can be incorporated into composite structures. Simulation and experimental results clearly show that such antennas can be built using structural composite materials, such as fiberglass or cyanate-ester/quartz, Rohacell foam, and conductive mesh with appropriate thicknesses commensurate with the frequency band of operation. The need for a foam buffer layer between the antenna and the dielectric skin is demonstrated, and the thickness of such a layer is optimized through simulations. Characteristic mode analyses are performed to further understand and elucidate how the presence of structural composites impact the bandwidth of the antenna as function of its modes and modal significance. Multiple antenna prototypes were built and tested, with the final one being representative of a sandwich structure consisting of fiberglass skins, Rohacell foam, and copper mesh. Experimental results for this antenna demonstrate impedance bandwidth from 89 to 221 MHz. The simulated radiation patterns show good coverage looking down for a UAV application with a simulated gain between 2 and 3 dBi across the band. The proposed sandwich structure antenna was also studied for possible MIMO application in an inverted V tail UAV configuration. The two antennas in that configuration clearly show excellent

performance based on their ECC and simulated radiation patterns.

Finally, fundamental studies and innovations are made in the topic area of structurally integrated broadband circularly polarized spiral antennas on EBG structures. As stated before, spiral antennas are very attractive for airborne satellite communications. However, to allow directional radiation, spirals require 1/4th of a wavelength separation when placed on a reflecting surface (e.g. the aircraft's ground). This thickness (as much as 6 inches or more at 450 MHz) is a significant hurdle for structural integration and is unacceptable at UHF frequencies. While RF absorbing materials have been proposed in the past they significantly reduce antenna efficiency and power handling ability. EBG structures have been studied in the literature in the context of low profile antenna design, especially dipoles. Only limited works have been reported on spirals on EBGs. No work on spirals on EBGs have been reported to our knowledge for integration with composite aircraft platforms that addresses broadband design challenges in the UHF frequency band. The final contribution of this work lies in that area. The investigation, design, and development of an equiangular spiral antenna on an EBG are conducted for 425-800 MHz satellite applications, such as the MUOS system. Starting from a mushroom EBG structure, the dependency of antenna gain bandwidth, impedance bandwidth, pattern bandwidth, and axial ratio bandwidth on the EBG geometry, materials, and height is studied through full-wave EM simulations. An antenna plus EBG with nearly an octave bandwidth is designed, built, and tested that demonstrate good CP performance (gain greater than 4 dBi RHCP and axial ratio less than 3 dB). While further optimization of gain versus axial ratio versus EBG geometry and height is quite possible the findings demonstrate the clear feasibility of a RHCP spiral antenna on a planar progressive EBG with half the thickness of a traditional spiral on a reflector for composite structural integration.

6.2 Future Work

In chapter three, a DNG coated dipole was studied in which the thickness of the coating was limited to 0.5 mm. It is believed that a lower operating frequency can be achieved by increasing the thickness of the DNG coating; characterizing the effects of increasing the coating thickness would be beneficial. Additionally, the variation of ε_r and μ_r with frequency was not studied, and including this phenomenon in the CMA calculations would increase accuracy. The physical realization of DNG material and material anisotropy are other topics that could be of interest.

The VHF antenna developed in chapter four could not be measured because of lack of access to RF measurement facilities in the required frequency range. However, the antenna could be studied further through measurements if it was scaled to a higher frequency. The cost and complexity of VHF measurements could thus be avoided, and a smaller antenna could also find use on vehicles that lack the space to implement the VHF version.

One area for further study is the impact of substructure on radiation patterns. The reinforcing structural members, such as ribs and spars, were not considered in the simulations, and developing an understanding of what materials could be used for structural components is important for implementation on an actual aircraft. In particular, a critical task is determining what percentage of the structure could be fabricated with high strength carbon fiber composites without negatively impacting RF performance. Furthermore, if the use of carbon fiber is feasible, this presents the possibility of using parts of the aircraft structure as passive elements to guide RF energy in a specific direction.

In chapter five, a structural EBG was developed in order to integrate a directional, broadband, UHF antenna with a composite structure. While a fairly practical thickness of 7 cm was achieved, additional height reduction or a lower operational frequency might be possible through the use of a multi-layer EBG. It was also observed

that the gain and axial ratio deteriorated across a narrow frequency band around 520 MHz. Simulations indicated that shorting the end of the spiral arm to the adjacent arm mitigated this problem, but had adverse effect on performance outside of this band. One solution would be to implement a shorting mechanism with either an RF switch or discrete capacitors and inductors such that the short is only active over the problematic frequency band. This idea could even be extended to include multiple shorts along the arms that could be used to optimize performance over certain portions of the operational band. Finally, while parametric studies were relied upon in this work to develop the EBG geometry, such an approach is time consuming. The development of a mathematical relationship (such as sequence or recurrence relation) that would expedite the design process and ultimately lead to design rules for patch sizes and ring spacing would be useful.

Finally, a key area for future research is to develop actual structural designs that incorporate the CLAS concepts that we have developed. This work would involve Finite Element simulations to investigate the effects of the integrated antenna on the mechanical design, development and testing of coupons to investigate the durability of bonded joints and electrical connections (e.g. the feed for the spiral), and full scale static and fatigue testing of the CLAS component. This research is multidisciplinary in nature and should be approached through a collaboration between mechanical or aerospace engineering researchers with expertise in the design of composite structures and RF researchers. This also offers an opportunity to investigate multi-domain optimization in which key RF performance parameters are incorporated into the structural design process.

Bibliography

[1] J. Cambi. (2016, Mar.) "The Drones Report: Market Forecasts, Key Players and Use Cases, and Regulatory Barriers to the Proliferation of Drones". Business Insider. Accessed 15 April 2016. [Online]. Available: http://www.businessinsider.com/the-drones-report-market-forecasts-key-players-and-use-cases-and-regulatory-barriers-to-the-proliferation-of-drones-2016-3

[2] J. Bort. (2014, Mar.) "Here's What Facebook's New Solar Powered Drone Looks Like". Business Insider. Accessed 8 Oct 2015. [Online]. Available: http://www.businessinsider.com/facebooks-solar-powered-drone-2014-3

[3] J. Yarow. (2014, Apr.) "Google Buys Drone Company Titan Aerospace". Business Insider. Accessed 8 Oct 2015. [Online]. Available: http://www.businessinsider.com/google-buys-drone-company-titan-aerospace-2014-4

[4] Amazon Incorporated. (2015, Oct.) "Amazon Prime Air". Accessed 15 Jan 2016. [Online]. Available: http://www.amazon.com/b?node=8037720011

[5] K. Atherton. (2015, May) "Google's High-Flying Internet Drone Crashed in New Mexico Weeks Ago". Popular Science. Accessed 29 September 2015. [Online]. Available: http://www.popsci.com/googles-high-flying-internet-drone-crashes-outside-albuquerque

[6] Insitu Inc. (2015) "RQ-21A Blacjack". Accessed 14 Oct 2015. [Online]. Available: www.insitu.com/systems/integrator/rq-21a-blackjack

[7] P. Callus, "Novel Concepts for Conformal Load-bearing Antenna Structure," Defense Technical Information Center, Fort Belvoir, VA, Technical Report, 2007.

[8] A. Lockyer, K. Alt, J. Kudva, R. Kinslow, and A. Goetz, "Structural finite-element modeling strategies for conformal loadbearing antenna structure (CLAS)," in *Proc. SPIE 3046, Smart Structures and Materials 1997*, 1997, pp. 166 – 172.

[9] A. Lockyer, K. Alt, D. Coughlin, M. Durham, J. Kudva, A. Goetz, and J. Tuss, "Design and development of a conformal load-bearing smart skin antenna: overview of the AFRL Smart Skin Structures Technology Demonstration S3TD," in *Proc. SPIE 3674, Smart Structures and Materials 1999*, SPIE, Ed., July 1999, pp. 410–424.

[10] U B Corporation. (2015) "UHF Blade Antennas". Accessed 21 Sep 2015. [Online]. Available: http://www.ubcorp.com/products/products-blade-antennas/command-blade-uhf.html

[11] Mesoscribe Technologies Inc. (2011, Feb.) "Conformal Load Bearing Antenna by Direct Write on Wing to Body Fairing". Accessed 8 Jan 2015. [Online]. Available: www.mesoscribe.com/conformal-load-bearing- antenna-by-direct-write%E2%84%A2-on-boeing-component/

[12] J. Volakis, C. Chen, and K. Fujimoto, *Small Antennas: Miniaturization Techniques & Applications*. McGraw-Hill, 2010, pp. 2-3.

[13] D. Sievenpiper, D. Dawson, M. Jacob, T. Kanar, S. Kim, J. Long, and R. Quarfoth, "Experimental Validation of Performance Limits and Design Guidelines for Small Antennas," *IEEE Transactions on Antennas and Propagation*, vol. 6, no. 2, 2012, DOI:10.1109/TAP.2011.2167938.

[14] K. Nicholson, W. Rowe, P. Callus, and K. Ghorbani, "Small Slot Design for Slotted Waveguide Antenna Stiffened Structure," *Electronic Letters*, vol. 48, pp. 676–677, June 2012.

[15] D. Gray, K. Nicholson, K. Ghorbani, and P. Callus, "Carbon fibre reinforced plastic slotted waveguide antenna," in *Proceedings of Asia-Pacific Microwave Conference 2010*, Dec. 2010, pp. 307–310.

[16] D. Banks, M. Berden, W. Baron, and J. Tenbarge, "Structurally integrated x-band array development," in *Multifunctional Structures / Integration of Sensors and Antennas. Meeting Proceedings RTO-MP-AVT-141*, RTO, Ed., 2006, pp. 17.1–12.

[17] C. You and W. Hwang, "Design of load-bearing antenna structures by embedding technology of microstrip antenna in composite sandwich structure," *Composite Structures*, vol. 71, pp. 378–382, 2005.

[18] N. Bishop, J. Miller, D. Zeppettella, W. Baron, J. Tuss, and M. Ali, "A Broadband High-Gain bi-Layer LPDA for UHF Conformal Load-Bearing Antrenna

Structures (CLAS) Applications," *IEEE Transactions on Antennas and Propagation*, vol. 63, no. 5, 2015.

[19] M. Ali, N. Bishop, W. Baron, B. Smyers, J. Tuss, and D. Zeppettella, "A MEMS Reconfigurable Pixel Mictrostrip Patch Antenna for Conformal Load Bearing Antenna Structures (CLAS) Concept," in *IEEE Antennas and Propagation Society International Symposium*, Jul. 2014.

[20] N. Bishop, M. Ali, W. Baron, J. Miller, J. Tuss, and D. Zeppettella, "Aperture Coupled MEMS Reconfigurable Pixel Patch Antenna for Conformal Load Bearing Antenna Structures (CLAS)," in *IEEE Antennas and Propagation Society International Symposium*, Jul. 2014.

[21] Y. Chen and C. Wang, "Electrically Small UAV Antenna Design Using Characteristic Modes," *IEEE Transactions on Antennas and Propagation*, vol. 62, no. 2, 2014.

[22] R. Garbacz, "A Generalized Expansion for Radiated and Scattered Fields," Ph.D. Dissertation, The Ohio State University, Columbus, OH, 1968.

[23] R. Garbacz and R. Turpin, "A Generalized Expansion for Radiated and Scattered Fields," *IEEE Transactions on Antennas and Propagation*, vol. AP-19, pp. 348–358, May 1971.

[24] R. Harrington and J. Mautz, "Theory of Characteristic Modes for Conducting Bodies," *IEEE Transactions on Antennas and Propagation*, vol. AP-19, no. 5, pp. 622–628, Sep 1971.

[25] ——, "Theory of Characteristic Modes for Conducting Bodies," *IEEE Transactions on Antennas and Propagation*, vol. AP-19, no. 5, pp. 629–639, Sep 1971.

[26] E. Newman, "Small Antenna Location Synthesis Using Characteristic Modes," *IEEE Transactions on Antennas and Propagation*, vol. 27, no. 4, pp. 530–531, July 1979.

[27] P. Hazdra, P. Hamouz, M. Mazanek, and S. Zvanovec, "Theory of Characteristic Modes: Getting More Insight into Linear Antenna Behavior," in *Proceedings of the 17th International Conference Radioelectronika*, Apr. 2007.

[28] B. Austin and K. Murray, "The Application of Characteristic-ModeTechniques to Vehicle-Mounted NVIS Antennas," *IEEE Transactions on Antennas and Propagation*, vol. 40, no. 1, pp. 7–21, February 1998.

[29] Y. Chen and C. Wang, *Characteristic Modes: Theory and Applications in Antenna Engineering*. John Wiley and Sons, Inc, 2015.

[30] J.Adams and J.Bernard, "A Modal Approach to Tuning and bandwidth Enhancements of an Electrically Small Antenna," *IEEE Transactions on Antennas and Propagation*, vol. 59, no. 4, 2011.

[31] J. Chalas, K. Sertel, and J. Volakis, "Design of in-situ antennas using platform characteristic modes," in *2013 IEEE International Symposium on Antennas and Propagation and USNC/URSI National Radio Science Meeting*, 2013.

[32] M. Wright, M. Ali, W. Baron, J. Miller, J. Tuss, and D. Zeppettella, "Conformal direct written antenna on structural composites," in *Antennas and Propagation and USNC/URSI National Radio Science Meeting, 2015 IEEE International Symposium on*, Jul. 2015.

[33] K. Nicholson and P. Callus, "Antenna patterns from single slots in carbon fibre reinforced plastic waveguides," Defence Science and Technology Organisation, Australia, Technical Report, Feb. 2010.

[34] M. Cabedo-Fabres, "Systematic design of antennas using the theory of characteristic modes," PhD Dissertation, Technical University of Valencia, Valencia, Spain, 2007.

[35] K. M. Z. Shams and M. Ali, "Analysis of a Dipole Antenna Loaded by a Cylindrical Shell of Double negative (DNG) Material," *International Journal of Antennas and Propagation*, vol. 2007, article ID 97481, p. 10, 2007.

[36] R. A. Burberry, *VHF and UHF Antennas*. The Institute of Engineering and Technology, 1992.

[37] M. E. Davis, *Foilage Penetrating Radar*. SciTech Publising, 2012.

[38] D. Lopez, M. Ignatenko, and D. Fillipovic, "Low-profile tri-band inverted-f antenna for vehicular applications in hf and vhf band," *IEEE Transactions on Antennas and Propagation*, pp. 4632–4639, nov 2015.

[39] M. Hossain and Y. Ohashi, "Stub coupled monopole antenna for a broadband application," in *Microwave Conference Proceedings (APMC), 2011 Asia-Pacific*, IEEE, Ed., December 2011.

[40] Antcom Coporation. (2017) "UHF Band Antenna Catalog". Accessed 27 Oct. 2017. [Online]. Available: http://www.antcom/documents/catalogs/UHF-Band Antennas.pdf

[41] RF Micro Devices, Inc., *"RFXF9503 1:1 SMT Transformer"*, 2006, RFXF9503 Datasheet.

[42] D. Reith, C. Heller, D. Blaschke, and G. Ascheid, "Line-of-sight mimo in aircraft-to-aircraft data links," in *IEEE/AIAA 33rd Digital Avionics Systems Conference Proceedings*, IEEE/AIAA, Ed., December 2014.

[43] C. Zhang, K. Pang, and L. Ma, "Interpolated airborne mimo antenna array," *IEEE Antennas Wireless Propagat. Letters*, vol. 14, pp. 72–75, 2014.

[44] B. Holter, J. Hakegard, and T. Myrvoll, "On the use of MIMO in aeronautical communications," in *Proc. 2nd ENRI International Workshop on ATM/CNS (EIWAC2010)*, E. N. R. Institute, Ed., 2010.

[45] A. Flattie, "Performance evaluation of mimo cooperative radar by considering high altitude aeronautical platforms," in *International Conference on challenges in IT, Engineering and Technology (ICCIET2014)*, I. I. of Engineers, Ed., July 2014. [Online]. Available: http://dx.doi.org/10.15242/IIE.E0714069

[46] C. Votis, G. Tatsis, and P. Kostarakis, "Envelope correlation parameter measurements in a mimo antenna array configuration," *Int. J. Communications, Network and System Sciences*, vol. 3, 2010.

[47] K. Fujjimoto, *Mobile Antenna Systems Handbook*. Artech House Inc., 2001.

[48] C. Balanis, *Antenna Theory*, 3rd ed. Hoboken, NJ: Wiley and Sons, 2005.

[49] J. Bell and M. Iskander, "A low-profile archimedian spiral antenna using an ebg ground plane," *IEEE Antennas and Wireless Propagation Letters*, pp. 223–226, 2004.

[50] H. Nakano, K. Kikkawa, N. Kondo, Y. Itisuka, and J. Yamauchi, "Low-Profile Equiangular Spiral Antenna Backed by an EBG Reflector," *IEEE Transcations on Antennas and Propagation*, vol. 57, no. 5, pp. 1309–1318, May 2009.

[51] J. D. Krauss, *Antennas for All Applications*, 3rd ed. Boston, MA: McGraw-Hill, 2002.

[52] Federal Aviation Administration, *Aviation Maintenance Technician Handbook*. FAA, 2014, vol. 1, no. FAA-H-8083-31, accessed 5 November 2016. [Online]. Available: https://www.faa.gov /regulations_policies/handbooks_manuals/aircraft/amt_airframe_handbook/

[53] M. McFadden and W. Scott, "Analysis of the equiangular spiral antenna on a dielectric substrate," *IEEE Transactions on Antennas and Propagation*, vol. 55, no. 11, pp. 3163–3177, Nov. 2007.

[54] D. Sievenpiper, "High-impedance electromagnetic surfaces," Ph.D. Dissertation, University of California at Los Angeles, 1999.

[55] H. Nakano, K. Hitosugi, N. Tatsuzawa, D. Togashi, H. Mimaki, and J. Yamauchi, "Effects on the radiation characteristics of using a corrugated reflector with a helical antenna and an elecromagnetic bandgap reflector with a spiral antenna," *IEEE Transactions on Antennas and Propagation*, vol. 53, no. 1, pp. 191–199, January 2005.

[56] M. Coulombe, S. Koodiani, and C. Caloz, "Compact elongated mushroom (em)-ebg structure for enhancement of patch antenna performances," *IEEE Transcations on Antennas and Propagation*, vol. 58, no. 4, pp. 1070–1086, April 2010.

[57] K. Payandehjoo and R. Abhan, "Employing EBG Structures in Multiantenna Systems for Improving Isolation and Diversity Gain," *IEEE Antennas and Wireless Propagation Letters*, vol. 8, pp. 1162–1165, October 2009.

[58] Y. Lee, J. Yeo, K. Ko, R. Mittra, Y. Lee, and W. Park, "A novel design technique for control of defect frequencies of an electromagnetic band gap (ebg) cover for dual band directivity enhancement," *Microw. Opt. Technol. Lett.*, vol. 42, no. 1, pp. 25–31, July 2004.

[59] M. SalarRahimi, J. Rashed-Mohassel, and M. Edalatipour, "Radiation properties enhancement of a gsm/wlan microstrip antenna using dual band circularly symmetric ebg structure," *IEEE Transcations on Antennas and Propagation*, pp. 5491–5494, November 2012.

[60] N. Kushwaha and R. Kumar, "Study of different shape electromagnetic bandgap structures for single and dual band applications," *Journal of Microwaves, Optoelectronics and Electromagnetic Applications*, vol. 13, no. 1, pp. 16–29, June 2014.

[61] M. Azad and M. Ali, "Novel Wideband Directional Dipole Antenna on a Mushroom Like EBG Structure," *IEEE Transaction on Antennas and Propagation*, vol. 56, pp. 1242–1250, 2008.

[62] N. Chamok, T. Anthony, S. Weiss, and M. Ali, "Ultrathin UHF Broadband Antenna on a Nonuniform Aperiodic Metasurface," *IEEE Antennas and Propagation Magazine*, vol. 57, no. 2, April 2015.

[63] J. D. Dyson, "The equiangular spiral antenna," *RE Trans. Antennas Propag.*, vol. AP-7, no. 2, pp. 181–187, April 1959.

[64] F. Yang and Y. Rahmat-Sammi, *Electromagnetic Band Gap Structures in Antenna Engineering*. Cambridge University Press, 2008.

[65] S. Palreddy, "Wideband Electromagnetic Band Gap (EBG) Structures, Analysis and Applications to Antennas," Ph.D. Dissertation, Virginia Polytechnic Institute and State University, May 2015.

[66] M. Tanabe, M. Oyama, Y. Oishi, and Y. Masuda, "A spiral antenna over a high-impedance surface consisting of fan-shaped cells," in *IEEE-APS Topical Conference on Antennas and Propagation in Wireless Communications*. IEEE, Sep. 2015.

[67] M. Tanabe, M. Oyama, and Y. Masuda, "A bent-ends spiral antenna above a fan-shaped electromagnetic band-gap structure," in *9th European Conference on Antennas and Propagation*. IEEE, Apr. 2015.

[68] M. Amiri, C. Balanis, and C. Birtcher, "Analysis, Design, and Measurements, of Circularly Symmetric High-Impedance Surfaces for Loop Antenna Applications," *IEEE Transactions on Antennas and Propagation*, vol. 64, no. 2, pp. 618 – 629, Feb. 2016.

[69] J. Sarrazin, A. Lepage, and X. Begaud, "Circular high-impedance surfaces characterization," *IEEE Antennas and Wireless Propagation Letters*, vol. 11, pp. 260–263, 2012.

[70] G. Ruvio, M. Ammann, and X. Bao, "Radial ebg cell layout for gps patch antennas," *Electronics Letters*, vol. 46, no. 43, Jun. 2009.

[71] M. Tanabe, M. Matsumoto, and Y. Masuda, "A two-arm archimedean spiral antenna with bent ends," in *IEEE-APS Topical Conference on Antennas and Propagation in Wireless Communications*. IEEE, Sep. 2012.

[72] Pasternack Enterprises Inc. "Technical Data Sheet, RG223/U". Accessed 1 Dec 2017. [Online]. Available: www.pasternack.com/images/ProductPDF/RG223-U.pdf

[73] M. Tanabe, "A spiral antenna above a hybrid his-ebg reflector," in *IEEE-APS Topical Conference on Antennas and Propagation in Wireless Communications*, Sep. 2016.

[74] M. Tanabe and Y. Masuda, "Axial ratio characteristics of an archimedean spiral antenna on a thin magnetic material," in *International Conference on Electromagnetics in Advanced Applications*. IEEE, 2010.

[75] I. Tzanidis, C.-C. Chen, and J. Volakis, "Low profile spiral on a thin ferrite ground plane for 220-500 mhz operation," *IEEE Transactions on Antennas and Propagation*, vol. 58, no. 11, pp. 3715–3720, Nov. 2010.

[76] C. Liu, Y. Lu, C. Du, J. Cui, and X. Shen, "The Broadband Spiral Antenna Design Based on Hybrid Backed-Cavity," *IEEE Transactions on Antennas and Propagation*, vol. 58, no. 6, pp. 1876–1882, June 2010.

[77] M. Amiri, C. Balanis, and C. Birtcher, "Applications of circularly sysmmetric high impedance surfaces for spiral antennas," in *International Symposium on Antennas and Propagation*, 2016.

[78] ——, "Gain and Bandwidth Enhancement of a Spiral Antenna Using a Circularly Symmetric HIS," *IEEE Antennas and Wireless Propagation Letters*, vol. 16, pp. 1080–1083, Oct 2016.

[79] ——, "Reflection Phase Characterization of Wideband Semi-Periodic Circular High Impedance Surface," in *International Conference on Advanced Technologies for Communications*, Oct 2015.

[80] G. Saleh, K. Solbach, and A. Rennings, "Ebg structure for low frequency applications," in *Proceedings of the 7th German Microwave Conference*. IEEE, March 2012.